

AEROSPACE RESEARCH IN BULGARIA

Founded in 1978

Volume 28, Sofia, 2016
Space Research and Technology Institute
Bulgarian Academy of Sciences

Editorial Board

Prof. Garo Mardirossian (*Editor-in-Chief*)
Assoc. Prof. Lachezar Filchev (*English Language Editor*)
Tsveta Srebrova, MS (*Technical Editor*)

Acad. Valeri Bondour – Russia
Prof. Gerassimos Papadopoulos – Greece
Prof. Stefano Tinti – Italy
Assoc. Prof. Premysl Štych – Czech Republic
Corr. Member Petar Getsov
Corr. Member Filip Filipov
Corr. Member Petar Velinov
Prof. Petko Nenovski
Prof. Eugenia Roumenina
Prof. Dimitar Teodossiev
Assoc. Prof. Tania Ivanova
Assoc. Prof. Lachezar Filipov
Assoc. Prof. Bozhidar Srebrov

Address

AEROSPACE RESEARCH IN BULGARIA
Space Research and Technology Institute
Acad. Georgi Bonchev St., block 1, 1113 Sofia, Bulgaria

web-site: <http://journal.space.bas.bg>
e-mail: journal@space.bas.bg

Pre-Publication Processing
Tsveta Srebrova

© Space Research and Technology Institute – Bulgarian Academy of Sciences

p-ISSN 1313–0927

e-ISSN 2367–9522

This issue of *Aerospace Research in Bulgaria* is published with financial support from the Bulgarian National Science Fund – Contract No ДНП 05/45 – 22.12.2016

Aerospace Research in Bulgaria

28

Sofia, 2016

C o n t e n t s

1. *Peter Velinov*
EXTENDED CATEGORISATION OF GROUND LEVEL ENHANCEMENTS
(GLEs) OF COSMIC RAYS DUE TO RELATIVISTIC SOLAR ENERGETIC
PARTICLES. 5
2. *Alexander Yosifov, Lachezar Filipov*
BLACK HOLE THERMODYNAMICS FOR PRODUCING HORIZON
OSCILLATIONS. 21
3. *Alexander Yosifov, Lachezar Filipov*
HORIZON OSCILLATIONS FOR PRESERVING THE EQUIVALENCE
PRINCIPLE. 32
4. *Tsvetan Dachev, Borislav Tomov, Yuri Matviichuk, Plamen Dimitrov,
Vyacheslav Shurshakov, Victor Benghin, Elena Yarmanova,
Olga Ivanova, Igor Nikolaev*
“LIUILIN-ISS-2” SYSTEM FOR COSMONAULTS’ DOSIMETRIC CONTROL
IN THE ISS RADIATION ENVIRONMENT. 38
5. *Yuriy Kuksa, Igor Shibaev, Dimitar Teodosiev, Jaroslav Vojta*
DYNAMICS OF REGULAR AND INCIDENTAL EVENTS ACCORDING
TO THE MAGNETOMETRIC COMPLEX: MATERIALS
OF THE “SCHUMAN” PROJECT. 59
6. *Dimitar Dimitrov*
APPLICATION OF SPACE TECHNOLOGIES FOR STUDIES
AND MONITORING OF SEISMOGENIC ZONES. 67

7. <i>Ivan Yanev, Lachezar Filchev</i>	
A COMPARATIVE ANALYSIS BETWEEN MODIS LST LEVEL-3 PRODUCT AND IN-SITU TEMPERATURE DATA FOR ESTIMATION OF URBAN HEAT ISLAND OF SOFIA.	77
8. <i>Svetoslav Zabunov</i>	
QUATERNION-BASED AUTOPILOT FOR DODECACOPTERS - PART I.	93
9. <i>Peter Petkov, Elissaveta Alexandrova, Maxim Zayakov</i>	
KU-BAND SMALL ANTENNA FOR SATELLITE EARTH STATIONS WITH IMPROVED RADIATION DIAGRAM.	113
10. <i>Konstantin Metodiev</i>	
A RECTANGULAR UNIPOLAR PULSE WIDTH MEASUREMENT BY MEANS OF PIC18F2550 MCU.	122

New Projects

DOSIMETRY SCIENCE PAYLOADS FOR EXOMARS TGO & SURFACE PLATFORM. UNIFIED WEB-BASED DATABASE WITH LIULIN TYPE INSTRUMENTS' COSMIC RADIATION DATA (“DOSIMETRY”).	129
---	-----

TESTING SENTINEL-2 VEGETATION INDICES FOR THE ASSESSMENT OF THE STATE OF WINTER CROPS IN BULGARIA (TS2AGROBG).	131
---	-----

COORDINATING AND INTEGRATING STATE-OF-THE-ART EARTH OBSERVATION ACTIVITIES IN THE REGIONS OF NORTH AFRICA, MIDDLE EAST, AND BALKANS AND DEVELOPING LINKS WITH GEO RELATED INITIATIVES TOWARDS GEOSS - GEO-CRADLE.	133
--	-----

EEOBSS: EDUCATION IN EARTH OBSERVATION FOR BULGARIAN SECONDARY SCHOOLS.	135
--	-----

Jubilee

<i>Tanya Ivanova</i>	
VALENTINA TERESHKOVA CELEBRATES 80 th ANNIVERSARY.	137

СЪДЪРЖАНИЕ

- 1. Петър Велинов**
РАЗШИРЕНА КАТЕГОРИЗАЦИЯ НА ПОВИШЕНИЯТА
НА КОСМИЧЕСКИТЕ ЛЪЧИ НА ЗЕМНАТА ПОВЪРХНОСТ
(GLEs) ПОРОДЕНИ ОТ ВИСОКОЕНЕРГИЙНИ СЛЪНЧЕВИ ЧАСТИЦИ. 5
- 2. Александър Йосифов, Лъчезар Филипов**
ТЕРМОДИНАМИКА НА ЧЕРНИ ДУПКИ КАТО ПРИЧИНА
ЗА ТРЕПТЕНИЯ НА ХОРИЗОНТА. 21
- 3. Александър Йосифов, Лъчезар Филипов**
ТРЕПТЕНИЯ НА ХОРИЗОНТА ЗА ЗАПАЗВАНЕ НА ПРИНЦИПА
НА ЕКВИВАЛЕНТНОСТТА. 32
- 4. Цветан Дачев, Борислав Томов, Юри Матвийчук,
Пламен Димитров, Вячеслав Шуршаков, Виктор Бенгин,
Елена Ярманова, Олга Иванова, Игор Николаев**
ОПИСАНИЕ НА СИСТЕМАТА "ЛЮЛИН-МКС-2" ЗА ДОЗИМЕТРИЧЕН
КОНТРОЛ НА КОСМОНАВТИТЕ В РАДИАЦИОННАТА СРЕДА НА МКС. . . 38
- 5. Юрий Кукса, Игор Шибаетов, Димитър Теодосиев, Ярослав Войта**
ДИНАМИКА НА РЕГУЛЯРНИ И СЛУЧАЙНИ СЪБИТИЯ ПО ДАННИ
ОТ МАГНИТОМЕТРИЧЕСКИЯ КОМПЛЕКС: МАТЕРИАЛИ ОТ ПРОЕКТ
"ШУМАН". 59
- 6. Димитър Димитров**
ПРИЛОЖЕНИЕ НА КОСМИЧЕСКИ ТЕХНОЛОГИИ ЗА ИЗСЛЕДВАНЕ
И МОНИТОРИНГ НА СЕИЗМОГЕННИ ЗОНИ. 67
- 7. Иван Янев, Лъчезар Филчев**
СРАВНИТЕЛЕН АНАЛИЗ МЕЖДУ MODIS LST НИВО-3 СПЪТНИКОВИ
ПРОДУКТИ И НАЗЕМНИ ТЕМПЕРАТУРНИ ИЗМЕРВАНИЯ ЗА ОЦЕНКА
НА ГРАДСКИЯ ТОПЛИНЕН ОСТРОВ НА ГР. СОФИЯ. 77
- 8. Светослав Забунов**
АВТОПИЛОТ ЗА ДВАНАДЕСЕТОКОПТЕРИ, БАЗИРАН
ВЪРХУ КВАТЕРНИОНИ – ЧАСТ I. 93
- 9. Петър Петков, Елисавета Александрова, Максим Заяков**
МАЛКА АНТЕНА ЗА ЗЕМНИ СТАНЦИИ ЗА ВРЪЗКА СЪС СПЪТНИЦИ
В КУ-ОБХВАТА С ПОДОБРЕНА ДИАГРАМА НА ИЗЛЪЧВАНЕ. 113

10. Константин Методиев

ИЗМЕРВАНЕ НА ШИРОЧИНАТА НА ПРАВОЪГЪЛЕН ЕДНОПОЛЯРЕН
ИМПУЛС С ПОМОЩТА НА МИКРОКОНТРОЛЕР PIC18F2550.122

Нови проекти

ДОЗИМЕТРИЯ: НАУЧНА АПАРАТУРА ЗА ДОЗИМЕТРИЧНИ
ИЗСЛЕДВАНИЯ ЗА СПЪТНИКА TGO И ПЛАТФОРМАТА
НА ПОВЪРХНОСТТА НА МАРС ПО ПРОЕКТ ЕКЗОМАРС.
ИНТЕРНЕТ БАЗИРАНА БАЗА ДАННИ ЗА КОСМИЧЕСКАТА
РАДИАЦИЯ, ПОЛУЧЕНА ОТ УРЕДИТЕ ОТ СЕРИЯТА “ЛЮЛИН”.129

ТЕСТВАНЕ НА ВЕГЕТАЦИОННИ ИНДЕКСИ ОТ SENTINEL-2
ЗА ОЦЕНКА НА СЪСТОЯНИЕТО НА ЗИМНИ КУЛТУРИ В БЪЛГАРИЯ. . . .131

КООРДИРАНЕ И ИНТЕГРИРАНЕ НА СЪВРЕМЕННИ МЕТОДИ
ЗА НАБЛЮДЕНИЕ НА ЗЕМЯТА В РАЙОНА НА СЕВЕРНА АФРИКА,
БЛИЗКИЯ ИЗТОК И БАЛКАНИТЕ И СЪЗДАВАНЕ НА ВРЪЗКИ КЪМ
ИНИЦИАТИВИ ПО ПРОГРАМА GEO, НАСОЧЕНИ КЪМ GEOSS.133

ОБРАЗОВАНИЕ ПО НАБЛЮДЕНИЕ НА ЗЕМЯТА ЗА БЪЛГАРСКИТЕ
СРЕДНИ УЧИЛИЩА (ЕЕОВSS).135

Юбилей

Таня Иванова

ВАЛЕНТИНА ТЕРЕШКОВА НА 80 ГОДИНИ.137

EXTENDED CATEGORISATION OF GROUND LEVEL ENHANCEMENTS (GLEs) OF COSMIC RAYS DUE TO RELATIVISTIC SOLAR ENERGETIC PARTICLES

Peter Velinov

*Space Research and Technology Institute – Bulgarian Academy of Sciences
e-mail: pvelinov@bas.bg*

Abstract

The ground level enhancements (GLEs) due to solar cosmic rays (SCRs) are significant for a number of planetary processes on the Earth. The solar particles are the key for understanding of solar-terrestrial relations and space weather. On the basis of ground based observations of SCRs from 28 February 1942 (when they were discovered) to the end of 2015, have been determined some characteristic periods of GLEs and observed during the solar cycles 17–24. It is made quantifying of GLEs and the frequency of occurrence of GLEs in the different solar cycles is determined.

This article presents also a categorization of the ground level enhancements (from the first GLE 01 on February 28, 1942 to the last GLE 72 on January 06, 2014) due to solar energetic particles reaching the Earth's surface. We have detected new groups of collective GLEs, recurrent GLEs, recurrent-collective GLEs, collective-recurrent GLEs, etc. Physical, methodical, and applied aspects, related to the SCR and GLE events have been discussed as well, because they have an extreme impact on Earth. The obtained results have prognostic value and significance for the ionization and radiation conditions in the Earth environment and for the mechanisms of solar-terrestrial influences.

Introduction

The solar energetic particles (SEPs) and solar cosmic rays (SCRs) are of outstanding cosmophysical and astrophysical interest [1–5]. The solar proton events (SPEs) occur as a result of massive acceleration of charged particles in the solar corona and/or interplanetary space. Usually such events provide quite a soft spectrum of energetic particles, but sometimes the spectrum is sufficiently hard, so that the initial solar protons can generate secondary nucleons that can be detected as an increase in the cosmic ray flux at the ground level [6–12]. Such exceptional events are called with the international name GLE (Ground Level Enhancement or Ground Level Event) of cosmic rays (CRs) and are numbered consecutively from the first event that was detected in 1942 [13]. On February 28, 1942, ground detectors for the first time registered that accelerated solar protons arrived to the Earth. A new similar event was registered on March 7, 1942 [14]. This was one of

the greatest astrophysical discoveries of the 20th century: it turned out that charged particles can be accelerated to high energies in the interplanetary space [15].

However, researchers realized this fundamental fact and its close relation to solar flares with some delay. Only after the registration of the third similar event on July 25, 1946, the author of this discovery S. Forbush (1946) [13] wrote with caution that these observations "... make it possible to draw a rather unexpected conclusion that all three unusual CR intensifications can be explained by fluxes of charged particles emitted by the Sun." After the fourth ground level increase in SCRs on November 19, 1949 [16], the relationship between the observed relativistic particles and solar flares became an unquestionable fact, which motivated the appearance of a new concept for the nature of the intense flux of energetic particles, measures at the ground.

The SCRs can include other nuclei such as helium ions and HZE (high – H, atomic number – Z, and energy – E) ions [17]. These particles cause multiple effects. They can penetrate the Earth's magnetic field and cause ionization in the ionosphere [18–21]. The effect is similar to auroral events, however, instead of electrons, the protons are involved in the processes of ionization, dissociation, excitation etc. Energetic protons are also a significant radiation hazard to spacecrafts and spaceflights.

In the present paper we shall discuss and analyze some physical aspects of GLEs, namely, the distribution of GLEs during solar cycles 17÷24 (1942–2015), as well as the frequency of GLE event appearance. We will perform a new categorisation of different types of GLE events and we shall consider the cases of collective and recurrent GLEs. We will also illustrate some GLE effects on the Earth's atmosphere, i.e. the SCR geophysical effects. The prospects of studying SCRs/GLEs will be considered also in the end of this work.

Worldwide network of stations and data for GLEs

Ground-based observations of the secondary components (mainly muons and neutrons) are still the most reliable sources of data for primary SCRs, which are relativistic particles. Ionization chambers (ICs), muon telescopes (MTs), and neutron monitors (NMs, from the mid 1950s) were the first detectors that were used to register GLEs. The effective energies of particles, detected by these instruments at sea level, are ~25÷35, 15÷20, and 4÷6 GeV, respectively [15]. Neutron detector has been used for the first time to register GLE event of November 19, 1949 [16]. Geomagnetic cutoff rigidity (R_c) of particles during their motion in the Earth's magnetosphere is one of the main CR station characteristics.

The worldwide network of NMs was created more than 50 years ago based on IGY-type NMs. Data acquisition and analysis systems were constantly modernized, and a new modification of such a system, a SNM-64 neutron supermonitor [15], was designed in the early 1960s. Here we use the international

GLE database organized by the University of Oulu [6]. A new generation of the International GLE database is accessible at the web-site URL: <https://gle.oulu.fi> collecting and archiving data from the worldwide neutron monitor network concerning GLE events. The GLE database covers events starting from № 5 (GLE05 on February 23, 1956) and provides a useful tool for an analysis of the most energetic solar particle events.

Distribution of all GLEs during solar cycles 17-24 (1942-2015)

Seventy two GLEs were registered from February 1942 to the end of 2015. From February 28, 1942 (GLE 01), all events were numbered for the convenience of researchers. The last event in cycle 23 of solar activity (SA) was observed on December 13, 2006 (GLE 70). In cycle 24 (started in January 2009), SCR activity was registered with a delay: the first GLE in the new cycle occurred only on May 17, 2012 (GLE 71). To all appearance, this pause not only reflects the specific properties of cycle 23 (in particular, a very long period of SA minimum) but also characterizes the unusual character of cycle 24, which is most probably a critical cycle in the SA behavior for the last 150÷200 years [15, 22].

Analyzing a list of all GLEs, we can determine several characteristic periods, which are important parameters for manifestations of SA in a concrete solar cycle. The quantifying of GLEs in solar cycles 17÷24 is presented in Table 1. Here are given the introduced periods A, II, and Δ .

Table 1. Quantifying the GLEs in solar cycles 17÷24 and the corresponding characteristic periods

Solar cycle №	Started (YYYY.MM)	Finished (YYYY.MM)	Duration (years)	№ of GLE	A	II	Δ
17	1933.09	1944.01	10.4	2	– –	1W	4Y 5M
18	1944.01	1954.02	10.1	2	2Y 6M	3Y 4M	6Y 3M
19	1954.02	1964.10	10.7	10	2Y	5Y 5M	5Y
20	1964.10	1976.05	11.7	12	1Y 9M	6Y 9M	3Y
21	1976.05	1986.08	10.3	13	1Y	7Y 10M	5Y 5M
22	1986.08	1996.08	10.0	15	2Y 11M	3Y 3M	5Y
23	1996.09	2008.12	12.2	16	1Y 2M	9Y 1M	5Y 5M
24	2009.01	2018	Still ongoing	(2)	3Y 5M		

In Table 1, A is the period from the beginning of the considered solar cycle to the appearance of the first GLE. This is a passive period of accumulation of energy, after that begins the next active period II;

Π is an active period from the first GLE to the last GLE in the considered solar cycle;

Δ is a passive period from the last GLE in the current solar cycle to the appearance of the first GLE of the next solar cycle.

All periods in the Table 1 are expressed in years (Y), months (M) and weeks (W).

From Table 1 we can determine the ratio

$$\text{(Number of GLE)} / \Pi \text{ or } N(\text{GLE}) / \Pi$$

These results are shown in Table 2. From here it is seen that the highest occurrence rate of the GLEs is in the solar cycles 19, 20, and 22.

Table 2. Determination of GLE frequency of occurrence in solar cycles 18÷23

Solar cycle №	17	18	19	20	21	22	23	24
$N(\text{GLE}) / \Pi$	–	0.6	1.85	1.78	1.66	4.62	1.76	–

Based on Tables 1 and 2, we can assume that some weak GLEs were not registered in the early years of observations due to technical and methodological difficulties. If the average occurrence rate of the GLEs is $\eta \sim 1.0 \text{ yr}^{-1}$, the number of omitted events in 1942–1956 could be considerable [15]. A prolonged minimum of cycle 23 ended in December 2008; however, cycle 24 (started in January 2009) is proceeding very slowly [23] and sunspot formation as well solar flare and proton activities are generally at a rather low level. Thus, the first GLE 71 on 17 May 2012 was registered during more than three years off the cycle and more than five years after the last event in cycle 23 (GLE 70 on December 13, 2006). More precisely from Table 1 follows: $A = 3Y \ 5M$ and $\Delta = 5Y \ 5M$.

GLEs in the current solar cycle 24

In cycle 24 (started in January 2009) the first GLEs was registered at the beginning of 2012 (Table 3). This time delay reflects the specific properties of cycle 23 (in particular, the long lasting solar minimum) and correspondingly the unusual character of cycle 24 [15]. Solar Cycle 24 has been the weakest in the space era according to the measured sunspot number (SSN). The average SSN over the first 73 months of cycle 24 was ~ 46 , compared to 76 over the same epoch in cycle 23. This corresponds to a decrease of $\sim 40\%$ [23]. The solar activity has already entered into the declining phase, but the number of high-energy solar energetic particle (SEP) events has remained very low. During the first 73 months of cycle 24, there were only two ground level enhancement (GLE) events: 2012 May 17 and 2014 January 6 (Table 3). Over the same epoch, there were 9 GLE events in cycle 23. Thus the reduction in the number of GLE events is by 78 %, much higher than that in SSN. The number of SEP events, emitting particles with energies $>500 \text{ MeV}$, was also higher in cycle 23 (18 vs. 6 in cycle 24) [24, 25].

Besides GLEs, four more solar energetic proton events are included in Table 3. Three of them occurred in January and March 2012 and have a significant increase of the integral proton fluxes with energies > 500 MeV, registered by the data from subpolar neutron monitors. As it was found these events were followed by a cosmic ray enhancement of about 2 % at several subpolar and high latitude neutron monitors. Nevertheless, these events may contain some contribution of solar cosmic rays in the ground level observations [26].

Table 3. List of GLEs and contenders for GLEs during solar cycle 24

Event No	Event Date	Baseline Date (YYMMDD)	Recommended Baseline Time Start - End (UT)
(*)	27 January 2012	120127	160000 - 170000
(*)	07 March 2012	120306	230000 - 240000
(*)	13/14 March 2012	120313	160000 - 170000
071	17 May 2012	120517	000000 - 010000
072	06 January 2014	140106	070000 - 080000
(*)	29 October 2015	151029	000000 - 010000

(*) Events 27 January 2012, 7 March 2012, 13 March 2012, and 29 October 2015 are GLE contenders

All four events marked with (*), the three events at the beginning of 2012, as well as the SEP event from 29 October 2015, may be considered as candidate GLEs of SCRs. We will name them quasi-GLEs or abbreviated as qGLEs.

Collective GLEs in solar cycle 24 and before that

Analysis of Table 3 reveals an existence of a collective GLE. Thus the second and the third qGLEs (on 07 March 2012 and on 13/14 March 2012, respectively) represent one common collective event. The flare positions of the corresponding collective GLEs (cGLEs) on the Sun are [26]:

17N 27E for 07 March 2012 and

19N 59W for 13/14 March 2012,

i.e. both qGLEs are generated by one and the same active area AR11429 on the Sun, which has 27-day solar rotation period.

Here we show a number of other cases of cGLEs before solar cycle 24. We demonstrate the new evidence about these phenomena. In Table 4 is presented information about the flare position of every concrete GLE, the universal time (UT) of the onset of event, the H α /X flare importance, the active area (AR) [15] and the sequence number of the corresponding collective GLE.

List of all collective GLEs during cycles 17÷24

From the above mentioned list of all GLEs (1942-2015), we can show 14 cases of collective GLEs (cGLEs). Yet the first two cases of GLEs (GLE01 on February 28, 1942 and GLE02 on March 7, 1942) represent one collective event. The flare positions of the corresponding GLEs on the Sun were [15]:

07N 04E for GLE01 and
07N 90W for GLE02,

i.e. both cGLEs are generated by one and the same active center on the Sun, which has 27-day solar rotation period. In Table 4 is presented the list of the cGLEs during solar cycles 17÷24.

Table 4. List of collective GLEs (cGLEs) and corresponding flares and active areas (AR) during solar cycles 17÷24

Event №	Event Date	Flare Position	Onset UT	Importance H α /X	cGLE №	
01	28 February	1942 (1)	07N 04E	1228	3+	1
02	07 March	1942 (2)	07N 90W	N.O.	-/-	Double 1
01	28 February	1942 (1)	07N 04E	1228	3+	1
02	07 March	1942 (2)	07N 90W	N.O.	-/-	Double 1
10	12 November	1960 (1)	27N 04W	1315	3+	2
11	15 November	1960 (2)	25N 35W	0207	3+	
12	20 November	1960 (3)	28N 112W	2017	2	Triple 1
13	18 July	1961 (1)	07S 59W	0920	3+	3
14	20 July	1961 (2)	6S 90W	1553	3	Double 2
16	28 January	1967 (1)	22N 150W	<0200	-/-	4
17	28 January	1967 (2)	22N 150W	<0800	-/-	Double 3
24	04 August	1972 (1)	14N 08E	0617	3B/X4	5
25	07 August	1972 (2)	14N 37W	1449	3B/X43D	Double 4
28	19 September	1977 (1)	08N 57W	<0955	3B/X2	6
29	24 September	1977 (2)	10N 120W	<0552	-/-	Double 5
43	19 October	1989 (1)	25S 09E	1229	3B/X13	7
44	22 October	1989 (2)	27S 32W	1708	1N/X2.9	
45	24 October	1989 (3)	29S 57W	1738	2N/X5.7	Triple 2
47	21 May	1990 (1)	34N 37W	2212	2B/X5.5	8

Table 4. List of collective GLEs (cGLEs) and corresponding flares and active areas (AR) during solar cycles 17÷24 (cont.).

Event №	Event Date	Flare Position	Onset UT	Importance H α /X	cGLE №	
48	24 May	1990 (2)	36N 76W	2046	1B/X9.3	
49	26 May	1990 (3)	35N 103W	2045	–/–	
50	28 May	1990 (4)	35N 120W	<0516	–/–	Quadruple 1
51	11 June	1991 (1)	32N 15W	0105	2B/X12	9
52	15 June	1991 (2)	36N 70W	0633	3B/X12	Double 6
56	02 May	1998 (1)	15S 15W	1334	3B/X1.1	10
57	06 May	1998 (2)	11S 65W	0758	1N/X2.7	Double 7
60	15 April	2001 (1)	20S 85W	1319	2B/X14.4	11
61	18 April	2001 (2)	23S 117W	0211	–/–	Double 8
65	28 October	2003 (1)	16S 08E	1100	4B/X17.2	12
66	29 October	2003 (2)	19S 09W	2037	–/X10	
67	02 November	2003 (3)	18S 59W	1718	2B/X8.3	Triple 3
68	17 January	2005 (1)	15N 25W	0659	3B/X3.8	13
69	20 January	2005 (2)	14N 61W	0639	2B/X7.1	Double 9
(*)	07 March	2012 (1)	17N 27E	1100	AR11429/X5.4	14
(*)	13/14 March	2012 (2)	19N 59W	0700	AR11429/M7.9	Double 10

(*) Events 7 March 2012, 13/14 March 2012 are now only contenders for GLEs

List of the recurrent GLE

Some of the investigated events are complex and require more special examinations and analyses. A careful study of the complete list of GLEs available at URL: ftp://ftp.ngdc.noaa.gov/STP/SOLAR_DATA/COSMIC_RAYS/ground-level-enhancements/ground-level-enhancements.txt, determinate the existence of different types recurrent ground level enhancements (rGLEs). Some of them are shown in Table 5. A number of these groups are subject to a detailed study with subsequent comprehensive analysis and modeling.

Table 5. List of the recurrent GLEs (rGLEs) and the corresponding flares and active areas (AR) during solar cycles 17÷24

Event №	Event Date	Flare Position	Onset UT	Importance H α /X	rGLE №	
18	29 September	1968 (1)	17N 51W	1617	2B	
19	18 November	1968 (2)	21N 87W	1026	1B	1
20	25 February	1969 (1)	13N 37W	0900	2B/X2	
21	30 March	1969 (2)	19N 103W	0332	1N	2
28	19 September	1977 (1)	08N 57W	0955	3B/X2	
30	22 November	1977 (3)	24N 40W	0945	2B/X1	3
29	24 September	1977 (2)	10N 120W	0552	–/–	
30	22 November	1977 (3)	24N 40W	0945	2B/X1	4
34	10 April	1981 (1)	07N 36W	1632	2B/X2.3	
35	10 May	1981 (2)	03N 75W	0715	1N/M1	5
42	29 September	1989 (1)	24S 105W	1141	1B/X9	
43	19 October	1989 (2)	25S 09E	1229	3B/X13	6
42	29 September	1989 (1)	24S 105W	1141	1B/X9	
44	22 October	1989 (3)	27S 32W	1708	1N/X2.9	7
42	29 September	1989 (1)	24S 105W	1141	1B/X9	
45	24 October	1989 (4)	29S 57W	1738	2N/X5.7	8
42	29 September	1989 (1)	24S 105W	1141	1B/X9	
46	15 November	1989 (5)	11N 28W	0638	2B/X3.2	9
43	19 October	1989 (2)	25S 09E	1229	3B/X13	
46	15 November	1989 (5)	11N 28W	0638	2B/X3.2	
44	22 October	1989 (3)	27S 32W	1708	1N/X2.9	
46	15 November	1989 (5)	11N 28W	0638	2B/X3.2	
45	24 October	1989 (4)	29S 57W	1738	2N/X5.7	
46	15 November	1989 (5)	11N 28W	0638	2B/X3.2	
(*)	07 March	2012 (1-2)	17N 27E	1100	AR11429/X5.4	
(*)	13/14 March	2012 (1-2)	19N 59W	0700	AR11429/M7.9	
71	17 May	2012 (3)	11N 76W	0151	AR11476/M5/1	10

(*) Events 7 March 2012, 13/14 March 2012 are now only contenders for GLEs

Recurrent-collective and collective-recurrent GLEs

The consideration of previous Tables shows the presence of some combined cases of recurrent-collective GLEs (rcGLEs) and collective-recurrent GLEs (crGLEs), which are represented in Table 6. Some of these groups are subject to a detailed study with subsequent detailed analysis and the further numerical or theoretical modeling. These are the most complicated cases, because there is a superposition of different GLE groups. They are presented in Table 6.

Table 6. List of recurrent-collective GLEs (rcGLEs), collective-recurrent GLEs (crGLEs) and corresponding flares, and active areas (AR)

Event №	Event Date	Flare Position	Onset UT	Importance H α /X	rcGLEs & crGLEs №
42	29 September 1989 (1)	24S 105W	1141	1B/X9	1
43	19 October 1989 (2)	25S 09E	1229	3B/X13	
44	22 October 1989 (2)	27S 32W	1708	1N/X2.9	
45	24 October 1989 (2)	29S 57W	1738	2N/X5.7	
46	15 November 1989 (3)	11N 28W	0638	2B/X3.2	
28	19 September 1977 (1)	08N 57W	< 0955	3B/X2	2
29	24 September 1977 (2)	10N 120W	< 0552	–/–	
30	22 November 1977 (3)	24N 40W	0945	2B/X1	
(*)	07 March 2012 (1)	17N 27E	1100	AR11429/X5.4	3
(*)	13/14 March 2012 (2)	19N 59W	0700	AR11429/M7.9	
71	17 May 2012 (3)	11N 76W	0151	AR11476/M5/1	

(*) Events 7 March 2012, 13/14 March 2012 are now only contenders for GLEs

Presentation of all ground level enhancements GLE 01 – GLE 72 during the period 1942-2015

In Table 7 are presented all ground level enhancements (from GLE 01 to GLE 72) during the whole period of investigation of these events (1942-2015). There in detail are identified the single GLEs, collective GLEs (cGLEs), recurrent GLEs (rGLEs), recurrent-collective GLEs (rcGLEs) and collective-recurrent GLEs (crGLEs). Also are included four contenders for GLEs in the current solar cycle 24. Really these nominees are quasi GLEs (qGLEs) and they are marked by the indication (*). The marked (*) events from 27 January 2012, 7 March 2012, 13 March 2012, and 29 October 2015 are GLE contenders.

Table 7. List of all 72 Ground Level Enhancements (GLEs) during 1942-2015 in the solar cycles 17÷24. Included are: single – sGLEs, collective – cGLEs, recurrent – rGLEs, recurrent-collective – rcGLEs, collective-recurrent – crGLEs, quasi – qGLEs contenders

Event №	Event Date	Baseline Date	Class GLE	Type GLE
<u>Solar cycle № 17</u>				
<u>01</u>	28 February	1942	420228 cGLE 1	Double (1)
<u>02</u>	07 March	1942	420307 cGLE 1	Double (2)
<u>Solar cycle № 18</u>				
03	25 July	1946	460725 sGLE 1	Single
04	19 November	1949	491119 sGLE 2	Single
<u>Solar cycle № 19</u>				
05	23 February	1956	560223 sGLE 3	Single
06	31 August	1956	560831 sGLE 4	Single
07	17 July	1959	590716 sGLE 5	Single
08	04 May	1960	600504 sGLE 6	Single
09	03 September	1960	600902 sGLE 7	Single
<u>10</u>	12 November	1960	601112 cGLE 1	Triple (1)
<u>11</u>	15 November	1960	601115 cGLE 1	Triple (2)
<u>12</u>	20 November	1960	601120 cGLE 1	Triple (3)
<u>13</u>	18 July	1961	610718 cGLE 2	Double (1)
<u>14</u>	20 July	1961	610720 cGLE 2	Double (2)
<u>Solar cycle № 20</u>				
15	07 July	1966	660706 sGLE 8	Single
<u>16</u>	28 January	1967	670128 cGLE 3	Double (1)
<u>17</u>	28 January	1967	670128 cGLE 3	Double (2)
<u>18</u>	29 September	1968	680929 rGLE 1	Recurrent (1)
<u>19</u>	18 November	1968	681118 rGLE 1	Recurrent (2)
<u>20</u>	25 February	1969	690225 rGLE 2	Recurrent (1)
<u>21</u>	30 March	1969	690330 rGLE 2	Recurrent (2)
22	24 January	1971	710124 sGLE 9	Single
23	01 September	1971	710901 sGLE 10	Single
<u>24</u>	04 August	1972	720804 cGLE 4	Double (1)
<u>25</u>	07 August	1972	720807 cGLE 4	Double (2)
26	29 April	1973	730429 sGLE 11	Single
<u>Solar cycle № 21</u>				
27	30 April	1976	760430 sGLE 12	Single
<u>28</u>	19 September	1977	770919 cGLE 5	Double (1)
<u>29</u>	24 September	1977	770924 cGLE 5	Double (2)
<u>30</u>	22 November	1977	771122 rGLE 3-4	Recurrent (1-2)
31	07 May	1978	780507 sGLE 13	(Single) Rec. (?)
32	23 September	1978	780923 sGLE 14	(Single) Rec. (?)
33	21 August	1979	790821 sGLE 15	Single
<u>34</u>	10 April	1981	810410 rGLE 5	Recurrent (1)
<u>35</u>	10 May	1981	810510 rGLE 5	Recurrent (2)

Event №	Event Date	Baseline Date	Class GLE	Type GLE
36	12 October 1981	811012	sGLE 16	Single
37	26 November 1982	821126	sGLE 17	Single
38	07 December 1982	821207	sGLE 18	Single
39	16 February 1984	840216	sGLE 19	Single
<u>Solar cycle № 22</u>				
40	25 July 1989	890725	sGLE 20	Single
41	16 August 1989	890815	sGLE 21	Single
42	29 September 1989	890929	rGLE 6-9	Recurrent (1-4)
43	19 October 1989	891019	cGLE 2	Triple (1)
44	22 October 1989	891022	cGLE 2	Triple (2)
45	24 October 1989	891024	cGLE 2	Triple (3)
46	15 November 1989	891115	rGLE 6-9	Recurrent (1-4)
47	21 May 1990	900521	cGLE 1	Quadruple (1)
48	24 May 1990	900524	cGLE 1	Quadruple (2)
49	26 May 1990	900526	cGLE 1	Quadruple (3)
50	28 May 1990	900528	cGLE 1	Quadruple (4)
51	11 June 1991	910611	cGLE 6	Double (1)
52	15 June 1991	910615	cGLE 6	Double (2)
53	25 June 1992	920625	sGLE 22	Single
54	02 November 1992	921102	sGLE 23	Single
<u>Solar cycle № 23</u>				
55	06 November 1997	971106	sGLE 24	Single
56	02 May 1998	980502	cGLE 7	Double (1)
57	06 May 1998	980506	cGLE 7	Double (2)
58	24 August 1998	980824	sGLE 25	Single
59	14 July 2000	000714	sGLE 26	Single
60	15 April 2001	010415	cGLE 8	Double (1)
61	18 April 2001	010418	cGLE 8	Double (2)
62	04 November 2001	011104	sGLE 27	Single
63	26 December 2001	011226	sGLE 28	Single
64	24 August 2002	020824	sGLE 29	Single
65	28 October 2003	031028	cGLE 3	Triple (1)
66	29 October 2003	031029	cGLE 3	Triple (2)
67	02 November 2003	031102	cGLE 3	Triple (3)
68	17 January 2005	050117	cGLE 9	Double (1)
69	20 January 2005	050120	cGLE 9	Double (2)
70	13 December 2006	061213	sGLE 30	Single
<u>Solar cycle № 24</u>				
(*)	27 January 2012	120127	qGLE 1	
(*)	07 March 2012	120307	c(qGLE 2) 10	Double (1)
(*)	13 March 2012	120313	c(qGLE 3) 10	Double (2)
71	17 May 2012	120517	rGLE 10	Recurrent(1-2)
72	06 January 2014	140106	sGLE 31	Single
(*)	29 October 2015	151029	qGLE 4	

The bold and underlined numbers EVENT # indicate the collective GLEs, which are sorted in ascending order. The collective GLEs are also classified in Double, Triple and Quadruple;

The bold and italic numbers EVENT # indicate the recurrent GLEs, which are classified and sorted also in ascending order;

The remaining GLEs are simple, i.e. they are individual increases in CR intensity. Some of them may be substantially strong, as was the case of 23 February 1956 (GLE 05). This is the maximum proton flare in GLE history.

Single GLEs

There are a total of 31 single GLEs, which are designated as sGLE. These are the following events: 03, 04, 05, 06, 07, 08, 09, 15, 22, 23, 26, 27, (31, 32), 33, 36, 37, 38, 39, 40, 41, 53, 54, 55, 58, 59, 62, 63, 64, 70, and 72.

Collective GLEs

We noticed 10 groups of *Double GLEs*: (01, 02); (13, 14); (16, 17); (24, 25); (28, 29); (51, 52); (56, 57); (60, 61); (68, 69); and (71b, 71c).

To GLE 71b and GLE 71c relate the events on 7 March 2012 and 13 March 2012 that already have not autonomous numbering. In such a manner we have a total of 20 double GLEs.

In Table 7 there are also three groups of *Triple GLEs* (10, 11, 12); (43, 44, 45); (65, 66, and 67) and one group of *Quadruple GLEs* (47, 48, 49, and 50).

The recapitulation is as follows:

31 sGLE + 20 double GLEs + 9 triple GLEs + 4 quadruple GLEs = 64 GLEs

Recurrent GLEs

The remaining events are the recurrent GLEs, covering the following 10 groups: (18, 19); (20, 21); (28, 30); (29, 30); (34, 35); (42, 43); (42, 44); (42, 45); (42, 46); and (71c, 71).

It is noteworthy that the events GLE 31 and GLE 32 might appear as recurrent as the delay between them is about five solar rotational periods of 27 days. So to the abovementioned 10 groups of GLEs, probably should be added and this 11th recurrent GLE group (31, 32).

Multi-stage GLEs - recurrent-collective, collective-recurrent, and other complex GLE groups

In Table 7 are observed and the more complex combined groups. For example the GLE group (42, 43, 44, 45, and 46) represents a group of *Recurrent-collective GLEs* (rcGLEs) and the GLE groups (28, 29, and 30) and (71b, 71c, and 71) present *Collective-recurrent GLEs* (crGLEs) (Table 6).

It can be argued that the multi-stage GLE group (42, 43, 44, 45, and 46) represents a group of *Recurrent-collective-recurrent GLEs* (rcrGLEs). This is a new multi-stage GLE series.

Statistics of types and groups of GLEs

The analysis of Table 7 shows that the 31 single GLEs represent only 41.9 % from all 74 GLE events. And if we consider the concerned recurrent GLE group (31, 32), the number of the single GLEs reduces to 29, i.e. 39.2 % from all GLEs.

The number of the collective GLEs is 33 (20 double, 9 triple and 4 quadruple GLEs), which makes the relative number 44.6 % from all 74 GLEs. These types of GLEs dominate over single GLEs.

The number of the recurrent GLEs is 20 (or 22 with the group 31, 32), making 27 % (or 29.7 %) from all 74 GLE events.

Geophysical and applied aspects of GLE effects

The high energetic protons of SCRs that are guided into the middle latitude and Polar Regions collide with atmospheric constituents and release their energy through the process of ionization [3–5]. The majority of the energy is extinguished in the lower region of the ionosphere (around 50÷80 km in altitude), stratosphere (10÷50 km) and troposphere (0÷10 km) .

The ionospheric area is particularly important for propagation of radio waves and communications in wide frequency range because this is the area where the most of the absorption of radio signal energy occurs. The enhanced ionization produced by incoming energetic protons increases the absorption levels in the lower ionosphere and can have the effect of completely blocking all ionospheric radio communications through the polar regions. Such events, the so called Polar Cap Absorption (PCA) events commence and last as long as the energy of incoming protons at approximately greater than 10 MeV exceeds roughly 10 pfu (1 pfu = 1 particle.cm⁻²s⁻¹sr⁻¹) at geosynchronous satellite altitudes.

The relativistic solar particles of GLEs are substantial in many others geophysical processes owing to their ionizing effect, for instance the effects of ozone layer depletion [27, 28], the generation of nitrogen (NOx) and hydrogen (HOx) oxides, generation of cosmogenic isotopes, sudden disturbances in the global atmospheric electrical circuit (GAEC) and many others.

Conclusions

The present article is an attempt to contribute to the detailed investigations of poorly studied SCR/GLE events. These events initiate a nucleonic-electromagnetic cascades in the Earth's atmosphere [1, 7–12], affecting its physicochemical properties and ion balance [1, 27, 28]. Our consideration indicates that GLEs during registration period (1942-2015) have a complicated distribution (Table 1) and occurrence rate (Table 2). In 14 cases are seen collective GLEs (Table 4), in 10 cases there are recurrent GLEs (Table 5) and also more

complex combined groups – recurrent-collective GLEs (rcGLEs), collective-recurrent GLEs (crGLEs), and recurrent-collective-recurrent GLEs (rcrGLEs) (Table 6). In Table 7 are presented all ground level enhancements (from GLE 01 to GLE 72) during the whole period (1942-2015) of investigation of these events. There are identified also the single GLEs. Here are included as well four contenders for GLEs in the current solar cycle 24. Really these are quasi GLEs (qGLEs). The credibility of so indicated groups, however, should be carefully analyzed further. But in all cases one can say confidently that the contribution of the collective GLEs, recurrent GLEs, and other more complex GLE groups, dominates over the contribution of the simple GLE events – sGLEs. This demonstrates that the GLE events in most cases are not single, separate and individual, but joint and group phenomenon.

The SCR/GLE events are not the main source of geophysical disturbances (as compared, e.g., to coronal mass ejections and geomagnetic storms) [15]. However, the arrival of SCRs, the enhancement of the flux of accelerated charged particles (solar protons, helium ions and heavier HZE nuclei) in the Earth's environment and the corresponding appearance of GLEs, can be a sporadic but considerable trigger component of the global mechanism of solar-terrestrial relations.

References

1. Dorman, L.I. *Cosmic Rays in the Earth's Atmosphere and Underground*, Dordrecht, The Netherlands, Kluwer Academic Publishers, 2004.
2. Miroshnichenko, L.I. *Solar Cosmic Rays*, Dordrecht, The Netherlands, Kluwer Academic Publishers, 2001.
3. Velinov, P.I.Y. Expressions for ionizing capability due to sub-relativistic solar cosmic rays with anisotropic and isotropic penetration in the ionosphere and atmosphere. *C. R. Acad. Bulg. Sci.*, 2015, 68 (1), 79–88.
4. Velinov, P.I.Y. Ionization capability and ionization yield function of cosmic rays at their interaction with the atmospheres of Earth and planets. *C. R. Acad. Bulg. Sci.*, 2014, 67 (7), 987–994.
5. Velinov, P.I.Y. Ionization capability and yield functions of subrelativistic cosmic rays in planetary ionospheres and atmospheres. *C. R. Acad. Bulg. Sci.*, 2014, 67 (10), 1395–1400.
6. Usoskin, I.G., A. Ibragimov, M.A. Shea, D.F. Smart. Database of Ground Level Enhancements (GLE) of high energy solar proton events. Report 054 on the 34th International Cosmic Ray Conference, 30 July - 6 August, 2015, The Hague, The Netherlands. http://pos.sissa.it/archive/conferences/236/054/ICRC2015_054.pdf
7. Mishev, A., P.I.Y. Velinov, L. Mateev. Ion production rate profiles in the atmosphere due to solar energetic particles on 28 October 2003 obtained with CORSIKA 6.52 simulations. *C. R. Acad. Bulg. Sci.*, 2011, 64 (6), 859–866.

8. Mishev, A., P.I.Y. Velinov. Renormalized ionization yield function y for different nuclei obtained with full Monte Carlo simulations. *C. R. Acad. Bulg. Sci.*, 2011, 64 (7), 997–1006.
9. Mishev, A., P.I.Y. Velinov. Contribution of cosmic ray nuclei of solar and galactic origin to atmospheric ionization during SEP event on 20 January 2005. *C. R. Acad. Bulg. Sci.*, 2012, 65 (3), 373–380.
10. Mishev, A., P.I.Y. Velinov. A maverick GLE 70 in solar minimum. calculations of enhanced ionization in the atmosphere due to relativistic solar energetic particles. *C. R. Acad. Bulg. Sci.*, 2013, 66 (10), 1457–1462.
11. Mishev, A., P. I. Y. Velinov. Ionization rate profiles due to solar and galactic cosmic rays during GLE 59 Bastille day 14 July, 2000. *C. R. Acad. Bulg. Sci.*, 2015, 68 (3), 359–366.
12. Mishev, A., P.I.Y. Velinov. Determination of medium time scale ionization effects at various altitudes in the stratosphere and troposphere during ground level enhancement due to solar cosmic rays on 13.12.2006 (GLE 70). *C. R. Acad. Bulg. Sci.*, 2015, 68 (11), 1427–1432.
13. Forbush, S.E. Three unusual cosmic ray intensity increases due to charged particles from the Sun, *Phys. Rev.*, 1946, 70 (9/10), 771–772.
14. Lange, I., S.E. Forbush. Further note on the effect on cosmic ray intensity of the magnetic storm of March 1, 1942, *Terr. Magn. Atmos. Electr.*, 1942, 47 (4), 331–334.
15. Miroshnichenko, L.I., E.V. Vashenyuk, J.A. Pérez Peraza. Solar cosmic rays: 70 years of ground based observations. *Geomagn. Aeronomy*, 2013, 53 (5), 541–560.
16. Forbush, S.E., T.D. Stinchcomb, M. Schein. The extraordinary increase of cosmic ray intensity on November 19, 1949, *Phys. Rev.*, 1950, 79, 501–504.
17. Mishev, A., P.I.Y. Velinov. Influence of low energy hadron interaction models on ionization due to CR heavy nuclei. *C. R. Acad. Bulg. Sci.*, 2014, 67 (6), 843–84.
18. Velinov, P.I.Y. Formulas for ionization yield functions and ionization capability of solar cosmic rays in the ionosphere and atmosphere. *C. R. Acad. Bulg. Sci.*, 2014, 67 (11), 1555–1560.
19. Velinov, P.I.Y., S. Asenovski, L. Mateev. Improved COsmic Ray Ionization Model for Ionosphere and Atmosphere (CORIMIA) with account of 6 characteristic intervals. *C. R. Acad. Bulg. Sci.*, 2012, 65 (8), 1137–1144.
20. Asenovski, S., P. I. Y. Velinov, L. Mateev. Determination of the spectra and ionization of anomalous cosmic rays in polar atmosphere, *C.R. Acad. Bulg. Sci.*, 2013, 66 (6), 865–870.
21. Velinov, P. I. Y., S. Asenovski, L. Mateev. Ionization of anomalous cosmic rays in ionosphere and middle atmosphere simulated by CORIMIA Code. *C. R. Acad. Bulg. Sci.*, 2012, 65 (9), 1261–1268.
22. Abunina, M., A. Abunin, A. Belov, S. Gaidash, Y. Tassev *et al.* Properties of magnetic fields in coronal holes and geoeffective disturbances in solar cycle 24. *C.R. Acad. Bulg. Sci.*, 2014, 67 (5), 699–704.
23. Gopalswamy, N., P. Mäkelä, S. Yashiro, H. Xie, S. Akiyama, N. Thakur. High-energy solar particle events in cycle 24, *J. Phys.: Conf. Ser.*, 2015, 642, 012012.

24. Thakur, N., N. Gopalswamy, H. Xie, P. Makela, S. Yashiro, S. Akiyama, J. M. Davila. Ground level enhancement in the 2014 January 6 solar energetic particle event, *Astrophys. J. Lett.*, 2014, 790, L13 (5pp), doi:10.1088/2041-8205/790/1/L13
25. Gopalswamy, N. (2011) in Proc. of 7th International Workshop on Planetary, Solar, and Heliospheric Radio Emissions VII (PRE VII), ed. H. O. Rucker, W. S. Kurth, P. Loran, & G. Fischer, Vienna: Austrian Academy of Sciences Press, 325.
26. Belov, A., E. Eroshenko, O. Kryakunova, N. Nikolayevskiy, A. Malimbayev, I. Tsepakina, V. Yanke. Possible ground level enhancements at the beginning of the maximum of Solar Cycle 24, *J. Phys.: Conf. Ser.*, 2015, 632, 012063.
27. Kilifarska, N. An autocatalytic cycle for ozone production in lower stratosphere initiated by galactic cosmic rays. *C. R. Acad. Bulg. Sci.*, 2013, 66 (2), 243–252.
28. Kilifarska, N., V. Bakmutov, G. Melnyk, Energy particle influence on southern hemisphere ozone variability. *C. R. Acad. Bulg. Sci.*, 2013, 66 (11), 1613–1622.

РАЗШИРЕНА КАТЕГОРИЗАЦИЯ НА ПОВИШЕНИЯТА НА КОСМИЧЕСКИТЕ ЛЪЧИ НА ЗЕМНАТА ПОВЪРХНОСТ (GLEs) ПОРОДЕНИ ОТ ВИСОКОЕНЕРГИЙНИ СЛЪНЧЕВИ ЧАСТИЦИ

П. Велинов

Резюме

Явлението “увеличение на потока космически лъчи на нивото на земята”, т.н. ground level enhancement (GLE), вследствие проникването на слънчеви енергийни частици, има важно значение за редица процеси на Земята. Слънчевите частици са ключът за разбирането на слънчево-земните връзки и космическото време. Въз основа на наземните наблюдения на GLE от 28 февруари 1942 (когато са открити) до края на 2015 г., сме определили някои характерни техни периоди през време на слънчевите цикли 17÷24. Направено е количествено изследване на GLE и е определена честотата на възникването им в различните слънчеви цикли. В работата е представена и една категоризация на изследваните явления (от първото GLE 01 на 28 февруари 1942 до последното GLE 72 на 6 януари 2014 г.) вследствие на слънчевите енергийни частици, достигащи земната повърхност. Установени са нови групи на колективни, рекурентни, рекурентно-колективни, колективно-рекурентни и др. GLEs през време на изследвания период. Обсъдени са също така редица физически, методически и приложни аспекти, свързани със събитията GLE, защото те имат екстремално въздействие върху Земята. Получените резултати имат прогностична стойност и значение за йонизационните и радиационни условия на околната среда и за механизмите на слънчево-земните въздействия.

BLACK HOLE THERMODYNAMICS FOR PRODUCING HORIZON OSCILLATIONS

Alexander Yosifov, Lachezar Filipov¹

¹*Space Research and Technology Institute – Bulgarian Academy of Sciences
e-mail: alexander_yosifov@abv.bg, lfilipov@mail.space.bas.bg*

Abstract

We present a scenario for addressing the information loss problem in black holes which preserves the unitarity of the S-matrix. Our approach is based on quantizing the curvature singularity using classical non-commutative geometry. Also we take advantage of the developments in unification of quantum mechanics and gravity to provide a two-dimensional holographic description of the event horizon. Hence we discretize the holographic screen (horizon) into individual pixels, Planck area in size, each carrying a degree of freedom. We provide a generic phenomenon which arises naturally from black hole perturbation theory to produce a remnant-free final stage evolution and omit the necessity of introducing an additional membrane, as it has been proposed by Susskind. A stronger version of the Page's argument regarding the no-cloning theorem is considered.

Introduction

The 'black hole information loss' paradox conjectured by Hawking in 1974 [1] states that during the black hole formation and evaporation process the quantum-mechanical unitarity is violated. Thus a pure state, given by the density matrix

$$(1) \quad \rho = |\psi\rangle\langle\psi|$$

evolves into a mixed state described by the density matrix

$$(2) \quad \rho = \sum_{n=1}^N \rho_n |\psi_n\rangle\langle\psi_n|$$

When a black hole is formed in a semiclassical background geometry the strong gravitational dynamics act on the quantum vacuum, creating high frequency outgoing modes, which are radiated away to infinity, and the black hole evaporates. The model suggests the emitted Hawking particles carry large amount of entropy S , given by

$$(3) \quad S = M^2 / M_p^2$$

where M_p^2 is the Planck mass, have black body thermal spectrum of temperature $T_H = \kappa / 2\pi$ and carry next-to-nothing information about the initial

quantum state of the matter which undergoes gravitational collapse, hence $\Delta I = -\Delta S$. The thermal nature of the radiated Hawking quanta implies it does not depend on the internal microstates but rather on the geometry outside the black hole, thus its mass, M_{BH} . The vicinity of the black hole is just a part of the whole quantum system which means some of the correlations remain in the interior region and causality limits the accessibility for an outside observer. In this view it is impossible, even in principle, to reconstruct the initial state.

Any solution to the information paradox must address two important results which follow from the loss of unitarity, namely the pure-to-mixed state evolution and the time-irreversibility (T-asymmetry) of the map between the past and future null infinity regions, denoted as \mathcal{I}^- and \mathcal{I}^+ , respectively. The fundamental nature of the paradox pushes us in a direction towards abandoning a physical principle that up until now we have believed to understand. Recent developments in AdS/CFT correspondence [2–4] and holography [5–7] strongly advocate the fundamentally non-local universe view. The extreme conditions created by the strong gravitational dynamics in the process of black hole formation/evaporation further bolster the hypothesis. In our efforts to preserve the unitary evolution of the S-matrix, the overwhelming opinion is that in high energy regimes ($\geq M_P$) certain non-local features occur. Thus in super-Planckian physics we should observe violations of the locality/causality which govern quantum field theory

$$(4) \quad [\varphi(x), \varphi(y)] = 0$$

where $(x - y)^2 > 0$.

We present a scenario for preserving unitarity without involving exotic physics. The model we propose eliminates the infinities which arise from the singularity region, thus allowing us to establish a complete T-symmetry between \mathcal{I}^- and \mathcal{I}^+ . Furthermore, we put forward a mechanism which naturally follows from black hole thermodynamics and causes instability in the end-stage evolution of the system, hence leading to a complete remnant-free evaporation.

The article is organized as follows. In ‘Redefining the singularity’ section we develop our model by describing the requirements for preserving unitarity. We redefine the problematic singularity region by quantizing it with the use of non-commutative geometry. In ‘Holographic pixilation and horizon oscillations’ section we apply the holographic principle to the event horizon and define the notion of “pixel”. Applying holography (pixelating) to the horizon allows us to present a natural oscillating conjecture that we believe emerges as an effect of matter perturbations. The proposed conjecture could account for the membrane in complementarity [8] and leads to a late-time explosion due to certain instabilities which arise from black hole thermodynamics. In ‘Black hole evaporation and information storing’ section we put forward a method for storing the information

regarding an infalling matter onto the vacuum in the vicinity of the hole and establish symmetry between the past and future null infinities. In the ‘Conclusions’ we summarize the work.

Redefining the singularity

In the present Section we consider non-commutative geometry as a method for avoiding the formation of a singularity, in a spherically symmetric solutions, to the Einstein vacuum equations. The simplest solution of such type is the Schwarzschild metric

$$(4) \quad ds^2 = -(1 - 2M/r)dt^2 + (1 - 2M/r)^{-1} dr^2 + r^2(d\theta^2 + \sin^2\theta d\phi^2)$$

In the particular metric the event horizon is located at $r=2M$ and the singularity is at $r=0$. We suppose the Schwarzschild black hole settles rapidly to a quasi-stationary state, entirely parameterized by mass, angular momentum and charge, given by M , J , and Q , respectively. The quasistationarity is because of the monotonic thermal emission due to the strong gravity effects on the quantum fields.

The current definition of a singularity as infinitely dense point-like "object" leads to certain major problems such as temperature divergence at the black hole endpoint (big curvature), $R \rightarrow \infty$ as $r \rightarrow 0$ and complete breakdown of general relativity at short distance scales. It further leads to geodesic incompleteness in the interior region as $r \rightarrow 0$, and is thus responsible for the information loss problem. It has been argued that non-commutative (NC) geometry can cure all of the above problems by introducing a minimal length scale, hence removing the point-like zero-size "objects", $a(t) = 0$.

We quantize the singularity by first presenting the non-commutative nature of space-time in terms of the commutator

$$(5) \quad [x^\mu, x^\nu] = i\Theta^{\mu\nu}$$

where $\Theta^{\mu\nu}$ is the anti-symmetric matrix (non-commutative operator), with dimensionality of $(length)^2$, and places the minimal length scale of $\sqrt{\Theta} \sim 10^{-17} cm$. Here x^μ and x^ν are coordinate operators where $\mu, \nu \rightarrow 1, 2, 3$. We believe non-commutativity is an integral part of the manifold. NC geometry removes the point-like objects and favors the smeared over particular radius ones. The notion comes from its possible interpretation as a gravitational analog of the uncertainty principle. When we replace the delta-function by a Gaussian distribution the matter source is given by

$$(6) \quad \rho(r) = \frac{M}{(4\pi\Theta)^{3/2}} \exp(-r^2/4\Theta)$$

in $D = 4$ dimensions, where M is the mass of the source which is no longer concentrated in a region of zero size $a(t) = 0$, but is rather smeared across a region the size of the minimum length scale, $\sqrt{\theta}$. Once we have introduced the limit $\sqrt{\theta}$, and have established that the notion of point-like objects is no longer relevant in that context, we argue the infinities associated with singularity disappear. Thus as we consider the singularity as a gravitational source, it could be represented as

$$(7) \quad M(r) = 4\pi \int_0^r \rho(x)x^2 dx$$

where $\rho > 0$. Therefore we obtain finiteness of mass given by

$$(8) \quad m = 4\pi \int_0^\infty \rho(r)r^2 dr$$

Because of the finiteness of the parameters, any density source will effectively vanish as $r \rightarrow \infty$. Indeed we find that by using non-commutative geometry we can redefine the otherwise problematic physical singularity. Therefore we have got rid of the infinities and get a nice constant curvature which at $r = 0$ is described by the *Ricci* scalar

$$(9) \quad R(0) = \left(\frac{4M}{\sqrt{\pi\theta^{3/2}}} \right)$$

Once we apply NC quantization to the singularity region we cure the temperature divergence at the black hole endpoint, and thus assign a finite value to the curvature scalar R , as $r \rightarrow 0$. Detailed calculations have been carried out in [9, 10].

The framework we have provided deals with the pathological problems by eliminating the infinities and the curvature divergence. However, the effects of non-commutativity on large scales are negligible. It has been argued the given model substitutes the singularity region with the so-called *De Sitter* core which is characterized by finite-value parameters and exhibits repulsive gravity features. Therefore, the strong energy condition $(T_{\mu\nu} - \frac{1}{2}Tg_{\mu\nu})X^\mu X^\nu \geq 0$, is violated in this newly defined singularity region. Violations of the strong energy condition are present in many models and should not be taken as a surprise. We believe every potential solution to the information loss problem should address the problematic matter by either singularity quantization or different approaches.

Holographic pixilation and horizon oscillations

In this section we apply the holographic principle [5, 6] to quantize the event horizon into pixels. Pixelizing the horizon is akin to placing a Planck grid onto it,

where each cell (pixel) is of size l_p^2 , where $l_p^2 = 2.59 * 10^{-66} \text{cm}^2$. We argue the holographic interpretation of the horizon combined with the redefined notion of singularity (see preceding section) give a generic method for producing Planckian-amplitude horizon oscillations which substitute the physical membrane in the complementarity conjecture [8]. Moreover, in the context of perturbation theory the proposed horizon oscillations lead to a remnant-free explosion of the hole due to thermodynamic instabilities in the final stage of the evaporation.

By performing a coordinate transformation we can map 3D space into 2D

$$(10) \quad x^\mu = \begin{pmatrix} x^i \\ x^j \\ x^k \end{pmatrix} \rightarrow x^\mu = \begin{pmatrix} x^i \\ x^j \end{pmatrix}$$

By that simple operation we project 3D bulk physics to a 2D holographic screen at a rate of bit per l_p^2 . We define a *bit* as a binary degree of freedom or simply a two-state system which describes a classical unit of information. In the current framework, each pixel can host a single bit of information. The two states, that each pixel could be in, represented in terms of vectors have the form $\begin{pmatrix} 1 \\ 0 \end{pmatrix}$ and $\begin{pmatrix} 0 \\ 1 \end{pmatrix}$ for excited (on) and vacuum state (off), respectively. A one-pixel state is given by

$$(11) \quad |\Psi \rangle = \left(\frac{1}{\sqrt{2}}\right)(|on \rangle + |off \rangle)$$

Hence a pixel on a holographic screen can be either thermally excited or in a vacuum state. Each Planck cell is limited by the uncertainty principle and the cosmic censorship conjecture by the M_p . Therefore a surface of area A , consisting of N number of pixels can be interpreted as N -state system. Thus a black hole with surface area A will be described as N -state system which obeys the *Bekenstein-Hawking* area/entropy law in Planck units, $S = A/4l_p^2$, where $l_p^2 = G$. Therefore the number of different states the whole system can be in N , is given by the logarithm of the dimensions of the Hilbert space \mathcal{H}

$$(12) \quad N = \ln \dim(\mathcal{H})$$

In a way, N is the minimum required number of bits to describe a given system. The horizon-related entropy S , measures the lack of information about the collapsed matter as far as an observer in the $r > 2M$ region is concerned. The fate of an infalling matter as it crosses the event horizon and approaches the singularity (dS core) is examined in Fig. 1.

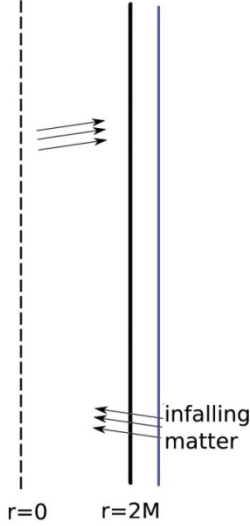


Fig. 1. Black hole in Eddington-Finkelstein coordinates. The dashed line ($r = 0$) is the singularity. The bold black vertical line denoted as $r = 2M$ is the event horizon. The blue line indicates the position of the horizon as it oscillates. The amplitude is Planckian, thus the horizon oscillates a Planck length in outward direction from $r = 2M$.

We make a simple assumption which can be interpreted as a stronger version of Page's argument. The conjecture provides an even tighter security for the no-cloning theorem. In fact, one does not have to wait for half of the black hole's mass to have evaporated in order to be able to retrieve a single bit. Suppose we use classical black hole mechanics to describe the perturbations

$$(13) \quad dM = \frac{\kappa}{8\pi} \delta A + \Omega \delta J$$

where κ is the surface gravity, Ω is the angular velocity and J is the angular momentum. We may define the no-back reaction conjecture as lack of perturbations on the metric due to quantum fields and fluctuations. As matter crosses the $r = 2M$ region (horizon) there will be no perturbations to the background metric. Such will be observed only after the infalling matter reaches $r = 0$, gets thermalized, and then gets embedded onto the holographic screen. Information no longer gets destroyed as it reaches the singularity due to its redefined nature. As we have argued in previous section the strong energy condition can be violated in the presence of significant gravity dynamics. Violation of the condition leads to repulsive gravity behavior by the gravitational field. Therefore, as infalling matter hits the singularity it gets thermalized (vacuumized) and reflected back towards the horizon where it will be embedded. The time for the

thermalized matter to get embedded onto the horizon is of order the scrambling time t_s , where $t_s = R \ln((R/l_p)/(\ell))$. Therefore in no scenario can the linearity of quantum mechanics be violated. An integral part of the black hole formation/evaporation process is the transformation of fine-grained degrees of freedom into coarse-grained degrees of freedom and vice versa. Moreover as the vacuumized (high energetic) matter gets embedded onto the holographic screen, it takes it out of its vacuum state, and thus causes the Planckian oscillations. The frequency of the oscillations obeys the simple relation

$$(14) \quad \omega = \sqrt{\frac{-T_{\mu\nu}}{M_{BH}}}$$

where $T_{\mu\nu}$ is the energy/momentum tensor (Hawking radiation) and M is the mass of the black hole. The minus sign indicates the black hole adiabatically loses mass. Small value of $T_{\mu\nu}$ would imply the hole is massive. This follows from the straightforward relation $T = 1/M$. Thus, a massive black hole would oscillate with lower frequency. Another way of stating the above conjecture would be

$$(15) \quad \frac{d^2 A(t)}{dt^2} = -T_{\mu\nu}$$

The oscillations do not lead to violations of the equivalence principle because of their Planckian amplitude and relatively low frequency throughout the black hole evolution. They can only become noticeable at the final stage of the evaporation process when the whole system becomes thermodynamically unstable. An observer close to the horizon will measure classical Unruh vacuum with no deviations. In fact, until the black hole reaches its lower mass bound the stress tensor will not diverge. However, as $T \rightarrow M_p$ the black hole explodes due to the present instabilities. Hence no timeslice with drama for the observer can be constructed.

We argue that the physical membrane in black hole complementarity can be substituted by the natural oscillations of the horizon. When a black hole is described by a distant observer the entropy of the hole S_{BH} , is viewed to arise from the fine-grained degrees of freedom on the stretched horizon. As it has been shown in [8] the stretched horizon is located a l_p away from the event horizon in outward direction. Therefore, each point from the event horizon is projected (corresponds) onto the membrane. Thus, the entropy of the global horizon equals the entropy of the stretched horizon, $S_{horizon} = S_{stretched} = A/4l_p^2$ which obeys the Bekenstein/Hawking entropy bound. Since there is equality between the degrees of freedom of the global horizon and the stretched horizon, we argue the oscillations conjecture omits the need for a membrane. Hence an observer at infinity can falsely interpret the horizon oscillations as a physical membrane located just outside the $r = 2M$ region.

We further suggest the generic oscillations can easily lead to a complete evaporation. As the black hole loses mass, in accordance with (14), the frequency of the oscillations ω and thus its temperature T , will monotonically increase. As we have already argued the proposed scenario does not lead to violations of the equivalence principle. However, as T becomes of order M_P , the whole system becomes thermodynamically unstable and the black hole explodes leaving no remnant behind. This view was first suggested by Hawking concerning primordial black holes of approximate mass $\sim 10^{15}g$ produced by quantum fluctuations in the early Universe [11]. The basic calculations behind particle production in curved spacetime are also provided. The proposed final-stage explosion releases in an instant the remaining of the information. It should be noted there is nothing that prevents complete remnant-free evaporation from occurring. The contemporary models fail to address the question of how to evaporate the singularity without presenting remnants which are equally troubling. The proposed remnants, stable or quasi-stable, must be able to carry infinitely many states so they can reproduce the initial quantum state of the matter that has collapsed to form a black hole. The amount of entropy the remnants should be able to carry is of order M^2/M_P^2 in Planck units, where M is the mass of the collapsing matter. In the proposed picture, however, since we have given a mechanism for quantizing the singularity region (removing the infinities), we have cured the pathological problems, hence there is nothing, in principle, to prevent the $r = 0$ region from evaporating.

Black hole evaporation and information storing

In the present Section we examine black hole evaporation and discuss a possible way for storing the information of an infalling matter.

The evaporation process is due to the strong gravitational dynamics acting on the quantum fields which thus leads to amplification of the energy density of the quantum fluctuations. Hence outgoing modes are radiated to infinity. The calculations suggest the emitted Hawking particles are purely thermal with black body thermal spectrum of $T = (\kappa/2\pi)$, which implies they do not carry information about the initial quantum state of the infalling matter [12]. The thermal radiation depends solely on the fixed background metric of the hole. It is in no way correlated with the interior microstates. As matter, in a certain quantum state $|\psi\rangle$, falls in, the Hilbert space \mathcal{H} , partitions into two independent Hilbert spaces for the interior and exterior region of the black hole, given respectively by \mathcal{H}_{in} and \mathcal{H}_{out} , which are uncorrelated.

$$(16) \quad \mathcal{H} \rightarrow \mathcal{H}_{in} \otimes \mathcal{H}_{out}$$

Because causality/locality limits the correlations between the independent Hilbert spaces, the outgoing modes are of thermal spectrum.

We have so far only addressed one of the aspects which we believe every potential solution to the information loss problem should tackle, namely the geodesic divergence in the $r < 2M$ region, and have only partly touched on the second issue - establishing T-symmetry between the \mathcal{J}^- and \mathcal{J}^+ regions, Fig. 2.

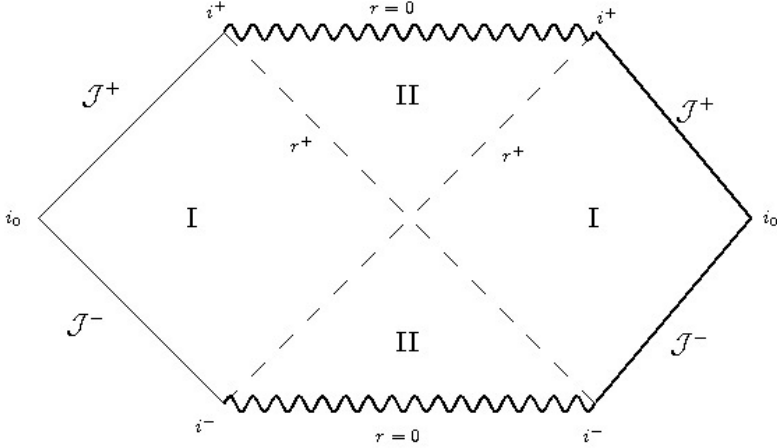


Fig. 2. Penrose diagram for the time-reversibility between \mathcal{J}^- and \mathcal{J}^+

As it has been recently argued the uniqueness of the vacuum might be an effective field theory [13, 14]. Thus any non-local fundamental framework reduces to classical local quantum field theory in low-energy regimes. Tracing radiation back from I^+ to the source (horizon) should not result in high-energetic excitations in the near-horizon region. Instead, one finds slight deviations from the unique Minkowski vacuum. Therefore there must be various states, locally indistinguishable, all energetically degenerate. In the provided framework a semiclassical black hole consists of many vacuum states $|\psi_n\rangle$ where $n = 1, 2, 3 \dots A/4$ in Planck units. The number agrees with the Bekenstein-Hawking area/entropy bound. In fact, vacuum degeneracy implies the number of different vacua in the region surrounding the black hole is given by the exponential of the Bekenstein bound

$$(17) \quad |\psi_n\rangle = \exp[A / 4l_P^2]$$

where $A = 16\pi M^2 l_P^4$. As far as an infalling observer is concerned the vacuum in the vicinity of the horizon is unique. Moreover the equivalence principle (no drama) holds and an accelerated observer should not encounter any deviations from the Unruh vacuum. Furthermore non-uniqueness of the vacuum allows for the possibility of information to be stored on it and later be encoded in the outgoing

Hawking radiation. Hence the degenerate vacuum surrounding the black hole should be able to store information without getting energetically excited.

That being said, we argue that as matter falls inside a black hole it leaves or imprints the information regarding its initial quantum state onto the degenerate vacuum. This should leave the classical perturbations given by Eq. (13) unchanged. Therefore, as the black hole radiates thermal Hawking particles, they "pick up" information from the vacuum. In principle, information about infalling matter could be found in the emitted Hawking radiation. However, description of the exact mechanism by which the quanta "pick up" the information requires a working theory of quantum gravity, and it appears to be beyond our scope as of now.

The proposed mechanism establishes time-symmetric (T-symmetry) map between \mathcal{J}^- and \mathcal{J}^+ . The two regions become completely identical. All of the information at I^- can be obtained from I^+ and vice versa.

Conclusions

We have provided a model which addresses both of the issues that contemporary resolution proposals suffer from. Namely, the geodesic divergence (incompleteness) and T-asymmetry between \mathcal{J}^- and \mathcal{J}^+ . By using classical non-commutative geometry we are able to cure the pathological problems of the singularity region. The framework also redefines the singularity by attributing repulsive gravity features to it. Also we get rid of infinities associated with $r = 0$. In the proposed picture information no longer gets destroyed as it reaches the singularity but rather gets thermalized (vacuumized). By combining this proposal with the holographic description of the horizon we are able to present a phenomenon which, we believe, arise naturally. The conjectured Planckian-amplitude horizon oscillations not only account for the physical membrane proposed in black hole complementarity, thus omitting the necessity of its very existence, but also take care of the late-time evolution of the system by leading to final-stage explosion which does not leave remnants behind. The put-forward vacuum degeneracy surrounding the black hole stores the information about infalling matter. This way the emitted particles are of thermal spectrum and "pick up" the information, hence get certain quantum corrections, if you will. Therefore we make the \mathcal{J}^- and \mathcal{J}^+ regions identical (time-symmetric) and preserve the unitarity of the S-matrix.

References

1. Hawking, S.W., Breakdown of Predictability in Gravitational Collapse, Phys. Rev. D 14, 2460 (1976).
2. Maldacena, J. M., The large n limit of superconformal field theories and supergravity, Adv. Theor. Math. Phys. 2 (1998) 231–252, hep-th/9711200.

3. Gubser, S.S., I.R. Klebanov, and A.M. Polyakov, Gauge theory correlators from non-critical string theory, Phys. Lett. 1998, B428, 105–114, hep-th/9802109.
4. Witten, E., Anti-de sitter space and holography, Adv. Theor. Math. Phys. 2 (1998) 253–291, hep-th/9802150.
5. Hooft, G. The Holographic Principle, arXiv:hep-th/0003004v2.
6. Bousso, R., The Holographic Principle, Rev. Mod. Phys. 2002, 74, 825–874.
7. Banks, T., Holographic space-time and its phenomenological implications, Int. J. Mod. Phys. 2010, A25, 4875–4887.
8. Susskind, L., Thorlacius L., Uglum J. The stretched horizon and black hole complementarity. Physical Review D: Particles and Fields. 48, 3743–3761. PMID 10016649, DOI: 10.1103/PhysRevD.48.3743.
9. Nicolini, P., Anais Smailagic, Euro Spallucci, Noncommutative geometry inspired Schwarzschild black hole, DOI: 10.1016/j.physletb.2005.11.004.
10. Arraut, I., D. Batic, M. Nowakowski, Maximal extension of the Schwarzschild spacetime inspired by noncommutative geometry, arXiv:1001.2226v1 [gr-qc].
11. Hawking, S.W., Black Hole Explosions? Nature. 1974, 248, 30–31; DOI: 10.1038/248030a0.
12. Hawking, S. W., Particle creation by black holes, Phys. 1975, 43, 199–220.
13. Hossenfelder, S., Comment on the black hole firewall, arXiv:1210.5317v1 [gr-qc].
14. Hawking, S.W., M.J. Perry, A. Strominger, Soft Hair on Black Holes, Phys. Rev. Lett. 116, 231–301.

ТЕРМОДИНАМИКА НА ЧЕРНИ ДУПКИ КАТО ПРИЧИНА ЗА ТРЕПТЕНИЯ НА ХОРИЗОНТА

А. Йосифов, Л. Филипов

Резюме

Представяме модел за решение на информационния парадокс при черни дупки, който запазва унитарността на S-матрицата. Подходът ни се базира на квантизиране на сингулярността, използвайки класическия некомутативна геометрия. Също така използване напредъка в опитите за унифициране на квантова механика и гравитация, за да представим холографско описание на хоризонта. Тоест, квантизираме холографския екран (хоризонт) на индивидуални „пиксели“, с размер на Планк, всеки от които носи по един бит информация. Предлагаме класически феномен, който произтича от пертурбационна теория за черни дупки и води до безостатъчен финален етап, като също така и премахва необходимостта от представяне на допълнителна физическа мембрана, както бе предложено от Съскинд. Предлага се и по-добра версия на аргумента на Пейдж, отнасяща се до теоремата за клониране на квантова информация.

HORIZON OSCILLATIONS FOR PRESERVING THE EQUIVALENCE PRINCIPLE

Alexander Yosifov, Lachezar Filipov¹

¹*Space Research and Technology Institute – Bulgarian Academy of Sciences
e-mail: alexander_yosifov@abv.bg, lfilipov@space.bas.bg*

Abstract

We present a generic phenomenon which provides a set of boundary conditions for preservation of the effective field theory after Page time. We further argue the proposed scenario can account for the physical membrane in the complementarity conjecture as far as an outside observer at future null infinity is concerned.

Introduction

Recently, it has been argued by AMPS [1] there is an inconsistency between the postulates of black hole complementarity [2] which causes drama for an infalling observer after half of the mass has been evaporated. The three postulates are given as follows. The absence of drama for an infalling observer is also mentioned in [2], and has been established in the literature as a fourth postulate.

Postulate 1: The process of formation and evaporation of a black hole, as viewed by a distant observer, can be described entirely within the context of standard quantum theory. In particular, there exists a unitary S–matrix which describes the evolution from infalling matter to outgoing Hawking-like radiation.

Postulate 2: Outside the stretched horizon of a massive black hole, physics can be described to good approximation by a set of semiclassical field equations.

Postulate 3: To a distant observer, a black hole appears to be a quantum system with discrete energy levels. The dimension of the subspace of states describing a black hole of mass M is the exponential of the Bekenstein entropy $S(M)$.

Postulate 4: A freely falling observer experiences nothing out of the ordinary when crossing the horizon.

We wish to preserve unitarity in accordance with Postulate 1

$$(1) \quad \rho = |\psi\rangle\langle\psi|$$

Following the semiclassical approximation, stated in Postulate 2, combined with the desired information preservation in Postulate 1, we see that an infalling observer should encounter high-energy quanta at the horizon, Fig. 1.

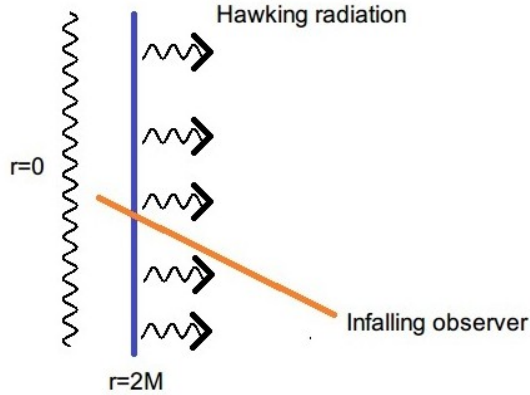


Fig. 1. Black hole in Eddington-Finkelstein coordinates. The wave-like line ($r=0$) is the singularity. The event horizon is depicted by the solid blue line. The solid orange line depicts an infalling observer.

However, according to Postulate 4, there should be absence of drama for an infalling observer. Hence the observer should measure the ground state with no deviations from the classical Unruh vacuum. Suppose an infalling observer is counting the high-energy modes with a measuring apparatus. Following Postulate 4, the expectation value should be zero, $N_i = 0$, where $N_i = a_i^\dagger a_i$. As AMPS have pointed out, this statement appears to be in contradiction with our nomenclature regarding quantum field theory in curved spacetime (Postulate 2). As Hawking has explicitly shown in his semiclassical calculations [3] the strong gravitational field acts on the quantum vacuum and polarizes the virtual particle pairs. The number of the produced particles which are radiated away to infinity is thus given by

$$(2) \quad \langle 0 | a_i^\dagger a_i | 0 \rangle = \sum_i |\beta_i|^2$$

By finding the value of β we approximate the number of the emitted quanta. As it follows from black hole perturbation theory [4, 5] as the hole evaporates it loses mass which leads to an increase of the temperature, and thus faster evaporation rate. Although the value of β is small, the effects of the black hole's mass on the matter fields add up during the course of evaporation, and should be significant after Page time. Therefore, after half of the black hole has evaporated the number of out-modes, that an infalling observer carrying measuring apparatus will count, should be non-zero, hence causing drama and contradicting Postulate 4.

Because of the contradiction between the postulates of complementarity, AMPS argue the following three statements cannot all be true:

- (i) Purity of the emitted Hawking quanta.
- (ii) Absence of drama for an infalling observer.
- (iii) Semiclassical physics in the vicinity of the black hole.

Oscillations as stretched horizon

We address the question of what boundary conditions need to be present at the vicinity of the event horizon in order to avoid formation of a firewall for a sufficiently old black hole. As it has been argued in Sec. I, AMPS' argument leads to violation of the no-drama principle after Page time if there is an entanglement, i.e. maximal correlation, between early- and late-time Hawking radiation. It has been shown in [6] that disentangling the quantum vacuum in the near-horizon region by introducing certain boundary conditions preserves the effective field theory for old black holes. The imposed boundary conditions have to meet certain requirements, namely to change the correlation between the in- and out-modes without affecting the thermal spectrum of the radiation emitted to I^+ , and preserve the conservation of momentum. Even small deviations from the purely thermal spectrum of the Hawking particles will lead to stress-energy divergence due to the large blueshift which occurs when an observer at I^+ traces the particles to the origin. In that case, $T_{\mu\nu} \rightarrow \infty$ as $r \rightarrow 2M$.

As it has been suggested in [2, 6] as far as a far away observer is concerned there is a stretched horizon (physical membrane) located l_p away from the global horizon ($r = 2M$) in outward direction. The proposed membrane acts as a partially reflecting mirror with the following characteristic

$$(3) \quad \Phi_{out} - \Phi_{in} = 0$$

where *in* and *out* stand for coming from I^- and radiated to I^+ , respectively. Thus an observer at I^+ can obtain all of the information from I^- and vice versa. The reflective property implies we preserve the unitary evolution of the S-matrix and establish time-symmetric map between past and future null infinity. As a result the stress-energy tensor is normalized. That being said, the conditions imposed in [6] lead to polarization of the particle pairs solely on one side of the horizon, either $r < 2M$ or $r > 2M$, and hence break the trans-horizon correlations.

We argue the Planckian-amplitude horizon oscillations [7] can generically account for the suggested boundary conditions. The conjectured oscillations arise naturally from perturbation theory. The effect is argued to be caused by transformation of coarse-grained degrees of freedom into fine-grained degrees of freedom which is an integral part of the black hole formation/evaporation process. Furthermore, the frequency of the oscillations solely depends on the mass of the hole

$$(4) \quad \omega = \sqrt{\frac{-T_{\mu\nu}}{M}}$$

where $T_{\mu\nu}$ is the emitted Hawking radiation and M is the mass of the black hole. We suppose the horizon oscillations can account for both, vacuum disentanglement and the partially reflecting boundary surface.

Let's suppose we have a spherically symmetric collapse given by the Schwarzschild metric

$$(5) \quad ds^2 = -(1 - (2M/r)dt^2 + (1 - 2M/r)^{-1}dr^2 + r^2(d\theta^2 + \sin^2\theta d\phi^2)$$

In the context of complementarity an observer at I^+ would measure the entropy of the black hole to emerge from the fine-grained degrees of freedom outside the global horizon (stretched horizon). As it has been argued in [2] each point from the global horizon ($r = 2M$) is projected onto a physical membrane located a l_p away. Hence the whole surface is shifted by order of δ , where δ is a small positive constant. Therefore the entropy of the event horizon equals the entropy of the stretched horizon which obey the Bekenstein bound in Planck units, $S_{horizon} = S_{stretched} = A/4$. Because of the established equality we argue the oscillations can account for the physical membrane as far as an observer at I^+ is concerned.

Since the black hole polarizes the quantum vacuum in the vicinity of its horizon, we argue the proposed oscillations are sufficient to produce the desired effect, namely the particle pairs remain in either the interior or exterior region thus breaking up the vacuum entanglement. Suppose we have a collapse in initially pure state

$$(6) \quad |\psi\rangle = \sum_i |\psi\rangle \otimes |i\rangle$$

where $|\psi\rangle \in \mathcal{H}_{out}$ and $|i\rangle \in \mathcal{H}_{in}$. Here \mathcal{H}_{out} and \mathcal{H}_{in} stand for radiation emitted to infinity and radiation close to the horizon, respectively. For a black hole after Page time we assume $|\psi\rangle \gg |i\rangle$. If we interpret the radiated Hawking particles in terms of Hilbert spaces, we get $dim(\mathcal{H}_{out}) \gtrsim dim(\mathcal{H}_{in})$ [8]. That being said, when an observer at I^+ traces the Hawking quanta back to the origin no deviations will be observed due to the purely thermal spectrum of the emission. Moreover, when the out-modes are traced back no membrane will be present. As far as a close-by observer is concerned infalling matter is not reflected by a stretched horizon, and crosses the $r = 2M$ region with no drama. We argue there will be discrepancy between the reference-based description of order t_s , where $t_s = R \ln(R/l_p)$, due to the lack of perturbation to the background metric caused by infalling matter. A close-by observer should see matter being radiated away from the global horizon, hence being reflected by the singularity region (dS core) [7] of order t_s later.

So far we have provided a complementary description of the physical membrane, and have shown how the conjectured horizon oscillations can account for it. However, we still have not addressed the question of what causes the infalling matter reflection, as reported by an observer at I^+ .

Spherically symmetric solutions to Einstein field equations describe generic collapse with the horizon region being a flat plane with no special dynamics. Quantum vacuum in asymptotically flat spacetime with a boundary surface leads to ambiguity (Casimir effect). Thus the number of measured eigenstates $a_i^\dagger a_i$, will be observer dependent. Let's suppose we have a pair of observers, Alice and Bob, each carrying a measuring apparatus, where Alice is close to the event horizon, and Bob is far away. We expect Alice and Bob to disagree on the number of the produced eigenstates in the near-horizon region

$$(7) \quad \varphi = \sum_i (a_i^\dagger f_i^* + a_i f_i)$$

$$(8) \quad \varphi = \sum_i (b_i^\dagger f_i^* + b_i f_i)$$

hence they measure different number of particles, $N_A \neq N_B$. It has been suggested in [9, 10] that tracing back the outgoing modes from I^+ to the horizon will result in various vacua, all locally indistinguishable (vacuum degeneracy). The observer close to the horizon, i.e. Alice, will not encounter high-energy particles but rather Unruh vacuum (Postulate 2). The number of different vacua, $|\psi_n\rangle$ surrounding the horizon is given by the exponential of the Bekenstein-Hawking area/entropy bound in Planck units, $\exp[A/4]$. The number $|\psi_n\rangle$, equals the entropy of the global horizon $S_{horizon}$, and therefore the entropy of the stretched horizon $S_{stretched}$. The effective uniqueness of the quantum vacuum allows for information to be stored onto it without getting energetically excited (Postulate 4). That being said, we argue that a distant observer, i.e. Bob, can falsely interpret the information stored onto the degenerate vacuum as a partially reflective surface. As far as Bob is concerned, infalling matter gets thermalized, and reflected back by the stretched horizon. Moreover, the out-modes emitted to infinity are also seen to originate from the physical membrane, from the perspective of an observer at I^+ . For Alice, however, who is at proper distance r from the black hole nothing unusual happens. Infalling matter experiences no drama, and the Hawking particles are emitted from the global horizon ($r = 2M$).

Conclusion

We have shown that the generic phenomena of Planckian-amplitude horizon oscillations can account for the stretched horizon proposed in black hole complementarity, and also provide the necessary conditions for breaking up the entanglement between early- and late-time Hawking particles; thus preventing the

formation of a firewall after Page time. The conjectured oscillations follow from classical black hole perturbation theory. The model builds on the complementary picture given by Susskind by providing natural explanation of its basic features.

References

1. Almheiri, A., D. Marolf, J. Polchinski, and J. Sully, Black Holes: Complementarity or Firewalls?, *J. High Energ. Phys.*, 10.1007/JHEP02(2013)062.
2. Susskind, L., L. Thorlacius, J. Uglum. The stretched horizon and black hole complementarity. *Physical Review D: Particles and Fields*. 48, 3743–3761. PMID: 10016649, DOI: 10.1103/PhysRevD.48.3743.
3. Hawking, S. W., Particle creation by black holes, *Phys.* 43, 199220 (1975).
4. Paolo Pani, *Advanced Methods in Black-Hole Perturbation Theory*, arXiv:1305.6759v2 [gr-qc].
5. Mino, Y., M. Sasaki, M. Shibata, H. Tagoshi, and T. Tanaka, *Black Hole Perturbation*, *Prog. Theor. Phys. Suppl.* 1997, 128, 1–121.
6. Hossenfelder, S., *Disentangling the Black Hole Vacuum*, *Phys. Rev. D*. 2015, 91(4) 044015. DOI: 10.1103/PhysRevD.91.044015
7. Yosifov, A., and L. Filipov, *Black Hole Horizon Oscillations*, *Aerospace Research in Bulgaria*, 2016, 28, 19–31.
8. Nomura, Y., J. Varela, and S.J. Weinberg, *Complementarity Endures: No Firewall for an Infalling Observer*, arXiv:1207.6626v4 [hep-th].
9. Hawking, S.W., M.J. Perry, and A. Strominger, *Soft Hair on Black Holes*, *Phys. Rev. Lett.* 2016, 116(23), 231301. DOI: 10.1103/PhysRevLett.116.231301
10. Hossenfelder, S. *Comment on the black hole firewall*, arXiv:1210.5317v1 [gr-qc].

ТРЕПТЕНИЯ НА ХОРИЗОНТА ЗА ЗАПАЗВАНЕ НА ПРИНЦИПА НА ЕКВИВАЛЕНТНОСТТА

А. Йосифов, Л. Филипов

Резюме

Представяме принцип, който описва група от гранични условия за запазване на ефективната теория на полетата след време на Пейдж. Също така предлагаме сценарий, който описва физическата мембрана от комплементарността при черни дупки, без да е наличен разгънат хоризонт от гледна точка на отдалечен наблюдател.

“LIULIN-ISS-2” SYSTEM FOR COSMONAUTS’ DOSIMETRIC CONTROL IN THE ISS RADIATION ENVIRONMENT

**Tsvetan Dachev¹, Borislav Tomov¹, Yuri Matviichuk¹,
Plamen Dimitrov¹, Vyiacheslav Shurshakov², Victor Benghin²,
Elena Yarmanova², Olga Ivanova², Igor Nikolaev³**

¹Space Research and Technology Institute – Bulgarian Academy of Sciences

²Institute of Biomedical Problems – Russian Academy of Science

³S.P. Korolev Rocket and Space Corporation “Energia”, Russia
e-mail: tdachev@bas.bg

Abstract

Under a collaboration agreement between Space Research and Technology Institute, Bulgarian Academy of Sciences (SRTI–BAS), Institute of Biomedical Problems, Russian Academy of Sciences (IBP–RAS) and S.P. Korolev Rocket and Space Corporation “Energia” an engineering model of new system named “Liulin-ISS-2”, for personal dosimetric control of Russian cosmonauts inside and outside ISS, was developed. It is expected that the new system will replace the Liulin-ISS system, launched to ISS in September 2005. The “Liulin-ISS-2” priority is focused on the active measurement with 10 seconds resolution of the dose rate dynamics from Galactic Cosmic Rays (GCR), protons from internal and energetic electrons from external radiation belts, and solar energetic particles (SEP) inside ISS modules and during the extravehicular activity (EVA) of Russian and international cosmonauts. The significance of dose measurements for EVA was formulized during the analysis of the large and rapid variations in space and time of the doses obtained simultaneously at two different locations outside the ISS [1]. Liulin-ISS-2 system consists of 4 portable dosimeters (PD) and interface block (IB) with internal dosimeter. The PD sized 66×56×26 mm is based on the traditional Liulin type DES block diagram with 2 cm² square and 0.3 mm depth PIN diode. The analysis of the obtained deposited energy spectra will be performed according the ideas for intelligent crew personal dosimeter [3] and the new experience obtained during the data analysis from the R3DR2 instrument outside ISS in the period October 2014–January 2016. A SAFT prismatic lithium-Ion rechargeable battery, endorsed for space use, is used in the PD and allows more than 7 days independent work of the PD with 10 sec resolution. Thermostat and manageable heater are implemented to keep the temperature of the PIN diode not lower than -20 °C during EVA when is situated in the cosmonauts’ spacesuit pocket. The PD can work independently on ID by using USB connection and special software with any other PC. The interface block (size 265×178×85 mm) is based on a Getac T800 (<http://www.getac.com/>) fully rugged tablet PC in compliance with the requirements and procedures of MIL-STD-810G, and under Windows-8 operational system. Through eight-port industrial USB hub the tablet PC manages the system and data transfer toward CAN serial interface and/or flash memory stick. Continuously the last 90 minutes of data, obtained with the internal dosimeter, are visualized on the screen of the tablet PC. These data can be used by the cosmonauts and the radiation control personal for fast analysis of the radiation risk for astronauts during solar proton events.

1. Introduction

1.1. Purpose of “Liulin-ISS-2” instrument

The purpose of performing the development of the “Liulin-ISS-2” is the creation of dosimetric equipment for operational individual monitoring of the crew aboard the Russian segment of the International Space Station (ISS), both in the compartments and outside the ISS. Dosimeter "Liulin-ISS-2" priority is focused on the active measurement of dose rate dynamics with 10 s resolution of the energetic protons and electrons from internal and outer Earth's Radiation Belts (RB) during ExtraVehicular Activity (EVA) in the cosmonauts' space suit pocket. Similar measurements on the ISS have not been carried out yet.

According to the results of measurements that were carried out previously on the external surface of the ISS with two devices R3DE/R [1] – they are similar to dosimeter "Liulin-ISS-2" described in this article – it was concluded the possibility of large (more than an order of magnitude) and rapid (within ~ 10 s) dose rate variations caused by different shielding of the detectors and anisotropy of the radiation sources.

The R3DE/R instruments' results can be interpreted as the possible doses received by astronauts and cosmonauts during EVA, because the shielding of the R3DE/R detectors is close to the value of shielding of the space suits of the Russian and American cosmonauts and astronauts [2]. Tooling solution was proposed in [3], where on the basis of analysis of the shape of the energy spectrum and the relationship of dose to the flux (specific dose), is feasible in principle to distinguish between the predominant sources of cosmic radiation on the ISS orbit and calculate the equivalent dose for them. These ideas were confirmed during the latest experiment on ISS with the R3DR2 instrument in the period October 2014–January 2016 [4]. The dosimeter "Liulin-ISS-2" will apply the basic instrument and software developments, which were made in the papers [4, 5].

1.2. Analysis of the research object and the state of the art

Cosmic radiation is an unavoidable factor in spaceflight, which it is impossible to eliminate, due to restrictions on weight, power consumption and other spacecraft resources. In connection with the proposed future expansion of space activities (missions to asteroids and to the Moon, interplanetary manned missions, etc..) and, as a consequence, an increase in terms of human presence on board the spacecraft importance of this factor will steadily increase. At the present time the usual stay of astronauts on the ISS is months-long, as well as holding a number of flights during the career. In addition, there are plans in the near future to carry out a manned mission to Mars, which implies a long-term stay of the person in space.

The essential point in the planning and development of long-term space flight is the impact of radiation on the crew [6–8], the dose received by an astronaut in a space flight, associated with the effect of various radiation sources.

1.2.1. Galactic Cosmic Ray (GCR)

A Galactic Cosmic Ray (GCR) consists of protons and heavy nuclei – practically the entire periodic table of elements of D.I. Mendeleev. The GCR particles are accelerated in the depths of space to energies at which the particles penetrate through casing spacecraft, creating at the same time in the nuclear reactions secondary charged particles and neutrons.

The amplitude changes of GCR intensity during solar cycle phase for different energies is different. For example, for $E_p \sim 100 \sim \text{MeV}$ it reaches 100 %, whereas for $E_p \geq 2 \div 3 \text{ GeV}$ its magnitude does not exceed 1 \div 2 %. Integral flow GCR ($10^6 \div 10^{21} \text{ eV}$) in interplanetary space is changed under the influence of solar modulation, and near the Earth's orbit is $J(\text{GCR}) = 2 \div 4.5 \text{ cm}^{-2} \text{ s}^{-1}$, the minimum GCR flux value is realized in the period of the SA maximum, and the maximum - in minimum period.

In the near-Earth space, due to the shielding effect of the Earth GCR flux, decreases 2 times, and even additional attenuation GCR flux occurs due to the conditions of entry into the geomagnetic field. The flow of GCR particles in Earth orbit outside the magnetosphere with a high degree of accuracy can be considered isotropic.

In terms of dynamic performance, the FCL can be attributed to sources of chronic exposure of biological objects. GCR dose rate inside the ISS at altitude of 400 km and inclination 51.6° can be estimated as $100 \div 200 \mu\text{Gy day}^{-1}$. Due to the hard spectrum absorbed dose of the GCR varies slightly with the thickness of the protection.

1.2.2. Inner Radiation Belt (IRB)

High-energy charged particles are trapped by the Earth's magnetic field and form two distinct belts of toroidal shapes surrounding the Earth. These are called radiation belts (RB). The IRB is situated at an altitude of 0.2 \div 2.0 Earth radii and consists of both electrons, with energies of up to 10 MeV, and protons with energies of up to 700 MeV. Outside of the ISS, the IRB energetic protons delivered the highest daily dose rates.

During an analysis of the R3DE and R3DR data, it was discovered that the US space shuttle dockings with ISS decreased the IRB dose rate delivered by IRB 30 \div 150 MeV proton fluxes [9]. The effect was attributed to the additional shielding provided by the 78-ton shuttle.

1.2.3. Outer Radiation Belt (ORB)

The Outer Radiation Belt (ORB) is located in the altitudinal range of 3.4÷10 Earth radii. The ORB population is electrons with energies > 10 MeV. The first observations of the ORB relativistic electron fluxes in the ISS were made in 2001 with a Liulin-E094 instrument (Dachev et al., 2002a; Reitz et al., 2005) inside the US laboratory module. The effects of the relatively small ORB dose rates were not fully understood in 2002. ORB relativistic electron fluxes were observed with Liulin DES type instruments flown on ISS and LEO satellites [10–12]. The ORB daily dose rate was practically zero on magnetic quiet days, but reached maximum dose rates up to $288.40 \mu\text{Gy h}^{-1}$ in the disturbed periods after magnetic storms.

1.2.3. Solar Energetic Particles (SEP)

Solar flares, caused by sporadic eruptions in the chromosphere and corona of the Sun, produced high fluxes of charged solar energetic particles (SEP) with energies up to several GeV. We measured the characteristics of SEP from September till October 1989 inside the Russian space station “MIR” with the first Liulin type instrument [13] and with the Liulin-5 dosimetric telescope (DT) inside the ISS in March 2012 [14]. With the R3DR2 instrument, we performed one of the first SEP measurements outside of the ISS [15]. The highest SEP hourly dose rate measured during the EXPOSE-R2 mission was $5251 \mu\text{Gy h}^{-1}$ on June 22, 2015. Historically the SEP measurements inside the ISS are rare, but have been discussed in [16, 17].

2. Instrumentation

The engineering model of the “Liulin-ISS-2” instrument consists of three units: 2 portable dosimeters (PD) and 1 interface block (IB) with one stationary dosimeter inside (Fig. 1).



Fig. 1. External view of “Liulin-ISS-2” instrument

2.1. “Liulin-ISS-2” interface block (IB) description

The interface block (IB) is situated in a black painted aluminum box sized 265×178×85 mm with weight of about 3 kg. On the upper panel of the IB is seen the Getac-T800 type (URL: <http://www.getac.com/>) fully rugged tablet personal computer (PC). There are 3 LED indicators and 6 buttons seen on the right side of the IB, which serve the PC management. The touch screen of the PC is foreseen to be switched OFF in the most of the time in space. The cosmonaut may see the information on the screen after simple touch of it.

Two portable dosimeters are seen connected with USB cables to the IB. The two more USB cable, which may be seen on Fig. 1, are foreseen for the extension of the engineering model up to a system with 4 portable dosimeters.

On the right panel of the IB (Fig. 2.) are mounted from left to right as follows: the ground bolt; the 7-pin 28 V power connector; the 10-pin Controller Area Network (CAN) interface connector; the Universal Serial Bus (USB) connector for flash memory stick connection; 2 fuses; the 28 V power ON/OFF switch and the green Light Emitting Diode (LED), which indicate when the power switch is in position ON. (All labels on the engineering model are preliminary. During the final development of it, these labels will be replaced with better made permanent labels.)



Fig. 2. External view of the right panel of the IB

The whole “Liulin-ISS-2” system and IB are managed by the Getac-T800 type tablet PC in compliance with the requirements and procedures of MIL-STD-810G, and under Windows-8 operational system (OS). Except the PC in the IB are situated the following blocks: DC/DC converter from 22÷32 V to 19 V, which supplies with power the tablet PC; 4 DC/DC converters from 8.4 V to 5 V, which powered the PD and charged their batteries; 8-port USB hub, which communicate upstream with the tablet PC and with 7 downstream USB devices as follows: 4 PD, 1 internal dosimeter (ID), 1 USB-controller area network (CAN) bus module, and 1 USB flash drive (Fig. 3).

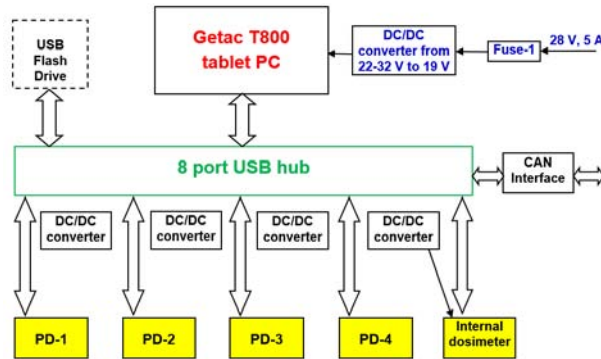


Fig. 3. Block-diagram of “Liulin-ISS-2” instrument

2.2. Description of “Liulin-ISS-2” dosimeters

The design of the internal and portable dosimeters-spectrometers of the engineering model of “Liulin-ISS-2” instrument is not new. Recently published paper by [18] includes list and description of all the experiments carried out with the participation of SRTI-BAS for measuring cosmic radiation from 1988 to August 2014 using dosimeters similar to these in “Liulin-ISS-2” on satellite, rocket, balloons, and aircraft.

The external view of the portable dosimeters is seen in Fig. 4a. It is situated in an oxidised aluminium box with size 66×56×26 mm and weight of 0.135 kg. Below the upper panel of PD (Fig. 4b) are mounted the ON/OFF switch, the red status LED, and the USB mini female connector. Below the panel is situated the space qualified SAFT rechargeable lithium-ion battery MP 144350 type. It is foreseen an opportunity for change of the battery by removing of the upper panel by unscrewing the 2 bolts.

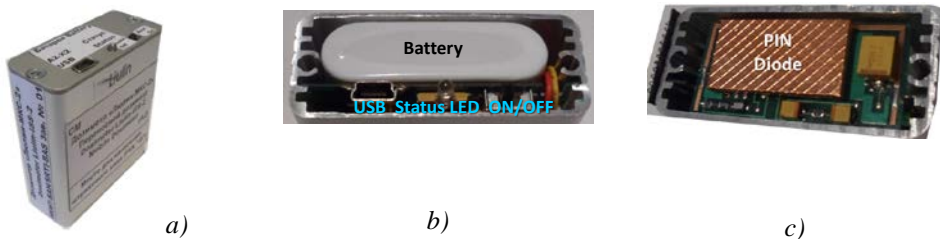


Fig. 4: a) External view of the “Liulin-ISS-2” PD, b) view below upper panel of PD, c) view below lower panel of PD

Below the 0.5 mm thick bottom panel of PD (Fig. 4c) is situated the 2 cm² PIN diode detector. In addition, there is a technological shielding of 0.07 mm copper and 0.2 mm plastic material, which provide total shielding of 0.25 g cm⁻². The calculated required kinetic energies of normally falling particles to the detector are 0.67 and 12.5 MeV for electrons and protons, respectively (URL: <https://www.nist.gov/pml/stopping-power-range-tables-electrons-protons-and-helium-ions>). This indicates that only protons and electrons with energies higher than the values listed above can cross the PD shielding materials and reach the surface of the detector.

The “Liulin-ISS-2” portable dosimeters and the IB internal dosimeter are Liulin type deposited energy spectrometers (DES), which use one silicon detector to measure the deposited energy and number of particles that allow calculating the dose rate and particle flux.

On Fig. 5 is presented the block diagram of the engineering model of “Liulin-ISS-2” portable dosimeters. The internal dosimeter contains only some of the blocks: semiconductor detector, charge-sensitive preamplifier, a fast 256 bits analogue-to-digital converter (ADC), discriminator, and 2 microcontrollers. It is managed directly by the PC through the USB port and its deposited energy spectra are stored in the PC also.

The PD consists of all blocks seen in Fig. 5 but are managed only by one microcontroller. Except the mentioned, in the internal dosimeter blocks, they consist of: 2 MB flash memory to store the spectra, clock-calendar, battery charge controller, and SAFT rechargeable battery. Thermostat and manageable heater are implemented to keep the temperature of the PIN diode detector not smaller than -20 °C during EVA when is situated in the cosmonauts’ spacesuit pocket.

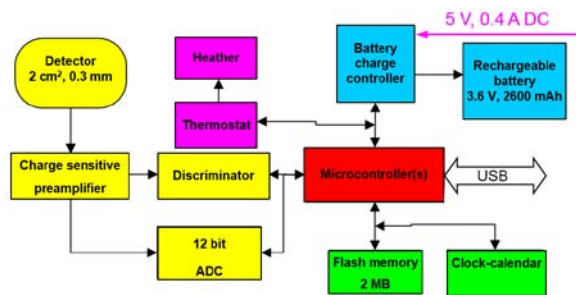


Fig. 5. Block-diagram of “Liulin-ISS-2” dosimeters

3. Dose determination

Pulse analysis technique is used to obtain the deposited energy from each photon/particle crossing partially or fully the silicon detector of the dosimeters. The deposited energies organised in 256 channels form the deposited energy spectrum

for each measurement cycle. It is further used for the calculation of the absorbed dose and flux in the silicon detector from primary and secondary particles. The analysis of the shape of the spectrum and the dose to flux ratio, known also as specific dose (SD), permits the characterization of the predominant radiation source in the DES environment [19].

The internal and external dosimeters are managed by the microcontrollers through specially developed firmware. The ADC and the microcontroller measure organize and keep in RAM memory the 256 channels deposited energy spectra. The microcontroller(s) manages the whole work of the dosimeters and data outputs toward the USB connection.

The main measured parameter in the dosimeters is the amplitude of the pulse after the charge-sensitive preamplifier, generated by a particle or a photon crossing partially or fully the detector. The amplitude of the pulse is proportional by a factor of 240 mV MeV^{-1} to the energy deposited in the detector and to the dose, respectively. By 12 bit ADC these amplitudes are digitized and organized in a 256-channel deposited energy spectrum.

By definition the dose in the silicon detector D_{Si} [Gy] is one Joule deposited in 1 kg of matter. The dosimeters absorbed dose is calculated by dividing the summarized energy deposition in the spectrum in Joules to the mass of the detector in kilograms [20]:

$$(1) \quad D_{Si} [\text{Gy}] = K \sum_{i=1}^{255} (EL_i) [J] / MD [kg]$$

where K is a coefficient, MD is the mass of the detector, and EL_i is the energy loss in Joules in the channel i . The energy in MeV is proportional to the amplitude A of the pulse: $EL_i [\text{MeV}] = A [\text{V}] / 0.24 [\text{V/MeV}]$, where $0.24 [\text{V/MeV}]$ is a coefficient dependent on the preamplifier used and its sensitivity.

All 255 deposited dose values, depending on the deposited energy for one exposure time, form the deposited energy spectrum. The energy channel number 256 accumulates all pulses with amplitudes higher than the upper energy of 20.83 MeV measured by the spectrometer.

On Fig. 6 are shown deposited energy spectra from different calibrations of the DES, which are compared with experimental proton, electron and GCR spectra obtained at aircraft altitudes and spacecraft orbit. The individual spectra seen in the figure are obtained after averaging various numbers of primary spectra and are plotted in coordinates as deposited energy per channel/deposited per channel dose rate. This allows for a better understanding of the process of formation of the spectra in different deposited energy ranges. According to Eq. (1) the absorbed dose in Si is the area between the curve of the deposited energy spectrum and the abscissa. That is why from bottom to top each spectra position against the ordinate

axes depends on the value of the deposited dose rates in Si seen in the legend at the top of the figure. The higher the measured dose rate, the higher the position of the spectrum against the ordinate axis, and the greater the area between the spectrum and the abscissa. The lowest line spectrum in Fig. 6 was obtained by Prof. Frantisek Spurny during the calibration of the Liulin-4C Mobile Dosimetry Unit MDU#2, with ^{60}Co as a reference radiation source, at the Nuclear Physics Institute of the Czech Academy of Sciences [19a]. This spectrum is the shortest because the energy of the ^{60}Co gamma emission line is 1.2 MeV. The absolute values of the dose rates obtained from the spectra are in very good agreement with the dose rates calculated using the EGS4 transport code (URL: <http://rcwww.kek.jp/research/egs/>). The values of the measured doses were found to be within 2.8% of the reference value for the ^{137}Cs source and within 8 % of the ^{60}Co source [19a]. The calibrations showed that the DES had high effectiveness with respect to gamma rays, which allowed monitoring of the natural background radiation.

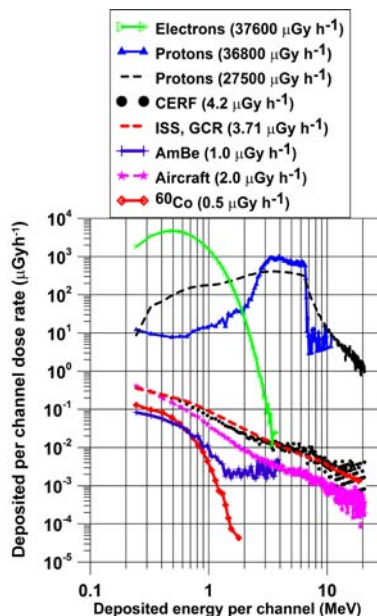


Fig. 6. Different spectral shapes obtained by Liulin-type instruments during calibrations on aircraft and spacecraft

The spectrum denoted by crosses in Fig. 6 was generated by a reference AmBe radiation source emitting neutrons with an average energy of 4.4 MeV. This spectrum continues up to about 4 MeV deposited energy with an obvious change in the slope around 1.2 MeV deposited energy. The neutron sensitivity of the DES

was further studied in the CERN-EU high-energy reference field (CERF) facility, on aircraft and in the near Earth radiation environment.

The spectrum with heavy dots in Fig. 6, obtained in the CERF facility field, contains events in all channels of the DES including the 256th channel, devoted to energy depositions above the upper level of the spectrometer at 20.83 MeV. The events seen below 1 MeV in AmBe and at CERF represent the contribution of low LET radiation (electrons, muons, etc.), while the events above 1 MeV represent the high LET components (protons, neutrons and ions heavier than H⁺). This idea was further developed and allowed calculation of the ambient dose equivalent $H^*(10)$ at aircraft altitudes from the deposited energy spectrum in the Si-detector [21–23].

The CERF energy deposition spectrum is very similar to the averaged aircraft spectrum shown with asterisks in Fig. 6. This spectrum is obtained by averaging Czech Airlines aircraft data during mean solar activity at altitudes close to 10.6 km on routes between Prague and the North American cities New York and Montreal [24]. The ISS R3DE instrument mean GCR deposited energy spectrum (heavy dashed line) has a shape even closer to the CERF spectrum.

Due to the proximity of the spectra in CERF, at the aircraft altitude and at ISS (See the bunch of 3 spectra in the middle of Fig. 6) and using the idea for the 2 parts of spectra, it is possible to be calculated the different sources ambient dose equivalent rate in the dosimeters of the "Liulin-ISS-2" engineering model with the following formulas:

$$(2) \quad H^*(10)_{GCR}[Sv] = \left\{ \sum_{i=1}^{15} (EL_i)[J] / MD[kg] + 5 \sum_{i=16}^{256} (EL_i)[J] / MD[kg] \right\}$$

$$(3) \quad H^*(10)_{IRB}[Sv] = \left\{ \sum_{i=1}^{15} (EL_i)[J] / MD[kg] + 1.3 \sum_{i=16}^{256} (EL_i)[J] / MD[kg] \right\}$$

$$(4) \quad H^*(10)_{ORB}[Sv] = \left\{ \sum_{i=1}^{15} (EL_i)[J] / MD[kg] + \sum_{i=16}^{256} (EL_i)[J] / MD[kg] \right\}$$

We suppose that: the average quality factor of GCR is 5, the IRB protons average quality factor is 1.3 and the energetic electrons in the ORB is 1.

The CERF, ISS and aircraft spectra in Fig. 6 show a similar knee around 6.5÷7 MeV deposited energy. To explain the knee in Fig. 6 a spectrum with heavy triangles was added to the figure. This was obtained during calibrations of DES (non-shielded detector) with a 7.8 MeV protons beam at the cyclotron facility of the University of Louvain, Belgium. The knee seen at about 6.3 MeV corresponds to the point where the incident energy of the normally incident beam on a 0.3 mm thick detector is equal to the deposited energy. All normally incident protons with energies less than 6.3 MeV are stopped in the detector.

The light-dashed spectrum in Fig. 6 was obtained by the RADOM instrument on the Chandrayaan-1 satellite by averaging of 60 primary 10-s resolution spectra. This spectrum shows a very similar shape to the cyclotron

facility spectrum (full triangle spectrum) and a knee at the same position. This is because the energy of the inner belt protons falling on the detector is calculated to be 7÷8 MeV, i.e. equal to the energy of the cyclotron facility's monoenergetic protons falling on the non-shielded detector.

The green open triangle spectrum is the highest one in Fig. 6. It was obtained on the Chandrayaan-1 satellite at altitudes of the ORB (22000 km). This spectrum with a predominant electron population is the result of averaging 120 spectra with 10-s resolution. Only the part with deposited energies up to 4.0 MeV is shown.

The DES effectiveness for neutrons depends on their energy, being minimal for neutrons with energy of 0.5 MeV and having a maximum of a few percent for neutrons with energies of 50 MeV in the CERN field [21]. According to the "neutron induced nuclear counter effect" introduced for the Hamamatsu PIN diodes of type S2744-08 [25] almost all DESs used the same type PIN diodes and neutrons could be observed in all channels of the spectrum with a probability at least one order of magnitude higher in the first 15 channels.

4. Radiation source separation example

It is expected that, on ground after the EVA experiments on ISS, using the formulas (1–4) we will be able to separate and analyze the variations of four different radiation sources dose rates obtained by the PD. The current section aims to confirm this and to present the expected values on ISS radiation sources. The methods for sources separation in the internal dosimeter is described in the next section of the article.

The following four primary radiation sources were expected and recognized in the data obtained with the R3DR2 instrument on ISS in the period 24.10.2014–11.01.2016: (i) globally distributed GCR particles and those derived from them; (ii) protons in the SAA region of the IRB; (iii) relativistic electrons and/or *bremsstrahlung* in the high latitudes of the ISS orbit where the ORB is situated; and (iv) solar energetic particles (SEP) in the high latitudes of the ISS orbit. Together with the real SEP particles, a low flux of what were likely to be mostly secondary protons (SP), were observed in the data.

The simplest method for source separation is described by [19]. It is based on the Heffner formulae [26]; The Heffner's formulae were recently published by [19] and shows that the data can be simply split into two parts by using the dose to flux ratio (D/F) or specific dose (SD). When the SD is less than $1.12 \text{ nGy cm}^2 \text{ particle}^{-1}$, the expected predominant type of radiation in a 10 s interval is ORB electrons. When the SD is greater than $1.12 \text{ nGy cm}^2 \text{ particle}^{-1}$, the expected type of radiation is IRB or SEP protons. The GCR source is divided between the two ranges.

The separation statistics of the R3DR2 data show the following results [5]: 441 days were covered; 3,810,240 points were separated; 2398 were lost (0.062 %) or on average less than 6 points per day; and 313 points were counted twice. The average source counts per day were as follows: GCR 7636 points, IRB 573 points, ORB 383 points, SEP counts per 27 days were 148 points; average, SP counts per 414 days (days without real SEP) were 34 points. The number of daily-averaged measurements for the “stable” presented sources are: 7636+573+383+34, or 8626 measurements in total, which were selected from a total of 8640.

In Fig. 7 in 4 panels is represented the end result of the division of 4 radiation sources and their variations for the period October 24, 2014–January 11, 2016 (Preliminary data were published in [4, 5, 27]).

The GCR source average daily doses variations are presented with a thick black line in Fig. 3a. At the top of this panel with red line is shown the variation of *Dst* (Disturbance Storm Time) index (URL: <http://wdc.kugi.kyoto-u.ac.jp/index.html>), which for the days after the beginning of the magnetic storms have negative values, reaching -223 nanoteslas on March 17 and -204 nanoteslas on June 23rd. Well defined correlation between daily-average dose and *Dst* index confirmed a phenomenon of reduction the flux of GCR particles during the main phase of the magnetic storm, known by the term “Forbush decreases”.

A very small almost linear trend of increase was observed in the data for average daily doses of GCR. The minimum value of $\sim 72 \mu\text{Gy d}^{-1}$ was at the beginning of observations in October 2014 and maximum values of $73 \mu\text{Gy d}^{-1}$ was at the end of observations through January 2016. The reason is declining solar activity during the period of observation.

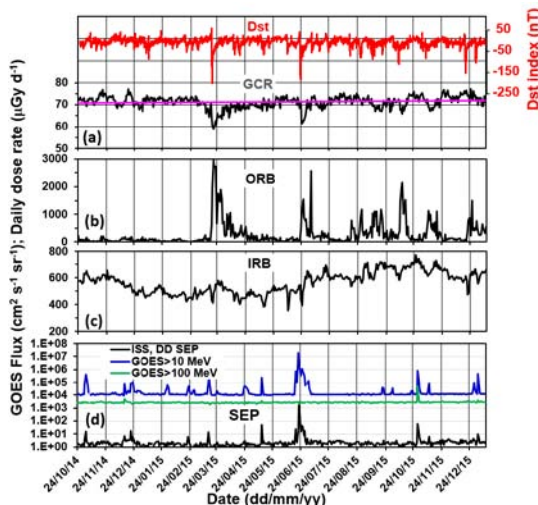


Fig. 7. Radiation sources dynamics as observed on ISS by R3DR2 instrument in the period November 2014–January 2016

The variations in average daily doses of relativistic electrons in ORB are shown in Fig. 3b. Clearly visible are 2 periods in the data. In relatively “quiet” period of geomagnetic activity, between 24 October 2014 and mid-March 2015 the values of average daily doses of relativistic electrons in ORB were relatively small and ranged $2\div 200 \mu\text{Gy d}^{-1}$. In the second period, between mid-March 2015 and the end of observations the fluctuations in average daily doses in ORB are larger and reached values up to about $3000 \mu\text{Gy d}^{-1}$, being in anti-correlation with *Dst* index (red line) in the top panel of Fig. 7. This was in result of the acceleration of electrons and filling the ORB with them.

The next relatively “stable” source of doses outside the ISS was the energy protons in IRB, which are shown by a thick black line in Fig. 3c. The main reason for the long time variation was the correlation with the average altitude of the station above the Earth. Higher doses at the end of the mission are also associated with a lower solar activity, which results in small concentrations in the neutral atmosphere of the earth and respectively to smaller losses from recombination of energetic protons in the IRB.

In Fig. 7d are presented the variations in the average daily dose of SEP and SP measured by R3DR2 on ISS in the period October 24, 2014–January 11, 2016. Along them are shown solar proton fluxes measured in geostationary orbit with the device "Space Environment Monitor" (SEM) (URL: <http://goes.gsfc.nasa.gov/text/databook/section05.pdf>) on the GOES 15 satellite with energies more than 10 MeV (blue curve) and more 100 MeV (green curve). Low dose levels of several $\mu\text{Gy d}^{-1}$ in the lower part of the figure are of secondary protons.

Nine maxima observed in the curve of average daily doses of SEP measured with the device R3DR2 well correlated with the measured with the device SEM flux of protons with energy greater than 10 MeV and 100 MeV on the GOES 15 satellite. The highest peak of nearly $3000 \mu\text{Gy d}^{-1}$ on June 22, 2015 was not observed in the channel with data from GOES 15 with energy greater than 100 MeV. Our doses of June 22, 2015 [15] showed that if you hold a work of astronauts outside the ISS, they would receive more than 2.84 mGy extra dose for six hours and a half, which is identical to the average dose inside the ISS of 15 days [16].

5. "Liulin-ISS-2" engineering model operation

The operation of the "Liulin-ISS-2" instrument starts with two cable connection of the interface block with 5 A 28 V power line and simulator of the CAN interface running on external PC.

The "Liulin-ISS-2" instrument has to be switched ON by the ON/OFF tumbler on the right panel of IB. The green LED there indicates it. Then the tablet PC is switched ON by the right side green button (with a standard network switching symbol) on it (see Fig.1). This starts the loading of the Windows-8 OS

which lasts ~30 s. The "Liulin-ISS-2.exe" application is started automatically, which produce on the tablet PC screen an empty of information screenshot similar to that in Fig. 8. When you first turn ON the "Liulin-ISS-2" dosimeter on ISS the current time will be taken from the PC. After each connection with the CAN communication interface the time is updated with the on-board time automatically.



Fig. 8. Screenshot of empty of information "Liulin-ISS-2"

The internal dosimeter starts to measure with 10-s resolution the current background doses. When on earth their average values are in the range $0.05 \div 0.2 \mu\text{Gy h}^{-1}$, it is simply confirmed the measurements correctness. Each new measurement is displayed on the screen of tablet PC. After 90 minutes of measurements, which is about the time for 1 orbit on ISS, the curve with measured values, displayed on the screen of PC is similar to this seen in Fig. 9. Further the curve on the screen continue to be updated in a dynamical way, i.e. when new value is added at the right side the oldest value in the left side is removed. The values seen in the curve in Fig. 9 are between 0.03 and $4 \mu\text{Sv h}^{-1}/\mu\text{Gy h}^{-1}$. The average value is $0.116 \mu\text{Sv h}^{-1}/\mu\text{Gy h}^{-1}$. These values are normal for the background radiation [27].

The explanation of the tablet PC screenshot content is presented in Fig. 9. (All labels in the screenshot are in Russian. Alternative English language variant is developed also). The English language explanations are black printed around the screenshot. In the bottom of Fig. 9 in three white ovals the begin date/time, the elapsed time and the current time are displayed respectively. The second values are upgraded after each 10-s exposition time interval. In the third one the current time is running with 1-s resolution.

The measured dose rates in the last 10-s are shown in the oval in the upper left corner of the image. The left value of $0.101 \mu\text{Gy h}^{-1}$, situated in blue oval is the absorbed dose rate in the Silicon of the detector. This numeric value is represented graphically with the last seen in the left curve point. It is in $\mu\text{Gy h}^{-1}$ and is calculated by the formula (1). The second value also of 0.101, situated in a red oval, is the calculated by formula (2) ambient dose equivalent dose rate in $\mu\text{Sv h}^{-1}$. We decide to use the GCR formula (2) because the conclusions from the "Dose

determination” section of the article says that the high LET part of the spectra is populated by protons, neutrons, and ions heavier than H⁺.

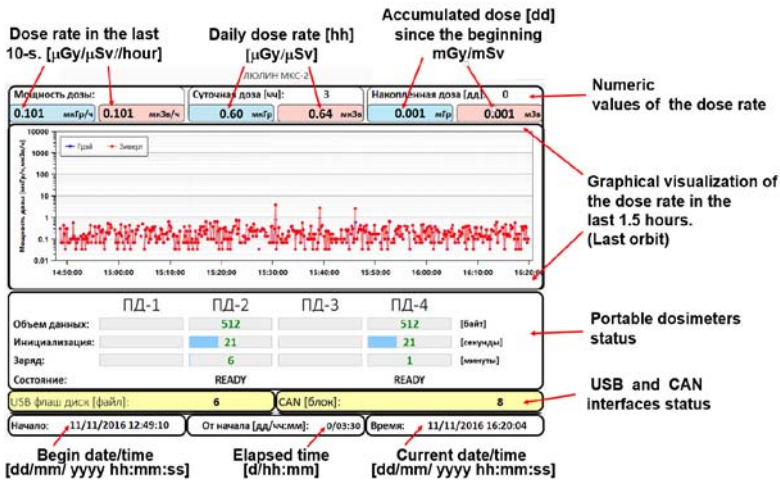


Fig. 9. Explanation of the tablet PC screenshot content

The absorbed dose rates are first plotted in the curve below by blue points and connected also by blue lines. Only 3 blue points are seen in the middle of the graphic. The reason is that the calculated by formula (2) ambient dose equivalent dose rate values in $\mu\text{Sv h}^{-1}$ in the most of the natural background radiation measurements overlap the absorbed dose rate values, which leads that mostly red points and lines are seen in the curve. The ambient dose equivalent rate values are same as the absorbed dose rates because there aren't counts in the high LET part of the spectrum after 15th channel. Only in 3 measurements from about 540, sporadic particles from GCR origin are registered in some of the channels above number 15th and the calculated ambient dose rate red symbols are seen above the blue symbols of the absorbed dose rate in the curve.

The daily absorbed and ambient dose rates measured for 3 hours (3:30 hours precisely) are printed in the middle oval in the upper part of Fig. 9. The value of 0.6 μGy can be obtained by multiplication of the average dose rate of 0.116 $\mu\text{Gy h}^{-1}$ by 1890 measurements for 3 hours and 30 minutes divided by 360 to proceed from $\mu\text{Gy h}^{-1}$ to μGy . The daily ambient dose equivalent rate is a bit larger with a value of 0.64 μSv .

The total accumulated dose rates in mGy and mSv are shown in the oval in the right upper corner of the screenshot in Fig. 9. The two identical values of 0.001 mGy and mSv are the round off value of 0.6 μGy and 0.64 μSv to the upper value.

The two PD has to be connected to IB and switched ON. The PD battery charge starts. Then, the IB automatically reads and stores in the memory file the available data. The PD microcontroller informed IB when the battery is fully charged and this stops the process. The IB clears the PD memory and initiates them with: 1) the current date/time from PC, which is stored and upkeep in the PD clock-calendar; 2) the preselected exposition of 10-s or any other up to 1 h, required by the operator (cosmonaut). The PD has to be switched OFF and then disconnected from IB. After this it is ready to be used in places of interest inside or outside the ISS in a single or multiply sessions. Each new switching ON will produce a new file in the PD connected with the running in the PD clock-calendar. The maximum expected time of independent operation of PD is more than 7 days at 10-s resolution.

The “Portable dosimeters status” fields in Fig. 9 are divided in 4 columns, or one column for each possible PD. In the case of the "Liulin-ISS-2" engineering model only PD#2 and PD#4 are available. In the first row of each PD column the amount of the transmitted to the PC bytes is recorded and it is equal to 512 bytes for each PD. Next row shows that both PD has been initiated for 21 s each. The third row indicates how long in minutes the charging of the batteries up to the “Full charge” continued. Because both PD were almost fully charged the reported charging time is 6 minutes for PD#2 and 1 minute for PD#4. The last row indicates the status of the PD. It is “READY” for both of them, which confirms to the operator (cosmonaut) that each of them is ready to be used again. It has to be switched OFF and disconnected from the USB cable.

The “USB and CAN interfaces status” yellow ovals give information about: 1) how many files has been transmitted toward the removable USB stick. In this case the number of files are 6; 2) how many blocks has been transferred toward the CAN interface. In this case are they are 8.

In Fig. 10a is presented a simulation of a possible 1.5 h curve on ISS. The data from the R3DE instrument outside ISS [11] were obtained on 7 July 2009. Their full day absorbed dose rate curve in seen in Fig. 10b. For a better understanding of the data the brown line in Fig. 10b represents the variations of the ISS geographic latitude (φ) between -51.6° and 51.6° . The blue line meander of data with values between 0.03 and $20 \mu\text{Gy h}^{-1}$ is from the GCR source, while higher value data up to $1570 \mu\text{Gy h}^{-1}$ are from the IRB source. The 4 descending SAA maxima are first seen and second 4 ascending maxima. The simulated on the Fig. 10a data are highlighted with a green rectangle.

The English language screenshot is used in Fig. 10a. The meaning of the data in the ovals in the upper part of Fig 10a is same as already described. The horizontal axes is devoted to the universal time but in this case we use an accelerated in the time variant of the simulating software that is why the values there are not the correct UT values but the time of about 1-minute which represent the used by the software time for the simulation.

The curve represents first relatively low value data from the minimum, observed close to the geomagnetic equator. Next ISS moves to the high North hemisphere high latitudes where the GCR dose rates rise up. Two separate blue and red points and lines are clearly seen there. The blue points are calculated by formula (1), while the red points are calculated by formula (2). As these graphic data on the “Liulin-ISS-2” screen will be used only for visualization, for the separation of the GCR from the IRB data we use simple requirements: all data below $20 \mu\text{Gy h}^{-1}$ are from the GCR source, while all data above are from the IRB source.

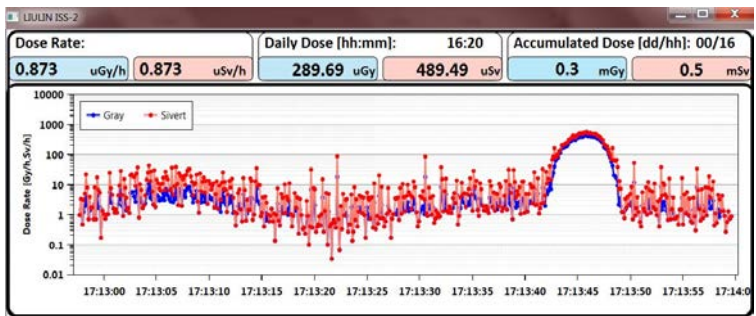


Fig. 10a. Simulation of the expected curve of measurements on ISS for 17 hours and 20 minutes. Real data from the R3DE instrument were used.

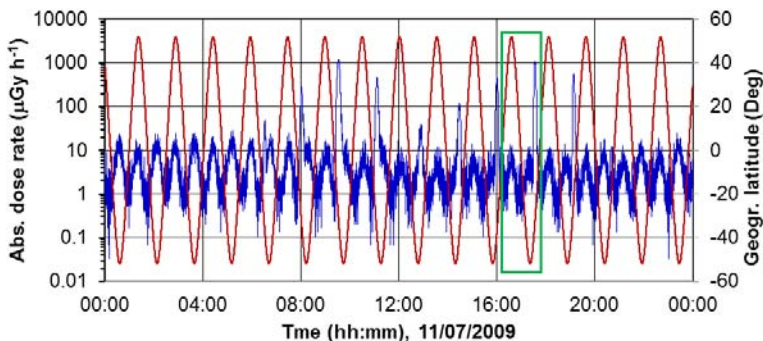


Fig. 10b. Real measured doses on 11 July 2009 by R3DE instrument on ISS

The low level data in the middle of Fig. 10a are from descending crossings of the geomagnetic equator. Next ISS transverses the South hemisphere high latitude region and reaches the SAA region. All data till this point was interpreted as a GCR source and were calculated using formula (2). Fast increase of the absorbed dose rates in the SAA region above $20 \mu\text{Gy h}^{-1}$ switched the formula for calculation toward formula (3) and this is well seen in Fig 10a with relatively close absorbed and ambient equivalent dose rates.

Conclusions

During the period 1989–2016 the Liulin type low mass, dimension and price instruments proved their ability to characterize the radiation environment at the ground, mountain peaks, aircraft, balloon, rocket, and spacecraft. We hope that the newly developed “Liulin-ISS-2” instrument will continue this tradition. If we will succeed to perform with portable dosimeter active measurements during real EVA on ISS this will give important and new information about the real doses from different radiation sources and their fast dynamics.

Acknowledgements

The authors would like to thank: [V. Petrov](#), and [I. Chernykh](#) from IBP–RAS, Moscow, Russia for the long lasting and fruitful scientific cooperation since the development of the first LIULIN instrument in 1986; G. Horneck and G. Reitz from DLR, Institute of Aerospace Medicine, Germany, D.-P. Häder, M. Lebert, and M. Schuster from Department für Biology der Friedrich-Alexander-Universität, Germany for the leadership and cooperation in the experiments on ESA Foton-M2/M3 spacecraft and ISS; [F. Spurny](#), and O. Ploc from Nuclear Physics Institute, Czech Republic for work on the radiological interpretation of Liulin data and for the leadership in the use of Liulin instruments on aircraft; K. Fujitaka, Y. Uchihori, and H. Kitamura from National Institute of Radiological Sciences, Chiba, Japan for the leadership in the calibrations of Liulin instruments on protons and heavy ions; J. Lemaire from Institut d'Aeronomie Spatiale de Belgique for the help in the interpretation of LIULIN data; Gh. Gregoire and H. Schrnitz from Institut de Physique, Universite Catholique de Louvaln, Belgium, for the “Liulin-ISS” calibrations; E.G. Stassinopoulos, former Director of NASA-GSFC Radiation Physics Office, for the support in the “Liulin-3M” calibrations; E. Benton from Department of Physics, Oklahoma State University, USA for the support and NASA balloon data; J. Miller, Lawrence Berkeley National Laboratory, Berkeley, USA for the post-calibrations of LIULIN instrument; ISRO staff and specially to: M. Annadurai, Project Director and J.N. Goswami, Project scientist of Chandrayaan-1 satellite, P. Sreekumar and V. Sharan, Space Astronomy & Instrument Division, ISRO, Bangalore, India for the RADOM instrument support; M.T. Giardi and M. Damasso from Institute of Crystallography–National Research Council, Rome, Italy for the Liulin-Photo cooperation.

References

1. Dachev, Ts. Analysis of the space radiation doses obtained simultaneously at 2 different locations outside ISS, *Adv. Space Res.*, 2013, 52, 1902–10. DOI: 10.1016/j.asr.2013.08.011

2. Benton, E.R., E.V. Benton, A.L. Frank, and M.F. Moyers. Characterization of the radiation shielding properties of US and Russian EVA suits using passive detectors, *Radiation Measurements*, 2006, 41, 1191–1201.
3. Dachev, T., B. Tomov, Y. Matviichuk, P. Dimitrov, G. De Angelis, Y. Uchihori, and O. Ploc. Main Specifications of New Liulin Type Intelligent Crew Personal Dosimeter, *Proceedings of 6th Scientific Conference with International Participation “Space, Ecology, Safety” SES’2010, Sofia, ISSN 1313-3888*, 76–82, 2011, URL: http://www.space.bas.bg/SENS/SES2010/1_SpPh/10.pdf.
4. *Letter to the Editor* Ts.P. Dachev; N.G. Bankov; G. Horneck; D.-P. Häder. *Radiation Protection Dosimetry*, 2016. DOI: 10.1093/rpd/ncw123
5. Dachev, Ts.P., B. T. Tomov, Yu. N. Matviichuk, Pl. G. Dimitrov, N.G. Bankov, G. Horneck, and D.-P. Häder. Overview of the ISS radiation environment observed during EXPOSE-R2 mission in 2014-2016, *Space weather*, 2017. (Submitted)
6. ГОСТ 25645.203-83. Безопасность радиационная экипажа космического аппарата в космическом полете. Модель тела человека для расчета тканевой дозы. Госстандарт, Москва, 1984.
7. Мирошниченко, Л. И., Петров В. М. Динамика радиационных условий в космосе. М., Энергоатомиздат, 148 с., 1985.
8. ICRP Publication 60. Recommendations of the International Commission on Radiological Protection, 1990, Pergamon Press.
9. Dachev, Ts.P., Semkova J., Tomov B., Matviichuk Yu., Dimitrov Pl., Koleva R., Malchev St., Reitz G., Horneck G., Angelis G. De, Häder D.-P., Petrov V., Shurshakov V., Benghin V., Chernykh I., Drobyshev S., and Bankov N.G. Space Shuttle drops down the SAA doses on ISS. *Adv. Space Res.* 47, 2030–38, 2011, DOI: 10.1016/j.asr.2011.01.034
10. Dachev, Ts.P., B.T. Tomov, Yu.N. Matviichuk, P.G. Dimitrov, and N.G. Bankov. Relativistic Electrons High Doses at International Space Station and Foton M2/M3 Satellites. *Adv. Space Res.*, 44, 1433–40, 2009, DOI: 10.1016/j.asr.2009.09.023
11. Dachev, Ts., G. Horneck, D.-P. Häder, M. Lebert, P. Richter, M. Schuster, and R. Demets. Time profile of cosmic radiation exposure during the EXPOSE-E mission: the R3D instrument. *Astrobiology*, 2012, 12(5), 403–411. DOI: 10.1089/ast.2011.0759
12. Dachev, Ts., G. Horneck, and D.-P. Häder, M. Schuster, and M. Lebert. EXPOSE-R cosmic radiation time profile. *Astrobiology*, 2015, 14, 17–25. DOI: 10.1017/S1473550414000093
13. Shurshakov, V. A., V. M. Petrov, Yu.V. Ivanov, V. A. Bondarenko, V. V. Tzetlin, V. S. Makhmutov, Ts.P. Dachev, and J.V. Semkova. Solar particle events observed on MIR station, *Radiation Measurements*, 1999, 30, 317–325. DOI: 10.1016/S1350-4487(99)00058-X
14. Semkova, J., Ts. Dachev, R. Koleva, N. Bankov, S. Maltchev, V. Benghin, V. Shurshakov, and V. Petrov. Observation of radiation environment in the International Space Station in 2012–March 2013 by Liulin-5 particle telescope, *J. Space Weather Space Clim.* 2014, 4, A32. DOI: 10.1051/swsc/2014029

15. Dachev, Ts.P., B. T. Tomov, Yu. N. Matviichuk, Pl. G. Dimitrov, N.G. Bankov. High dose rates obtained outside ISS in June 2015 during SEP event, *Life Sciences in Space Research*, 2016, 9, 84–92. DOI: 10.1016/j.lssr.2016.03.004
16. Reitz, G., R. Beaujean, E. Benton, S. Burmeister, Ts. Dachev, S. Deme, M. Luszik-Bhadra, and P. Olko. Space radiation measurements on-board ISS—the DOSMAP experiment. *Radiat. Prot. Dosimetry*. 2005, 116, 374–379. DOI: 10.1093/rpd/nci262
17. Narici, L., M. Casolino, L. Di Fino, M. Larosa, P. Picozza, and V. Zaconté. Radiation survey in the International Space Station. *J. of Space Weather and Space Climate*. 2015, 5:A37, 14 p. DOI: 10.1051/swsc/2015037
18. Dachev, Ts.P., J.V. Semkova, B.T. Tomov, Yu.N. Matviichuk, Pl.G. S. Maltchev, R. Koleva, Pl., Dimitrov, N.G. Bankov, V.V., Shurshakov, V.V., Benghin, E.N., Yarmanova, O.A. Ivanova, D.-P. Häder, M.T. Schuster, G. Reitz, G. Horneck, Y. Uchihori, H. Kitamura, O. Ploc, J. Kubancak, and I. Nikolaev. Overview of the Liulin type instruments for space radiation measurement and their scientific results, *Life Sci. in Space Res.*, 2015, 4, 92–114. DOI: 10.1016/j.lssr.2015.01.005
19. Dachev, Ts.P. Characterization of near Earth radiation environment by Liulin type instruments. *Adv. Space Res.* 2009, 44, 1441–49. DOI: 10.1016/j.asr.2009.08.007
- 19a. Spurný, F., & Dachev, T. Long-term monitoring of the onboard aircraft exposure level with a Si-diode based spectrometer. *Advances in Space Research*, 2003, 32(1), 53–58. DOI: 10.1016/S0273-1177(03)90370-X
20. Dachev, Ts., B. Tomov, Yu. Matviichuk, Pl. Dimitrov, J. Lemaire, Gh. Gregoire, M. Cyamukungu, H. Schmitz, K. Fujitaka, Y. Uchihori, H. Kitamura, G. Reitz, R. Beaujean, V. Petrov, V. Shurshakov, V. Benghin, & F. Spurny. Calibration Results Obtained With Liulin-4 Type Dosimeters. *Adv. Space Res.* 2002, 30(4), 917–925. DOI: 10.1016/S0273-1177(02)00411-8
21. Spurny, F. Response of a Si-diode-based device to fast neutrons, *Radiation Measurements*, 2005, 39, 219–223. DOI: 10.1016/j.radmeas.2004.05.006
22. Ploc, O., F. Spurny, and Ts.P. Dachev. Use of Energy Depositing Spectrometer for Individual Monitoring of Aircrew, *Radiat. Prot. Dosimetry*, 2011, 144(1–4), 611–614. DOI: 10.1093/rpd/ncq505
23. Green, A.R., L.G.I. Bennett, B.J. Lewis, F. Kitching, and M.J. McCall. Desormeaux, M., Butler, A., An empirical approach to the measurement of the cosmic radiation field at jet aircraft altitudes, *Adv. in Space Res.*, 2005, 36, 1618–26.
24. Spurny, F., O. Ploc, and I. Jadrníčková. Spectrometry of linear energy transfer and dosimetry measurements onboard spacecrafts and aircrafts. *Phys. Part. Nuclei Lett.*, 2009, 6, 70–77. DOI: 10.1134/S1547477109010117
25. Zhang, L., R. Mao, and R. Zhu. Fast neutron induced nuclear counter effect in Hamamatsu silicon PIN diodes and APDs, *IEEE Transactions on Nuclear Science*, 2011, 58(3), 1249–56. DOI: 10.1109/TNS.2011.2132144
26. Heffner, J. Nuclear radiation and safety in space. M, Atomizdat, 115 p., 1971. (In Russian).
27. Ghiassi-nejad, M., S.M.J. Mortazavi, J.R. Cameron, A. Niroomand-rad, and P.A. Karam. Very High Background Radiation Areas of Ramsar. 82. Preliminary Biological Studies. *Health Physics, Iran*, 2002, 87–93. URL: <http://www.probeinternational.org/Ramsar.pdf>.

ОПИСАНИЕ НА СИСТЕМАТА "ЛЮЛИН-МКС-2" ЗА ДОЗИМЕТРИЧЕН КОНТРОЛ НА КОСМОНАВТИТЕ В РАДИАЦИОННАТА СРЕДА НА МКС

*Цв. Дачев, Б. Томов, Ю. Матвийчук, Пл. Димитров,
В. Шуриаков, В. Бенгин, Е. Ярманова, О. Иванова, И. Николаев*

Резюме

По договор между Института за космически изследвания към БАН, Института за био-медицински проблеми на РАН и Ракетно-космическа корпорация „Енергия“ е разработен инженерен модел на новата система за персонален дозиметричен контрол на руските космонавти в и извън Международната космическа станция (МКС) – „Люлин-МКС-2“. Очаква се новата система да замени системата „Люлин-МКС-1“ и да се фокусира върху активен мониторинг, с разрешение от 10 s на динамиката на мощността на дозата от галактически космически лъчи (ГКЛ), протони от вътрешния и енергийни електрони от външния радиационни пояси, и слънчеви енергийни частици (СЕЧ) в модулите на МКС и по време на активности извън станцията (АИС) на руски и международни космонавти. Значимостта на измерването на дозата по време на АИС е оценена при анализа на големи и бързи колебания в пространствено-времеви разпределения на дозите, получени едновременно на две различни места извън МКС. Инженерният модел на системата „Люлин-МКС-2“ се състои от 2 преносими дозиметри (ПД) и интерфейс блок (ИБ) с вътрешен дозиметър. ПД е с размери 66×56×26 mm и е продължение на традиционните дозиметри от типа „Люлин“ с един 1 PIN диод. Анализът на спектрите от дозиметрите ще се извършва съгласно идеите за интелигентен личен дозиметър на екипажа и новия опит, получен по време на анализа на данните от инструмента R3DR2 извън МКС в периода октомври 2014–януари 2016 г. Призматичната литиево-йонна акумулаторна батерия на фирмата SAFT, одобрена за използване в космическото пространство се използва в ПД и позволява повече от 7 дни самостоятелна работа с разрешение от 10 s. По време на АИС, когато ПД се намира в джоба на скафандъра на космонавта, за да се поддържа температурата на PIN-диода не по-малка от -20°C в ПД се използват термостат и управляем нагревател. ПД може да работи независимо от ИБ посредством USB интерфейс и специален софтуер, с който и да е друг компютър. Интерфейсният блок се управлява от таблетен персонален компютър (ПК) на фирмата Getac от типа T800. Той е изпълнен в съответствие с изискванията и процедурите на стандарта MIL-STD-810G и е под ОС Windows-8. ПК управлява системата чрез 8-портов USB хъб, който свързва ПК с дозиметрите, CAN-интерфейса и външната флаш памет. Данните, получени с вътрешния дозиметър, за последната орбита (~90 минути) се визуализират непрекъснато на екрана на компютъра и ще бъдат използвани от космонавтите и наземния радиационен контрол за бърза оценка на риска за здравето на космонавтите по време на слънчеви протонни събития.

DYNAMICS OF REGULAR AND INCIDENTAL EVENTS ACCORDING TO THE MAGNETOMETRIC COMPLEX: MATERIALS OF THE "SCHUMAN" PROJECT

Yuriy Kuksa¹, Igor Shibaev², Dimitar Teodosiev³, Jaroslav Vojta⁴

¹*GEMRC IPE-RAS, Troitsk, Russia*

²*IZMIRAN, Troitsk, Russia*

³*SRTI-BAS, Sofia, Bulgaria*

⁴*UFA-CAS, Praha, Czech Republic*

e-mail: ishib@izmiran.ru

Abstract

In present article the review of results of the analysis of data of the monitoring, which is carried out within the "Schuman" project, is presented. The experimental part of the "Schuman" project is based on two hardware complexes. The first complex - the magnetometric station, registers three magnetic components, two electric, and amplitude envelopes of the acoustic channel. The quantization time of all channels is 0.5 s. The second complex including two induction magnetic field sensors is designed for registration in the Schuman range. The presented work is based on the data of the first complex working at IZMIRAN (Troitsk, Russia). The presented work shows possibilities and quality of the data from the magnetometric complex.

Introduction

Currently within the "Schuman" Project IZMIRAN has been conducting routine observations of geomagnetic variations in the frequency band up to 2 Hz [1]. The current investigations are supported by the magnetometric complex, which is based on a three-component unit of quartz magnetic field sensors. The complex also comprises 2 electric lines terminated with unpolarized electrodes. The electric lines are connected to the measuring unit via channels with conductive decoupling. In addition to electric channels a seismic pickup (via the seismic envelope detection and extraction unit) and a temperature sensor of the magnetic field sensor module are connected. The dynamic range across all channels is 22 discharges with a sampling time of 0.5 s.

The complex capabilities and quality of the data obtained are shown by the examples of recording both episodic events (solar flares of a different class, passing thunderstorm clouds) and routine observations (demonstration of the effect of daylight duration and the Moon on the dynamics of diurnal components in the analysis of extended arrays).

The temporal dynamics of daily values of the geomagnetic components with indications of a human pulse and arterial blood pressure was also correlated, which demonstrates the feasibility of using the monitoring data in the applied research.

Response to incidental events

A typical example the episodic event is a solar flare. The flare-generated additional ionospheric ionization results in the current alteration and perturbation of B-components up to $1\div 10$ nT during strong flares. Therefore, for a number of X-class flares a direct correlation of the observed perturbations of B_{x,y,z}-components and a X-ray flux burst, characterizing the flare, is possible. Such correlation of two events is demonstrated in Fig. 1, where moment X-ray flux data (in arbitrary units) in the ranges $0.5\div 4.0$ Å and $1.0\div 8.0$ Å of GOES series satellites [2] are compared with variations of the magnetic components in nT according to IZMIRAN data (“Schuman” project). Along the OX axis the time is given in minutes, T₀ is the beginning of the time axis, flare maximum – T_m.

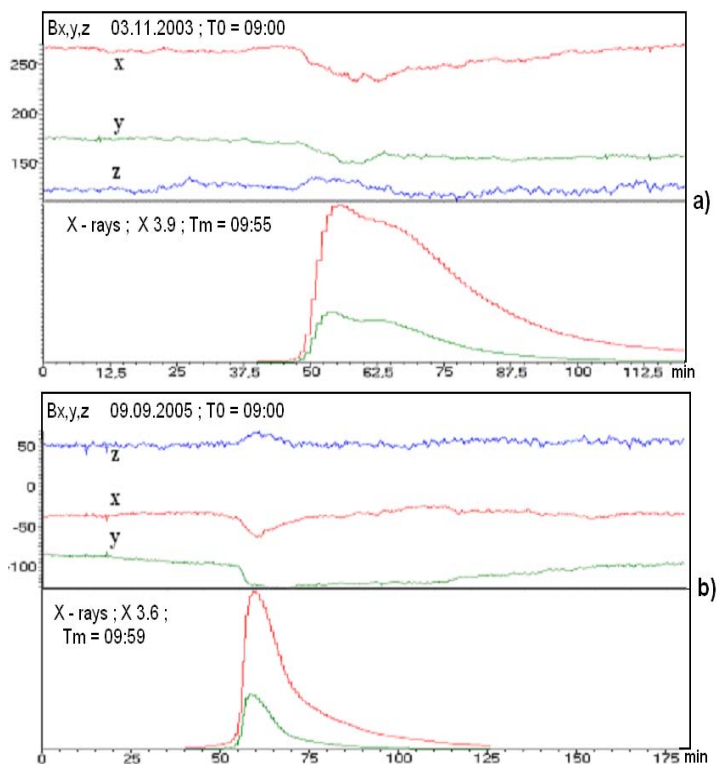


Fig. 1. Direct response to solar flares, X 3.9 – (a) and X 3.6 – (b)

Naturally, in addition to a flash class, the response manifestation accuracy depends on the season and local time. A different degree of the noise level is demonstrated in Fig. 2, where Almaty (“Intermagnet” project) [3] and IZMIRAN data is correlated for a strong X 6.9 class flare. In some cases, the M-class flash response can be also identified. The temporal dynamics of correlation relationships between the magnetic variation components (Fig.3, the lower Figure) clearly identified an M 6.9 class flare moment (Fig. 3, middle Figure). In the temporal dynamics of B_x, y, z -components no response is visible on the background of significant variations (Fig. 3, top Figure).

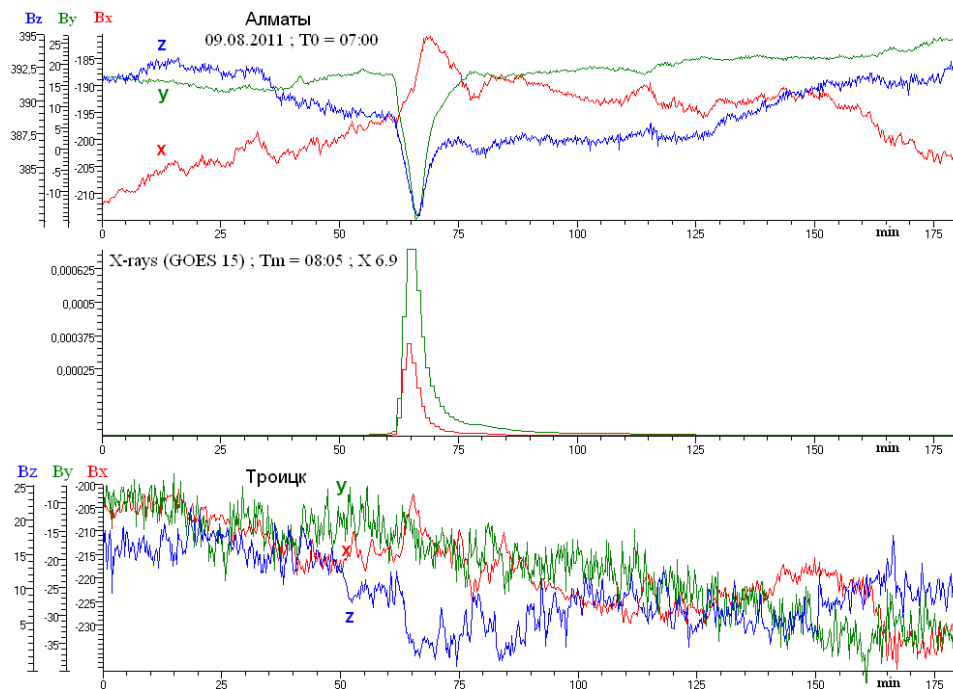


Fig. 2. Comparison of responses to solar flare according to Almaty and IZMIRAN

The example of recording the M 1.9 class seasonal flare in the morning with an aftereffect is provided in Fig. 4. The central part of the Figure highlights a rectangular area with B-component fluctuations and adjacent to the flare. It is quite possible that the observed oscillations are induced by the flash, their period is 3.9 minutes.

Another example of the episodic event is a thunderstorm. Passing through the storm area above the observation point is depicted in Fig. 5. Using E_x, y -components (in arbitrary units) moments associated with the polarization caused by storm clouds are clearly distinguished. Bursts P1 (P2) on the magnetic

component are characterized by the current alteration in front of (behind) the moving area of the induced charge. The burst size is comparable with the response of strong solar flares.

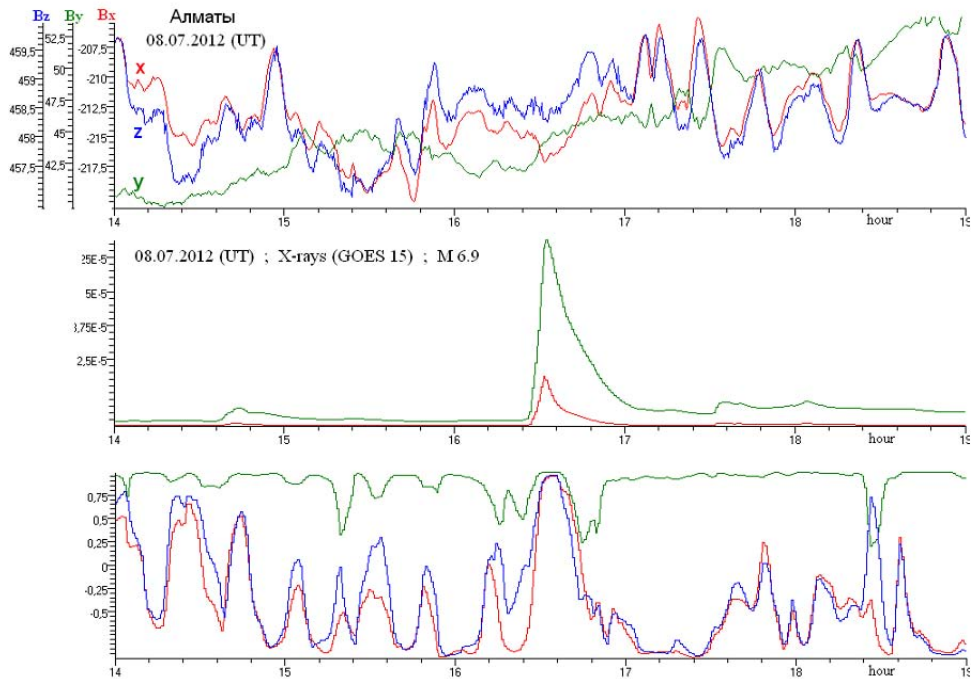


Fig. 3. Identification of a response to solar flare (class M 6.9) according to Almaty

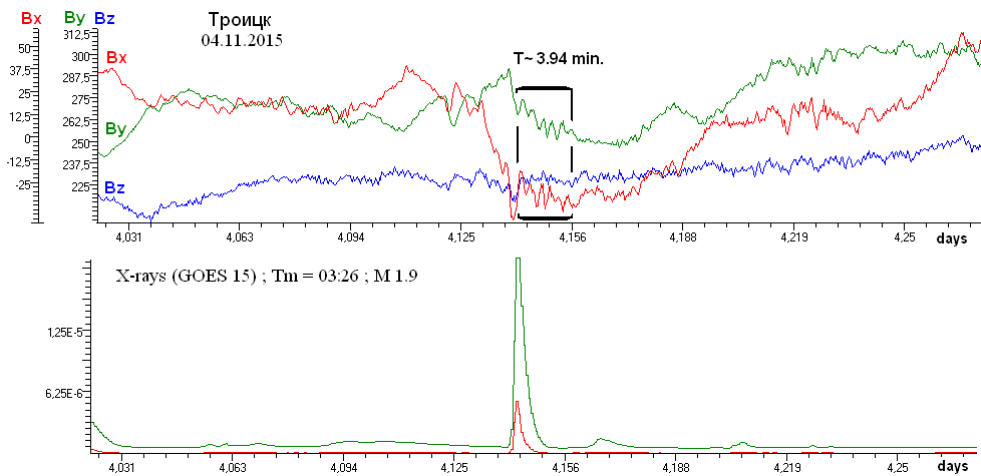


Fig. 4. Seasonal solar flare in the morning according to IZMIRAN (class M 1.9)

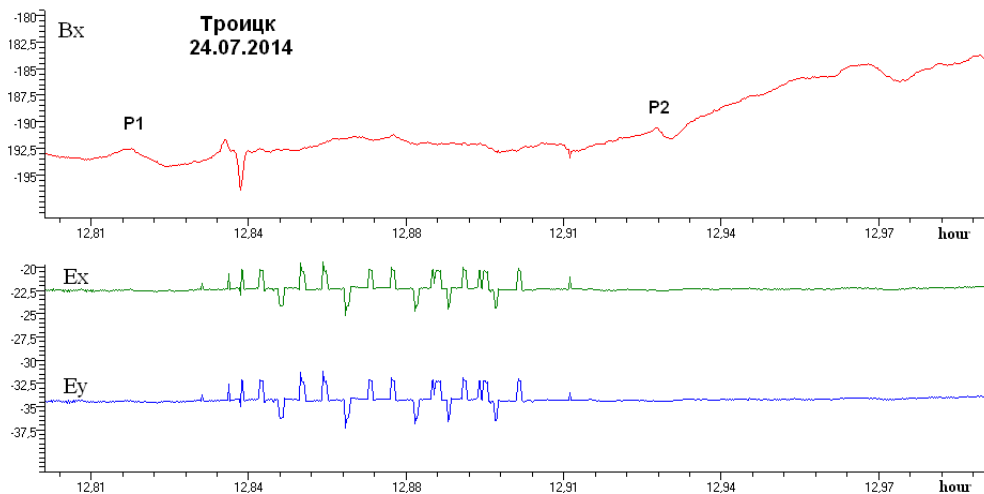


Fig. 5. Passing of a storm over the point of supervision

Assessment of characteristics of the regular events

Episodic events random in character occur against the background fairly regular processes associated with long observation intervals. Therefore, the assessment of baseline states of measured characteristics and their dynamics in the timeframes of different range is of great importance. In Fig. 6 is provided an overview of typical data recorded by the complex for 54 days (from March 6 to April 28, 2003). A detail of the envelope of the acoustic channel So is given in the right lower part of the Figure. A “day off” effect is visible; when on weekends and public holidays the noise level decreases (March 8÷10 was the weekend). In the spectral analysis of variations of the geomagnetic field components oscillation frequencies of the thermal atmospheric tidal waves appear. A complete set of periods contains 24, 12, 8 hours, and other harmonics are distinguished. The application of Hilbert transformation [4] makes it possible to obtain a time dependence of the amplitude of the selected harmonics. The envelopes (amplitudes) of the daily and twenty-minute harmonics for Bx-components are depicted in Fig. 7. The growing trend of the daily harmonic amplitude (Fig. 7, top Figure) reflects the increase of the light part of a day. The effect of the Moon's phase thereon is distinguished. The net effect of the gravitational forces of the Sun and the Moon occurs near the new moon, when the maximum effect should be expected. The lower part of the Figure shows the component amplitude with a period of ~20 minutes. Its relationship with selected moments of the daily harmonics is clearly seen. It should be noted that on March 17 and April 26 solar flares of X 1.5 and M 7.0 classes (in the morning and in the evening) occurred, that could increase the emissions on day 17 and day 57.

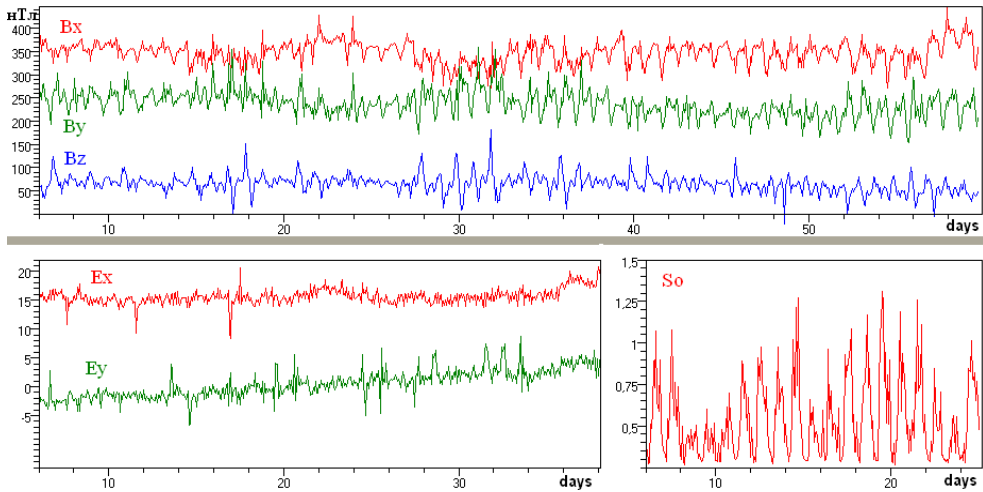


Fig. 6. The overview of data in 54 days

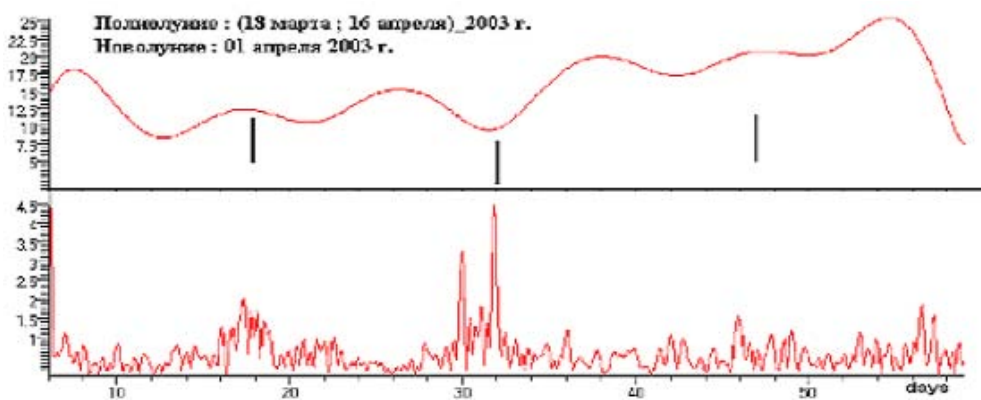


Fig. 7. The envelopes of the daily and twenty-minute harmonics for Bx-components

Connection of arterial pressure and pulse at changes of geomagnetic activity

Data on daily monitoring of systolic blood pressure (SBP), diastolic blood pressure (DBP) and heartrate (HR) for 2000 was applied. The measurements were performed by a patient in the morning and in the evening within the blood pressure self-monitoring program implemented under the care of a physician [5]. To describe a degree of the organism coordination ability, the time dependence of the linear correlation of medical parameters: $K1(t) = \text{Corr}(\text{HR}\&\text{SBP}; t)$ – dynamics of correlation coefficient between the heart rate and SBP; $K2(t) = \text{Corr}(\text{HR}\&\text{DBP}; t)$ correlations between the heart rate and diastolic blood pressure; $K3(t)$ – correlations between SBP and DBP were used. Their behavior was compared with

the dynamics of daily values of the geomagnetic components. What was the minute data of H, D, Z variations of the magnetic field for 2000 used for, and the envelope of their daily harmonics was selected.

The analysis result for the morning correlation relationships is presented in Fig. 8. It can be seen that the maximum values of daily amplitudes of B-components (in the vicinity of 100 and 200 days) and their fronts are superimposed on the periods when the morning readings of the heart rate and blood pressure changed out most clearly.

We have to add that in the spectra of annual B-component arrays a lunar (27.3 d.) and triple lunar periods are identified. The high-frequency part comprises a period of about 9 and 18 minutes. A similar phenomenon was mentioned above in the analysis of other time array intervals.

Conclusions

The review of the assessment results for the magnetometric complex data was demonstrated. The possibility of correlating and analyzing both minute and annual intervals was shown. The manifestation of responses to various processes of about 5÷20 minutes should be noted. Close time scales in various situations are presented in papers [6, 7].

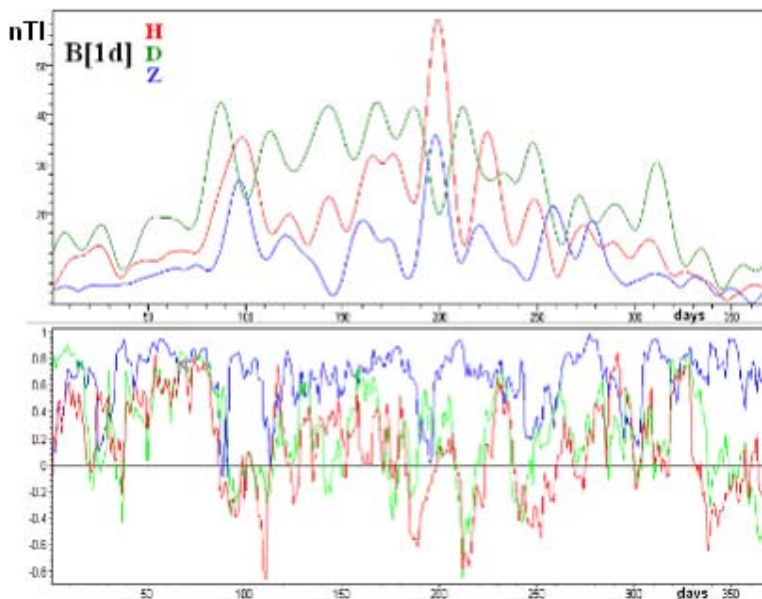


Fig. 8. The envelopes of the daily harmonics for B-components (top Figure) and correlation relations of pulse with arterial pressure (bottom). X axis - days of year; Red dashed line - $K1(t)$; Green dashed line - $K2(t)$; Blue dashed line - $K3(t)$.

References

1. Ишков, В. Н., Ю. И. Кукса, Д. Теодосиев, И. Г. Шибает. Непосредственный отклик на солнечные вспышки по данным магнитометрического комплекса: проект “Шуман”. В: Труды “Всероссийской ежегодной конференции по физике Солнца: Солнечная и солнечно-земная физика 2010”, Пулковско, Санкт Петербург, 3–9 октября 2010 г., с. 179–182.
2. http://satdat.ngdc.noaa.gov/sem/goes/data/new_avg/
3. www.intermagnet.org
4. Bendant, J., A. Pirsol. Random Data. Analysis and Measurement Procedures, John Wiley & Sons, Inc., NY, 1986.
5. Isajkina, O., Yu. Kuksa, I. Shibaev. Estimation of stability of arterial pressure and pulse at changes of geomagnetic data and atmospheric pressure. In: Proceedings of 9th Scientific Conference with International Participation "Space, Ecology, Safety" SES'2013, Sofia, Bulgaria, 2014, 36–42.
6. Шаповалов, С. Н., О. А. Трошичев, А. М. Безгрешнов. “Колебания Солнца” в диапазоне 297–330 нм по данным наземных спектральных наблюдений на ст. Новолазаревкая (Антарктида). В: Тезисы одиннадцатой ежегодной конференции „Физика плазмы в солнечной системе“, ИКИ-РАН, Москва, 15–19 февраля 2015г., с. 198.
7. Куколева, А. А., А. А. Криволуцкий, Т. Ю. Вьюшкова. Изменения в озоносфере Земли в период глубокого минимума солнечной активности в период 2003-2010 г.г. (трехмерное фотохимическое моделирование). В: Тезисы одиннадцатой ежегодной конференции “Физика плазмы в солнечной системе”, ИКИ-РАН, Москва, 15–19 февраля 2015 г., с. 194.

ДИНАМИКА НА РЕГУЛЯРНИ И СЛУЧАЙНИ СЪБИТИЯ ПО ДАННИ ОТ МАГНИТОМЕТРИЧЕСКИЯ КОМПЛЕКС: МАТЕРИАЛИ ОТ ПРОЕКТ “ШУМАН”

Ю. Кукса, И. Шибает, Д. Теодосиев, Я. Войта

Резюме

В работата е представен обзор на резултатите от анализа на данни от измерване на УНЧ вълни, осъществяван в рамките на проект “Шуман” [1]. Магнитометрическият комплекс регистрира три магнитни компоненти, две електрически и обвиваща на акустичния канал. Динамическият диапазон по всичките канали е 22 разряден с период на квантуване 0.5 сек. В настоящия момент в ИЗМИРАН (Троицк, Русия) се провеждат регулярни наблюдения на геомагнитните вариации в честотния диапазон до 2 Hz. В работата се демонстрират възможностите и качеството на получаваните данни от магнитометрическият комплекс.

APPLICATION OF SPACE TECHNOLOGIES FOR STUDIES AND MONITORING OF SEISMOGENIC ZONES

Dimitar Dimitrov

*National Institute of Geophysics, Geodesy and Geography – Bulgarian Academy
of Sciences (NIGGG-BAS)
e-mail: clgdimi@bas.bg*

Abstract

In the present article are presented the results of studies carried out by the author, or by teams under his supervision and participation, in different seismogenic zones in Bulgaria and abroad. The submitted cases of the application of space technologies Global Navigation Satellite System (GNSS) and Interferometry Synthetic Aperture Radar (InSAR) for investigation and monitoring of seismogenic zones manifest the significance and the advantages of these methods in determination of the regularities in the development of the tectonic processes of accumulation and release of tensions in the seismogenic zones, related to the assessment of the seismic hazard and medium-term forecast of strong earthquakes.

1. Introduction

The Global Earth Observation System of Systems (GEOSS) and Copernicus (formerly the Global Monitoring for Environment and Security – GMES) programs have as a priority the preservation of the environment and the sustainable development of the society, development of instruments for assessment, as well as methods for monitoring and prognosis.

The seismogenic zones are the regions genetically connected to historical and instrumental seismicity, which have potential seismic hazard of strong earthquakes and are identified by seismological, geophysical, and geological data. The Republic of Bulgaria is situated in an active seismogenic zone. This fact results in formulation of one of the main objectives for Bulgarian geophysical science, i.e. to study the processes occurring in these zones which lead to strong earthquakes and to undertake appropriate measures for effective counteraction. This problem is characterized with special topical degree as on a national as on a planetary scale and puts it in the category of priority research trends in the field of Earth sciences.

The application of space technologies Global Navigation Satellite System (GNSS) and Interferometry Synthetic Aperture Radar (InSAR) allow studying the seismogenic zones and the physical processes causing strong earthquakes.

The permanent and periodic high precision measurement with GNSS and the application of the InSAR are the most effective space technics for monitoring and study of the seismogenic zones.

Below are represented the results of the studies carried out during the last 20 years by the author himself, teams under his supervision, or with his participation in different seismogenic zones in Bulgaria and all over the world.

2. Monitoring of the seismogenic zone in the region of Sofia city

The region in south of Sofia city is revealed in structure-geomorphologic, tectonic and seismic approach seismogenic zone where could be expected strong earthquakes [1]. This zone is connected to the so-called *Vitosha fault* dividing *Vitosha* morphoblock from the absorbed under neogenic sediments complex broke up Sofia graben. The surface manifestations of *Vitosha* and *Lozen* faults are presented on the space image by appointed with InSAR method relatively vertical deformations and the network for GNSS monitoring (Fig.1).

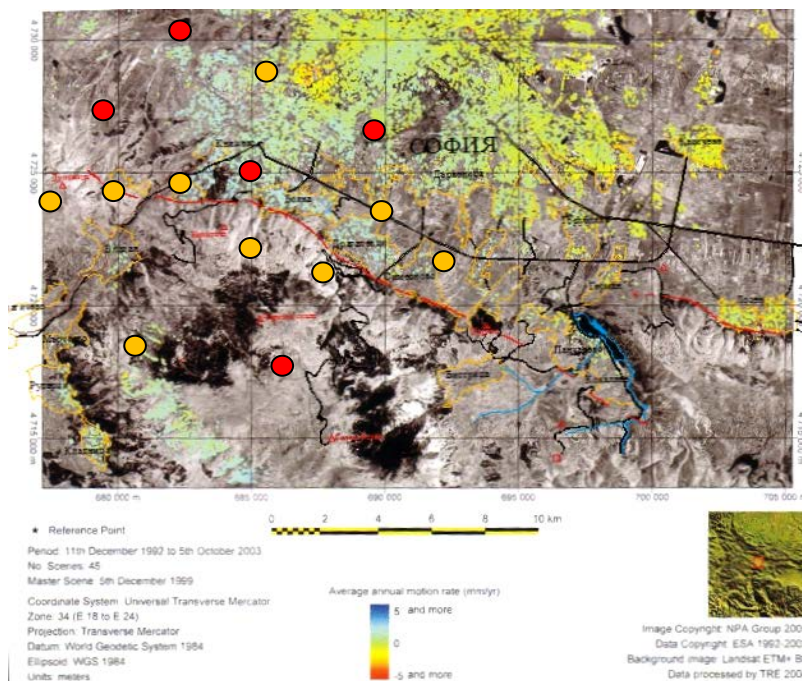


Fig. 1. Network for GNSS monitoring of the Vitosha fault on the space image and the result of the InSAR study of the zone. The permanent GNSS stations are presented with red and the periodic measurements with orange circles.

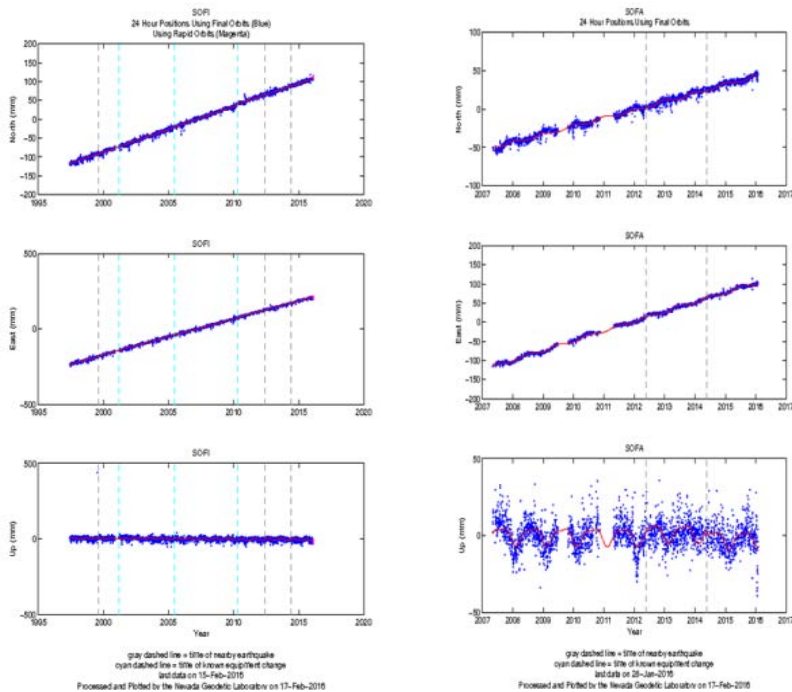


Fig. 2. Components of the absolute velocities from the permanent stations of SOFI and SOFA, on the both sides of the Vitosha fault

The obtained from the monitoring identical velocities of displacements of the permanent and periodic GPS measurement stations (Fig. 2) of the order of $1\div 2$ mm/yr do not testify for accumulating of considerable tectonic tensions on Vitosha fault. The data from the permanent and periodic re-measurement GPS stations in the regions provide a high-precision monitoring of the movements in this seismogenic zone in connection with the study of tectonic tensions and seismic hazard [2].

3. Studies and monitoring of the seismogenic zone Chirpan – Plovdiv

The application of the space technology GNSS for assessment of the velocities of shifting of geodetic benchmarks in the region allow to study the zone and to determine the geodetic parameters of the main faults, activated in 1928 [3] (Fig. 3). The monitoring of the zone with periodic GNSS measurements (Fig. 4) provides an assessment of the tectonic tensions. Along with paleoseismic studies allows determining the seismic cycle of strong earthquakes in the region [4].

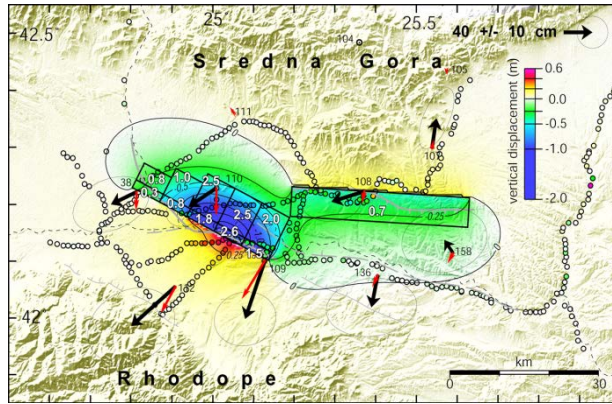


Fig. 3. Main faults, activated during the earthquakes on 14 and 18 April 1928, obtained from modeling of the co-seismic displacements determined by data from GNSS measurements (black arrows)

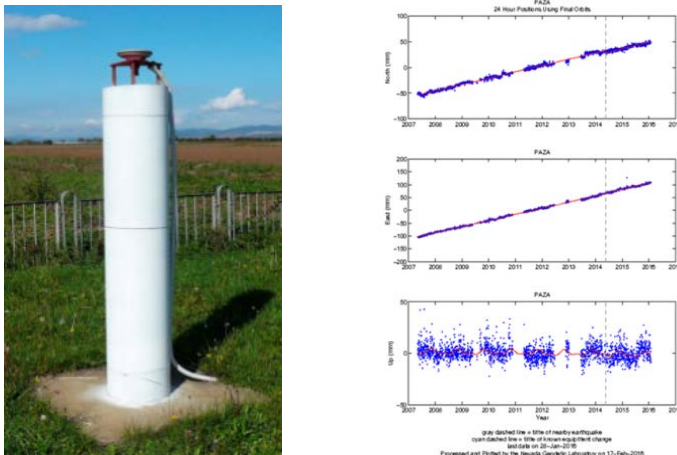


Fig. 4. On the left is a photo of permanent GNSS station in the city of Pazardzhik, and on the right is the components of its time series

4. Studies and monitoring of the seismic zone of Southwestern Bulgaria

The region of Southwestern Bulgaria is known with one of the strongest earthquakes which have struck Europe with a magnitude (M) 7.3 and 7.8 on 4 April 1904 [1]. The long standing monitoring of the zone with permanent GNSS stations and periodic measurements of the local geodynamic network around *Krupnik* fault allow to assess the regional tectonic movements and local tensions around *Krupnik*

fault (Fig. 5). According to the data obtained and together with the results from the paleoseismologic studies was determined the seismic cycle of the *Krupnik* fault [5].

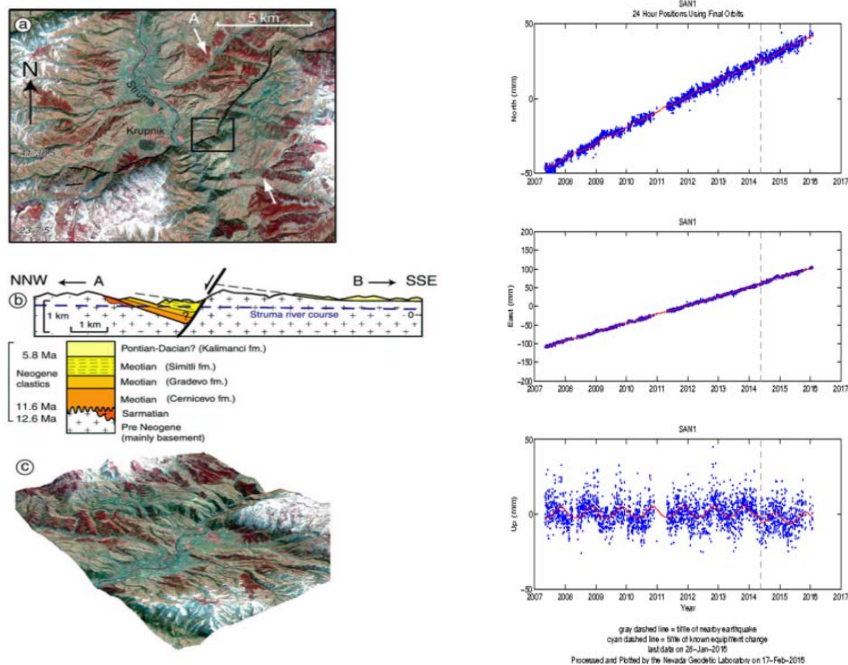


Fig. 5. The Krupnik fault mapping on a space image, geologic cross section, and components of absolute velocities of the permanent GNSS stations in the city of Sandanski

5. Studies of seismogenic zones in Central Greece

The *Corinth* Bay in Central Greece is one of the most seismologically active internal continental structures in Europe [6]. This asymmetric graben is surrounded from active faults causing many catastrophic earthquakes (Aigion, 1861 r. $M = 7.0$; Corinth, 1981 r. $M = 6.7$) [7]. Since 1991 in this seismogenic zone is carried out a monitoring of the surface deformations with GNSS network from 22 permanent and 240 periodic pre-measurement stations [8]. It was established a stretching of the bay with medium velocity of $14 \div 15$ mm/yr [8].

5.1. For the study of the earthquake on 15.06.1995 has been used data from the space methods GNSS and InSAR (Fig. 6). On figure 6 are presented coseismic displacements from the earthquake of 1995 of 24 benchmarks, assessed by GNSS measurements, as well as coseismic deformations from InSAR study. The modeling of the obtained coseismic displacements allows accessing the geometric seismotectonic parameters of the main faults of the main shock [2].

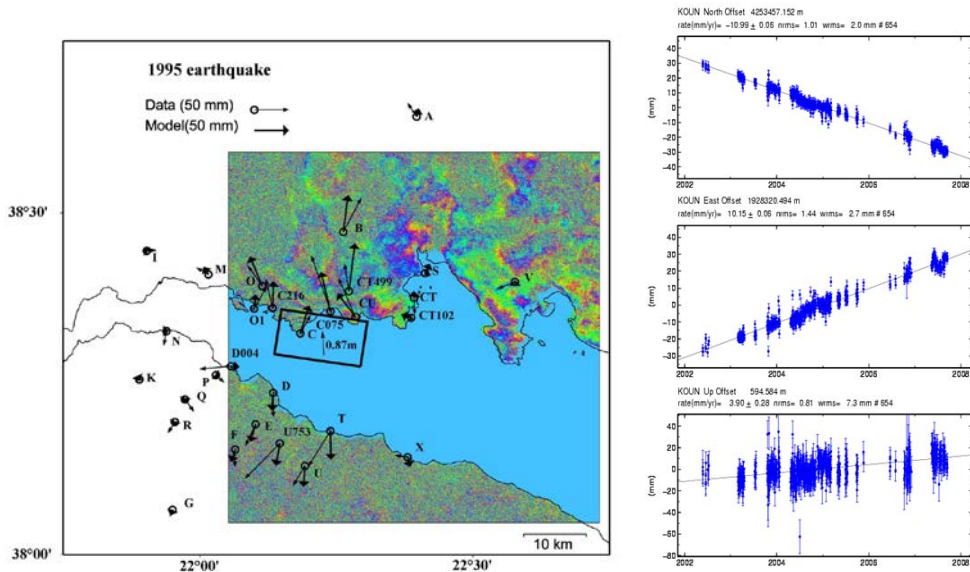


Fig. 6. The region of the earthquake on 15.06.1995 with determined by GNSS and InSAR methods of coseismic deformations. The assessed and modelled displacements are presented respectively by thin and thick arrows. On the right is presented a comparison between permanent stations on the two coasts of Corinth Bay. The space vectors between stations on the two coasts of the bay has been struck.

5.2. In the study of the earthquake on 26.07.1996 in Konitsa $M = 5.3$ in Northern Greece was confirmed the possibilities of the method InSAR for the study of the physical mechanisms of medium-strong earthquakes with (Fig. 7).

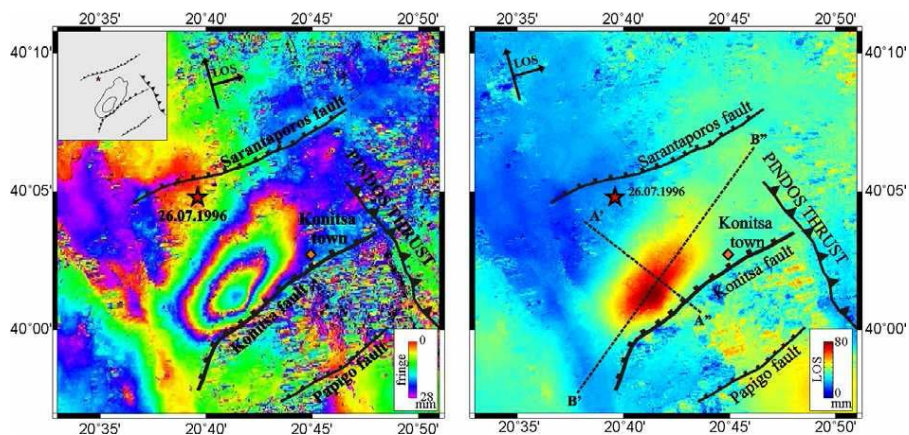


Fig. 7. Seismogenic zone of town of Konitsa and the faults activated with the assessed coseismic deformations with InSAR of the earthquake of 1996

5.3. The study of the earthquake of 2003 in Lefkada M = 6.3 with InSAR and modeling of coseismic deformations (Fig. 8) shows the possibilities of this method for assessment of the place and the seismotectonic parameters of the activated sea faults [9].

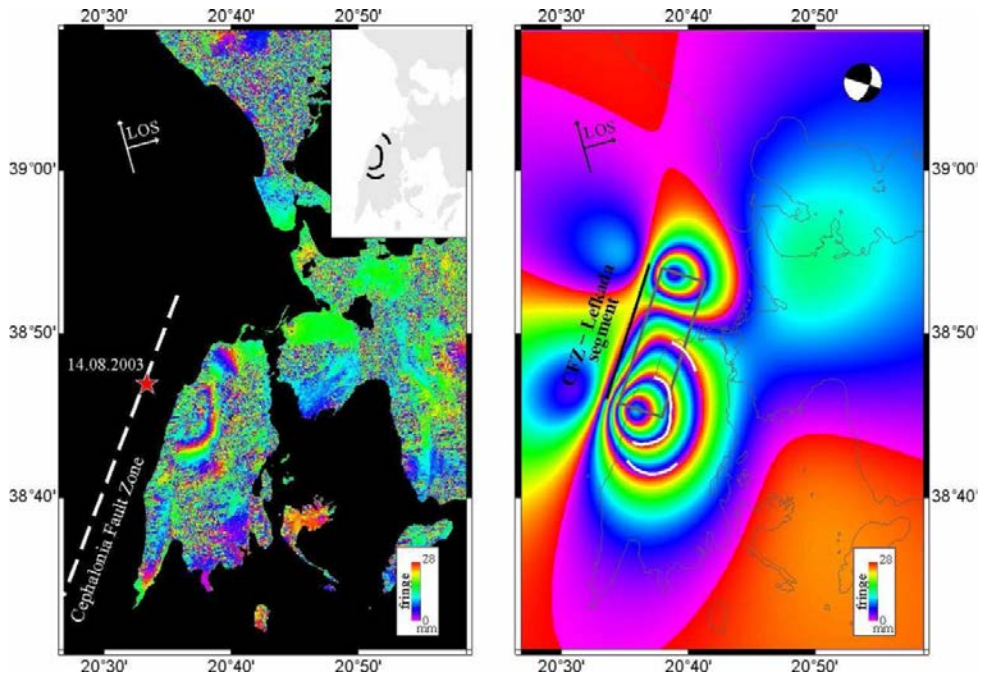


Fig. 8. On the left – Isle Lefkada with the assessed by the method InSAR coseismic deformations and the fault activated during the shock of 2003. On the right – the model of coseismic deformations.

6. Study of the zone of the earthquake of 1835 in Central Chile

The seashore line of Chile is one of the most seismogenic zones in the world. Here approximately at every ten years occur strong earthquakes with magnitude $M > 8$. The region is situated between 35° and 37° S and is known with its very strong earthquake in February 1835 [10] with $M = 8.5$ [11] (Fig. 9).

In this region was stabilized and assessed in 1996, 1999, and 2002, with a GNSS network of 41 points which allow considerable displacements of monitoring stations, reflection of the accumulation resulting from the subduction interseismic tensions.

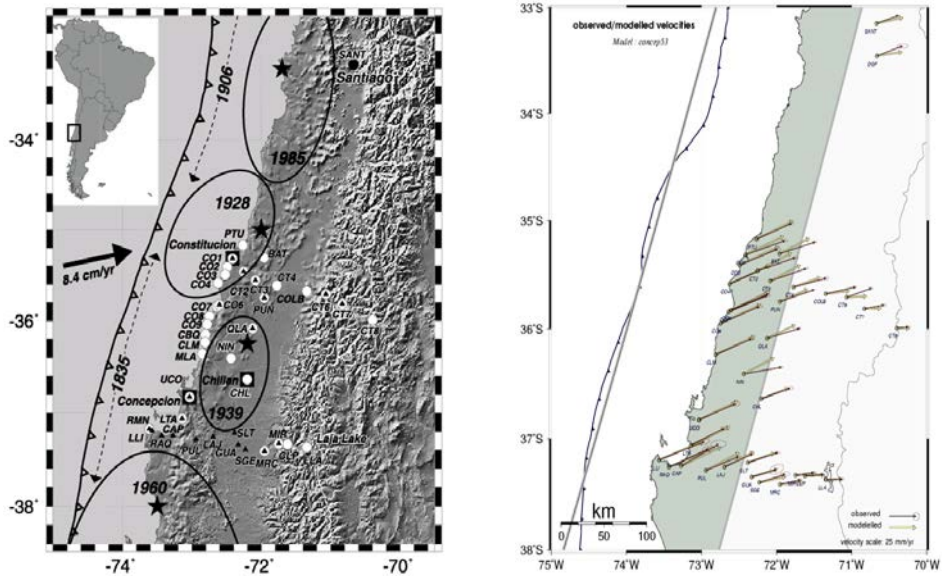


Fig. 9. On the left – Geodynamic GNSS network of 41 points in the seismogenic zone of Central Chile with the results of monitoring from 1996, 1999, and 2002. On the right (in grey) – the zone of collision of the Pacific Nazca Plate with this in South America, obtained from the modeling of interseismic displacements.

The analysis of the results from three cycles of measurements determines considerable interseismic movements with velocity from 34 to 45 mm/yr on coastline and from 10 to 20 mm/yr on the mountain range of Andes in comparison with the stable part of the South American continental Plate (Fig. 9). Namely the considerable difference between velocities of movement of the benchmarks stabilized on the coastline and those on the mighty mountain range of Andes is the reason for the accumulation of the seismogenic tensions in the area up to the contact zone. The data obtained allow assessing exactly the place and parameters of insertion: Azimuth $N 19^\circ$; gradient 16° ; sliding 67 mm/yr and depth of shock 55 km. The results show that the earthquakes in this zone are not simply a kind of subduction; and between the subduction zone and the mighty mountain range of Andes are accumulated tensions, increasing the danger of a new strong earthquake [12].

According to the parameters obtained has been calculated the accumulated tectonic tension in the region of the last strong earthquake in 1835 with $M = 8.5$, on the basis of which was made a prognosis for an expected strong earthquake in the zone with $M > 8.5$ [12]. The forecast of the occurring in the study zone earthquake in March 2010 with $M = 8.8$ was cited in [13] as “a good example and successful forecast of strong earthquakes on the basis of scientific data and methodology”.

6. Conclusion

The examples presented of the application of the space technologies GNSS and InSAR for study and monitoring of seismogenic zones show their importance and advantages in establishing of regularities in the development of slow and fast motions in the seismogenic zones, in revealing the developing tectonic processes and namely the accumulation and delivering of tectonic tensions, related to the assessment of seismic hazard and the forecasting of strong earthquakes.

References

1. Hristoskov, L. Seismology, 2007, 2nd ed. (in Bulgarian)
2. Dimitrov, D. St. Geodetic studies in the seismogenic zones. D.Sc. Thesis, 2009. (in Bulgarian)
3. Dimitrov, D. S., J. B. De Chabaliér, J.-C. Ruegg, R. Armijo, B. Meyer, and E. Botev, The 1928 Plovdiv sequence (Bulgaria): fault model constrained from geodetic data and surface breaks, *Geophys. J. Int.*, 2016. (in press)
4. Vanneste, K., A. Radulov, P. DeMartini., G. Nikolov, T. Petermans, K. Verbeeck, D. Pantosti, T. Camelbeeck, D. Dimitrov, and S. Shanov. Paleoseismologic investigation of the fault that ruptured in the April 14, 1928, Chirpan earthquake (M=6.8), Southern Bulgaria. *Journal of Geophysical Research*, 2006, 111, B01303.
5. Meyer, B., M. Sebrier, and D. Dimitrov. Rare destructive earthquakes in Europe: The 1904 Bulgaria event case, *Earth and Planetary Science Letters*, 2007, 253, 3–4, 485–496.
6. McKenzie, D. P. Active tectonics of the Mediterranean region, *Geophys. J. R. Ast. Soc.*, 1972, 30, 109–185.
7. Briole, P. et al. Active deformation of the Corinth Rift, Greece: results from repeated Global Positioning System survey between 1990 and 1995, *J. Geophys. Res.*, 2000, 105(B11), 25605–25625.
8. Pérouse, E. Cinématique et tectonique active de l'ouest de la Grèce dans le cadre géodynamique de la Méditerranée Centrale et Orientale, Thèse de doctorat de 3^{ème} cycle, Univ. Orsay-Paris Sud, 2013.
9. Ilieva, M., P. Briole, A. Ganas, D. Dimitrov, P. Elias, A. Mouratidis, and R. Charara. InSAR investigation and fault plane modelling of 14th of August 2003 Lefkada Island (Greece) earthquake, *Tectonophysics*, 2016. (in press)
10. Darwin, C. Geological observation on coral reefs, volcanic island and on South America, Londres, 1851, 768 p.
11. Lomnitz, C. The Peru earthquake of May 31, 1970: Some preliminary seismological results. *Bulletin of the Seismological Society of America*, 1971, 61(3), 535–542.
12. Ruegg, J. C., A. Rudloff, C. Vigny, R. Madariaga, J. B. de Chabaliér, J. Campos, E. Kausel, S. Barrientos and D. Dimitrov. Interseismic strain accumulation measured by GPS in the seismic gap between Constitución and Concepción in Chile, *Physics of the Earth and Planetary Interiors (PEPI)*, 2009, 180, 78–85.
13. Kanamori, H. Earthquake Hazard Mitigation and Real-Time Warnings of Tsunamis and Earthquakes. *Pure and Applied Geophysics*, 2015, 172, 2335–2341.

ПРИЛОЖЕНИЕ НА КОСМИЧЕСКИ ТЕХНОЛОГИИ ЗА ИЗСЛЕДВАНЕ И МОНИТОРИНГ НА СЕИЗМОГЕННИ ЗОНИ

Д. Димитров

Резюме

В настоящата статия са представени резултатите от изследвания, осъществени от автора или от колективи под негово ръководство или с негово участие, в различни сеизмогенни зони у нас и по света. Представените примери от приложението на космическите технологии GNSS (Global Navigation Satellite System) и InSAR (Interferometry Synthetic Aperture Radar) за изследване и мониторинг на сеизмогенни зони показват значението и предимствата на тези методи при установяване на закономерности в развитието на тектонските процеси на натрупване и освобождаване на напрежения в сеизмогенните зони, свързани с оценката на сеизмичният риск и средносрочното прогнозиране на силни земетресения.

A COMPARATIVE ANALYSIS BETWEEN MODIS LST LEVEL-3 PRODUCT AND IN-SITU TEMPERATURE DATA FOR ESTIMATION OF URBAN HEAT ISLAND OF SOFIA

Ivan Yanev¹, Lachezar Filchev²

¹*ESRI Bulgaria, Ltd., Sofia, Bulgaria*

²*Space Research and Technology Institute – Bulgarian Academy of Sciences
e-mail: ivan.yanevmail@gmail.com*

Abstract

In present study we use global eight-day MODIS Land Surface Temperature (LST) and Emissivity Level-3 satellite products (MOD11A2 and MYD11A2) with in-situ data from automatic weather stations (AWS) to analyze usability and reliability of satellite derived LST data for Urban Heat Island estimation for the city of Sofia, Bulgaria. In order to achieve the study aim the terrestrial measurements from eight AWS were compared to the extracted pixel values from the MODIS LST Level-3 products. The so formed time-series were averaged to align with MODIS LST Level-3 products and gap-filled using the established relationship between the satellite and terrestrial data. A very strong positive relationship ($R^2 \sim 0.97$ at 95% confidence interval) was found for the eight ground AWS which readings were analyzed on a diurnal and seasonal basis for the year of 2013. It is suggested that the pronounced diurnal and seasonal variations in the trends and correlation between satellite and in situ temperature data were primarily related to the different land-use/land-cover type of the mixed pixel of MODIS.

1. Introduction

Due to the greenhouse effect and global warming, thermal environment has received a great attention in the recent years which refers not only to the air temperatures, but also the Land Surface Temperatures (LST) [1, 2]. Human settlements and especially, large urban areas significantly modify the environment [3]. The most documented and unquestioned urban climatic effect is the urban influence on the surface temperature exemplified by the urban heat island (UHI) [4]. The urbanization process leads to two essential changes: change of materials covering the surface which influences the solar radiation absorption, and change of the shapes on the surface which influences the air flows [5].

Surface and atmospheric modifications due to urbanization generally lead to a modified thermal climate that is warmer than the surrounding non-urbanized areas – a phenomenon known as UHI [6]. An UHI is the name given to describe the characteristic warmth of both the atmosphere and surfaces in cities (urban

areas) compared to their (non-urbanized) surroundings [7]. The UHI may be atmospheric heat island when it refers to the relative warmth of the atmosphere or surface heat island – relative warmth of the surface temperature.

Urban areas are demonstrating surface roughness and high urban surface heterogeneity in both horizontal and vertical aspect which makes the analysis of UHI extremely difficult [8]. Many factors affect formation and dynamic of urban microclimate – surface type ratio [9–14], buildings density and height [15–17], buildings exposure and materials (especially roofs) [18], urban geometry [19–21], urban surface materials [22], percent and type of the area directly exposed to the sunlight [23–25], industrial activities [26–29], anthropogenic heat injected from the cooling systems and vehicles [30–32], population density etc. [33].

From the reviewed literature it can be concluded that for a successful analysis of the strongly varying 3D urban environment a big number of densely located stations is needed to collect temperature data. In situ data (in particular, permanent meteorological station data) offer high temporal resolution and long-term coverage but lacks spatial detail which makes them insufficient to monitor the spatial extent of the UHI. Mobile observations overcome this limitation to some extent, but do not provide synchronized view over a city, as well as high density measurement networks are costly [25, 34]. Thermal Infra-Red (TIR) imagery has the advantage of providing a time-synchronized dense grid of temperature data over a whole city [35].

Remote sensors acquire the surface temperature directly exposed to the Instantaneous Field Of View (IFOV) [36]. They measure the LST, which is defined as the skin temperature of the surface (grass, roofs, trees, roads etc.) exposed to the satellite sensor [25, 37]. The LST is a widely used parameter to analyze UHI. Obtaining LSTs over extensive terrains was impractical until the advent of satellite thermal sensor. However, acquiring satellite images with high temporal, spatial, and spectral resolutions remains a problem [38].

Although the satellite-derived temperatures and UHIs are a well-documented issue, and a growing number of publications are issued every year on the topic, the low resolution thermal remote sensing products for UHI estimation has not been validated in Bulgaria until present. The city of Sofia has been studied only recently from [3] who used MODIS to analyze surface temperature of urban areas in Central European cities including Sofia. Non-satellite estimates of the Sofia's UHI have been carried out by micro climatologists and urban climatologists on the basis of comparing meteorological data from the city-centre and the vicinity of Sofia. However, no real estimate of the applicability of MODIS LST for the city of Sofia is known to be published elsewhere.

The study aim is to assess the applicability of MODIS LST Level-3 satellite products for estimating UHI of Sofia, Bulgaria. For this purpose the following objectives have been defined: 1) to compare single MODIS LST Level-3 product with Automatic Weather Stations (AWS) near-surface temperatures;

2) to correlate of MODIS LST Level-3 product with AWS near surface temperatures; and 3) to assess the land cover influence on the correlation.

2. Study area

The area of interest is the city of Sofia – the capital and the biggest city of Bulgaria, and the 16th largest city in the EU [39]. It is located in the West part of the country in the central part of the Sofia valley ($\lambda=23^{\circ}19'28.443''\text{E}$, $\varphi=42^{\circ}41'48.492''\text{N}$) which in turn extends from North-West to South-East between Balkan Mountains on the North and the mountains *Viskyar*, *Lyulin*, *Vitosha*, *Lozenska* on the South, the rivers *Slivnishka* and *Gaberska* on the West and to the East it borders with *Vakarel* Mountain. The entire character of the landscape defines the climate of Sofia. According to climate classification adopted in Bulgaria, Sofia falls into temperate continental climate subzone of European continental climate zone [40]. The city of Sofia is constantly growing in population. The official population estimate in 2015 is around 1.3 million people (2011 census) [41]. This is a prerequisite for the presence of more reliable and frequent meteorological data which make Sofia a suitable place for such an investigation.

3. Data description and processing

Satellite data

The eight-day MODIS global LST and Emissivity Level-3 satellite products (MOD11A2 and MYD11A2) for the whole year of 2013 were used in this study. Two MODIS instruments have been launched onboard TERRA (December 18, 1999) and AQUA (May 4, 2002) platforms as part of NASA's Earth Observing System (EOS) project [42]. The TIR observations for both day and night overpasses of MODIS-Terra at $\approx 10:30$ h (descending) and 22:30 h (ascending) and MODIS-Aqua at $\approx 13:30$ h (ascending) and 1:30 h (descending) local solar time are available in both products [43]. Therefore, four observations are available for each day from a combination of the two sensors increasing the quantity of the emissivity and temperature science data over the global land surface due to the increasing number of MODIS observations in clear sky condition. Other strengths of the MODIS instruments are global coverage, high geolocation accuracy, high radiometric and temporal resolution, and accurate calibration in the visible, near-infrared and TIR bands [44].

The eight-day MODIS LST product is the averaged (simple averaging method) LSTs of the MOD11A1 product over eight days. It is constructed through mapping the SDSs of all pixels in MOD11_L2 products onto grids and averaging the values in each grid. The MODIS LST Level 3, version 5 products are in Sinusoidal projection [8]. A tile contains grids in 1200 rows \times 1200 columns.

The exact grid size at 1 km spatial resolution is 0.928 km×0.928 km. As ϕ increases beyond $\pm 30^\circ$, the LST value at some grids in the MOD11A1 product may be the average value of LSTs retrieved from multiple MODIS observations in clear-sky conditions in day or night. The (MOD11_L2) LST Level 2 product is generated by the generalized split-window LST algorithm [45] and the emissivity in bands 31 and 32 are estimated by the classification-based emissivity method [46]. The LST retrieval in a MODIS swath is constrained to pixels that: 1) have nominal Level 1B radiance data, 2) are in clear-sky conditions at a 99% confidence defined in MOD35, 3) are on land or inland water [8]. According to MODIS land validation web-site MODIS MOD11 (Terra) and MYD11 (Aqua) Collection 5 (C5) has accuracy ≤ 1 K (0.5 K mainly) [47].

Meteorological data

We used daily temperature data for the same time period from automatic weather stations (AWS) available in Weather Underground. This is the first Internet weather service delivering meteorological information globally since 1993 [48]. According to the Weather Underground web-site, the stations are put to a strict quality control. The used raw data from eight AWS, which refer to the entire 2013 year, serve for our diurnal and seasonal dynamic investigation. The 2013 was chosen as it is the most recent year excluding 2014 that was too rainy, i.e. with more cloud cover which limit the availability of MODIS LST product. The AWSs are situated in an urban environment on roof tops or grass areas, Table 1. They collect data in five-minute intervals except AWS *Sofia Airport* which collects its data on an hourly basis. The stations are regularly distributed across the city of Sofia ranging in elevation from 600 to 900 m a.s.l.

Data processing

As the MODIS LST Level-3 product is geometrically, atmospherically, and emissivity corrected, the only pre-processing step that we have applied are a scale factor to the data and a conversion of Kelvin's temperature to degree Celsius. As the MOD11A2 contains eight-day daily and nightly data there were a total of four observations per interception. They were additionally averaged in order to combine TERRA and AQUA MODIS LST Level-3 product and to get more accurate average daily temperature. The task was done by simple averaging method. If one of the four observations was missing we have considered the average value as 'NoData'. There are a total of 46 eight-day MODIS LST scenes (the last one of the yearly time-series is not an eight-day, but five-day average) for 2013. Therefore, we have applied the same averaging method to get the averaged *in-situ* values for the same eight-day interceptions. If more than 3 days for an interception were missing we have considered the average value as 'NoData'.

Table 1. Description of Automatic Meteorological Stations (AWSs) used in the study

AWS name	Data Collection (min)	Latitude (ϕ°)	Longitude (λ°)	Height (m a.s.l.)	AWS Land Cover	MODIS Pixel Land Cover (%)
<i>Sofia Airport</i>	60 min	42.65	23.38	595	Bare ground	100% 'Tall buildings'
<i>Simeonovo</i>	5 min	42.63	23.34	697	Unknown	50 % 'Developed' 50 % 'Bare ground'
<i>Yavorov</i>	5 min	42.69	23.35	554	Unknown	70 % 'Developed' 30 % 'Forest'
<i>Kazichene</i>	5 min	42.66	23.47	542	Tiled roof	75% 'Density houses' 25 % 'Bare ground'
<i>Bistritsa</i>	5 min	42.58	23.37	881	Unknown	100 % 'Bare Ground'
<i>Boyana</i>	5 min	42.64	23.28	744	Unknown	40 % 'Developed' 60 % 'Thick forest'
<i>Manastirski livadi</i>	5 min	42.66	23.28	632	Unknown	70 % 'Developed' 30 % 'Bare ground'
<i>Lyulin</i>	5 min	42.71	23.25	588	Unknown	70 % 'Tall buildings' 30 % 'Bare ground'

There are gaps in the MODIS LST data due to the cloud cover, especially in the winter months. This necessitates filling in the missing values. We have examined two methods to do that by regression equation. The first one considers each MODIS LST observation separately. An independent regression equation has been used to fill the gaps in day/night MODIS TERRA or AQUA LST observations. After that a simple averaging method has been used to extract the average temperatures for each intercept. In the second method we have firstly averaged the different MODIS LST observations and if one of the fourth MODIS LST values has been missing we have assigned 'No Data'. After that the missing values were recovered through a regression equation.

Statistical measures such as: coefficient of determination (R^2), Coefficient of Correlation, Mean Absolute Error (MAE), Root Mean Squared Error (RMSE), and Standard Deviation (SD) were used to compare the so formed two time-series data sets (one terrestrial AWS and one space-borne MODIS LST). As there were gaps in both MODIS LST and AWSs data we have used a regression equation to fill in these gaps. The MODIS LST product with the AWSs' measurements was statistically compared in two ways. Firstly, we have compared the MODIS LST with averaged daily *in-situ* temperature using descriptive statistics. Secondly, we have compared MODIS LST with the *in-situ* data that correspond to the MODIS day-and-night observations.

4. Results and discussions

Comparing single MODIS LST Level-3 product with AWS near surface temperatures

Between the *in-situ* measurements and the MODIS TERRA and AQUA day and night LST observations a correlation was studied. From the visual comparison of Fig. 1, it is obvious that there is strong correlation between AWS *Sofia Airport* and each of MODIS LST observations. However, there are differences in the absolute values. The night time trend lines are closer to AWS trend line than the day time trend lines. Considering day time trend lines a seasonal variation is observed.

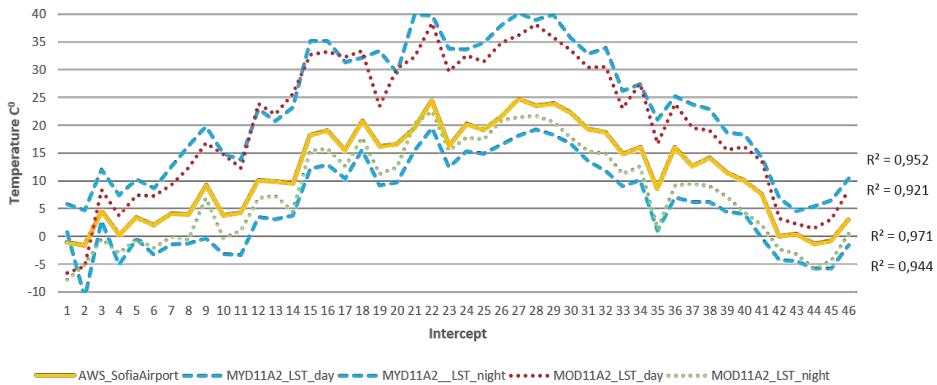


Fig. 1. Comparing temperature measurements (AWS Sofia Airport) with eight-day MODIS LST observations for 2013

Averaging MODIS LST level-3 product

As the trend lines from both 1st and 2nd averaging method are almost identical on the plot, the Table 2 shows the results from 1st method leads to slightly more accurate results.

Table 2. Statistical comparison of the two gap-filling methods

MODIS LST averaging after	1 st method	2 nd method
R ²	0.980	0.979
MAE	2.816	2.892
RMSE	3.534	3.565
SD (95% confidence)	4.271	4.169

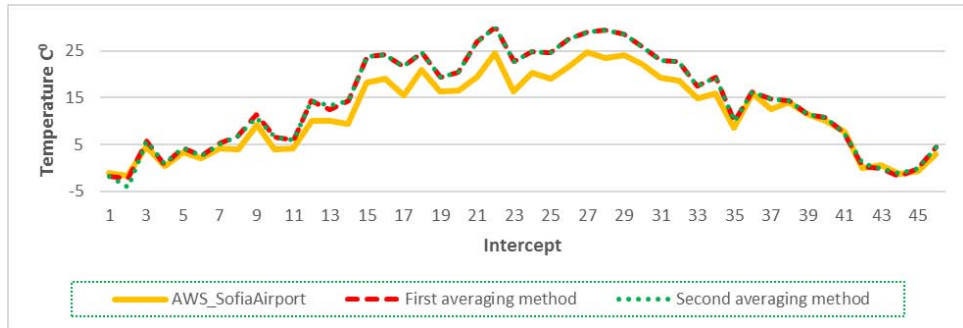


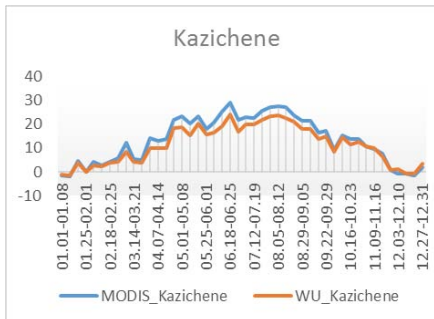
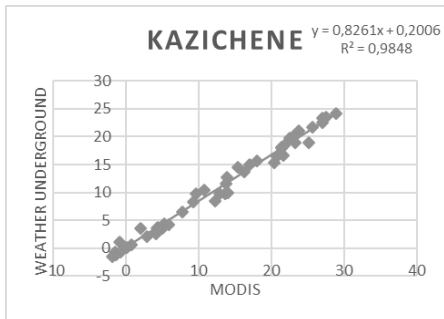
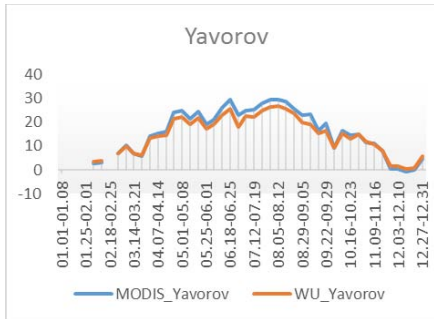
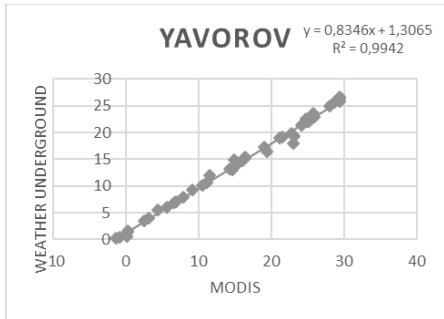
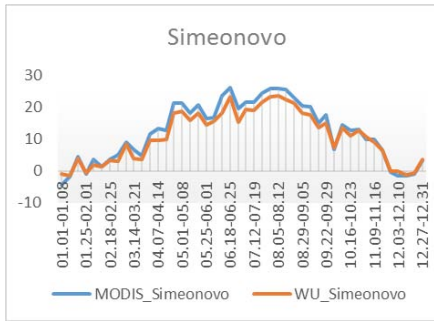
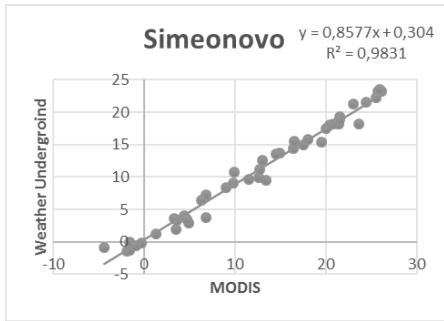
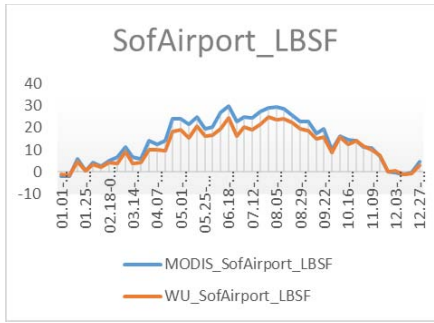
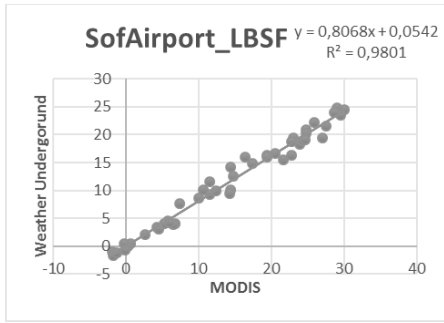
Fig. 2. Comparing AWS Sofia Airport in-situ near-surface temperature observations with averaged MODIS LST observations after the 1st and 2nd method for 2013

Correlation of MODIS LST level-3 product with AWS near-surface temperatures

We have plotted a regression line and trend line for all of the eight AWSs in order to check out the correlation between the two types of data. The correlation coefficient R^2 , among other statistical information, is presented in Table 2.

The MODIS LST Level-3 product has a very strong correlation with all of the AWSs which varies from 0.97 to 0.99. Only AWS *Manastirski livadi* has a value of 0.95. The trend lines moves almost identical in the winter months but in the summer months there is an overestimation from MODIS LST. Exclusions are AWSs *Bistritsa* and *Boyana* where MODIS LST trend line lies on the *in-situ* trend line even in the summer months. These two stations also give the best results. Several statistical parameters have been calculated and are shown in the Table 2. The Mean Bias (which is in fact average T_s – average T_a) is respectively 0.67 and 0.85, the MAE is around 1.1, the RMSE is near 1.4 and SD at 95% confidence is 1.72/1.77. If we divide the results into groups it's apparent the AWSs *Simeonovo*, *Yavorov*, and *Manastirski livadi* have very similar values and the stations *Kazichene* and *Lyulin* form another group with almost identical values. Below this rating is situated AWS *Sofia Airport*. Its Mean Bias is 2.72, the MAE is 2.82, the RMSE – 3.53 and 4.27 SD (95 % confidence). A possible reason for this result is the fact that the MODIS pixel's land-cover is a tall-building area whereas the AWS is located on grassland.

A careful investigation of Fig. 3 confirms our assumption for seasonality in the MODIS LST Level-3 product. In order to check out more carefully this tendency we have analyzed the residuals of MODIS_SofiaAirport data.



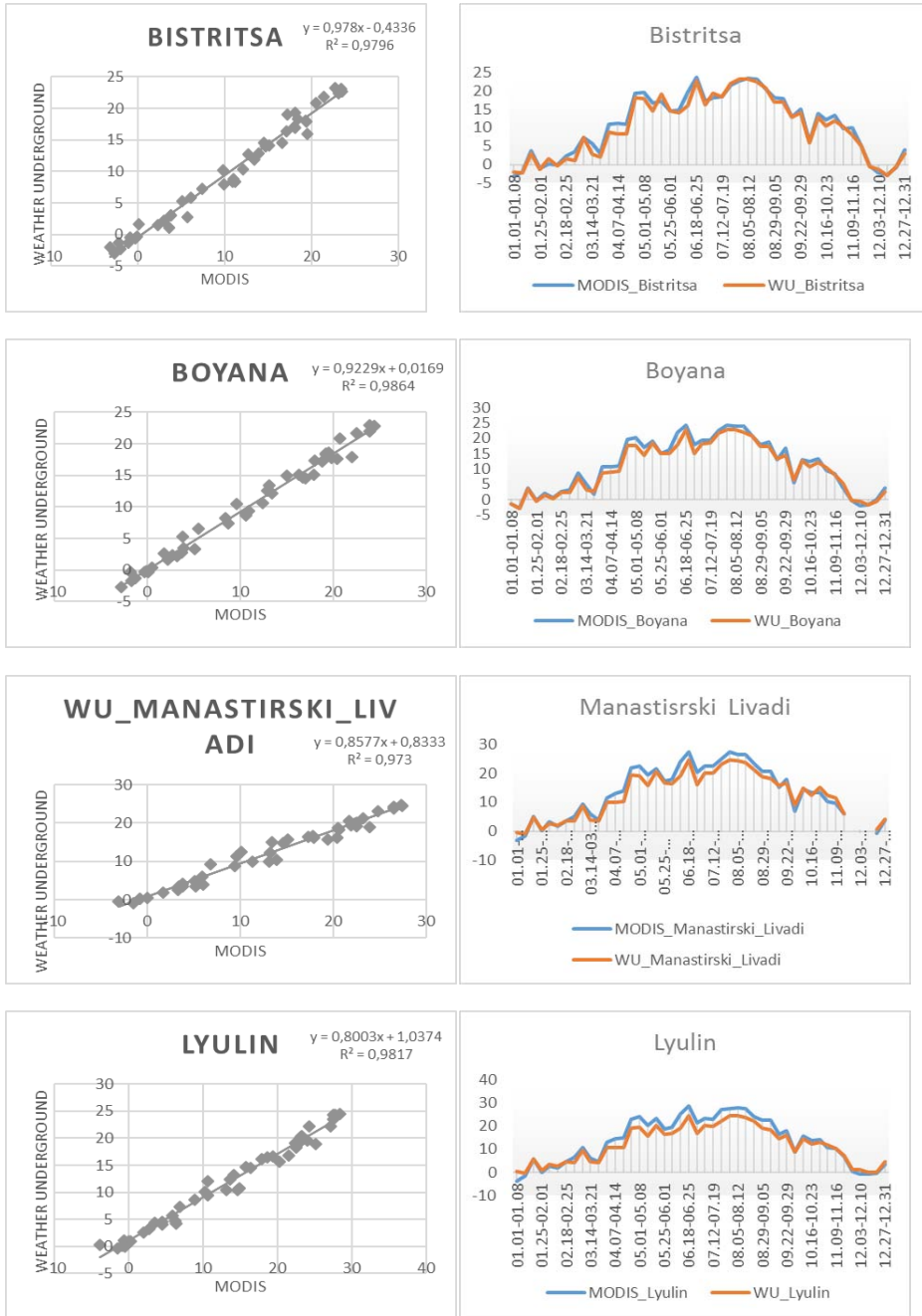


Fig. 3. In-situ (AWS) and MODIS LST regression lines (left) with a comparison of the eight-day time series trends (right) for the eight AWS

Table 3. Descriptive statistics for the AWS data (WU) and MODIS LST pixel values

	MODIS_ Sofia Airport	MODIS_ WU_Sofia Airport	MODIS_ Simeoneo	MODIS_ WU_Simeoneo	MODIS_ Yavorov	MODIS_ WU_Yavorov	MODIS_ Kazichen	MODIS_ WU_Kazichen	MODIS_ Bistritsa	MODIS_ WU_Bistritsa	MODIS_ Boyana	MODIS_ WU_Boyana	MODIS_ Manastirski	MODIS_ WU_Manastirski	MODIS_ Livadi	MODIS_ WU_Livadi	MODIS_ Lyulin	MODIS_ WU_Lyulin
MIN	-1,90	-1,63	-4,37	-1,50	-1,41	0,16	-1,82	-1,50	-3,19	-3,00	-2,81	-2,75	-3,08	-1,00	-3,82	-0,38		
MAX	30,05	24,75	26,14	23,50	29,43	26,63	28,92	24,13	23,57	23,25	24,42	23,00	27,45	24,63	28,45	24,50		
Absolute MIN difference (Ts-Ta)	0,28		2,87		1,57		0,32		0,19		0,06		2,08		3,45			
Absolute MAX difference (Ts-Ta)	5,30		2,64		2,81		4,79		0,32		1,42		2,83		3,95			
RZ	0,97		0,97		0,99		0,98		0,97		0,98		0,95		0,97			
Mean Bias (Ts-Ta)	2,72		1,44		1,16		2,13		0,67		0,85		1,02		1,68			
MAE	2,82		1,80		1,76		2,36		1,06		1,11		1,76		2,27			
RMSE	3,53		2,20		2,13		2,87		1,36		1,42		2,12		2,78			
SD(95% confidence)	4,27		2,52		2,63		3,26		1,72		1,77		2,49		3,21			



Fig. 4. AWS Sofia Airport residual plot

In the first plot on Fig. 4, we have used the near-surface temperature data from AWS *Sofia Airport* for X-axis and the LST data from MODIS pixel at the same location for Y-axis. Until 5 C° the temperatures are underestimated with up to - 2 C° but after this the temperature values of MODIS LST either under or overestimate the real-world ones with ± 2 C°. There could be a tendency for overestimation above 20 C° but these intervals are too small for making general statements. However, the model predicted values are within ± 2 C° for a given observation temperature.

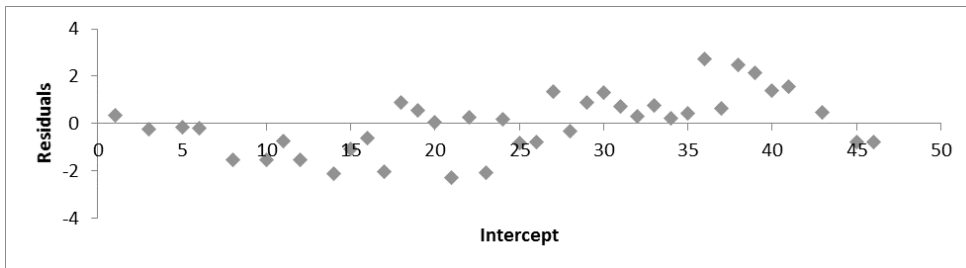


Fig. 5. Intercept residual plot

Observing the second plot on Fig. 5, there are apparently more readable results. This time the intercepts have been plotted on the X-axis. Here it is observed a tendency for a smooth displacement of the predicted values moving through the intercepts. This movement is expressed in underestimation in the winter intercepts, a mixed under- and overestimation in the transitional intercepts, and an overestimation in the summer intercepts.

Land cover influence on the correlation

It is well documented fact that the impervious surfaces raise the LSTs whereas the green/vegetated surfaces lower them [49, 50]. The MODIS LST pixel value is a combination of the thermal properties of all the represented land-cover types [38]. In table 1 we have described the land cover under the MODIS pixels. Comparing the presence of different land cover types to the statistical information in a table 2 it is observed an interesting tendency about the influence of the urban area on the LSTs. Earlier we have combined the statistical results into groups by their rating. A combination of these groups with the pixels' land cover description answers the question about the urban impact on the LST (Table 4).

Table 4. Comparison of statistical groups with pixel land cover types of MODIS LST. The AWS names are encoded from dark grey (worst) to white (best) statistical agreement (in terms of MAE, RMSE, and SD) with MODIS LST values

AWS name	Land use-land-cover class (%)
<i>Sofia Airport</i>	100 % 'Tall buildings'
<i>Simeonovo</i>	50 % 'Developed', 50 % 'Bare ground'
<i>Yavorov</i>	70 % 'Developed', 30 % 'Park'
<i>Kazichene</i>	75 % 'Dense housing with vegetation', 25 % 'Bare ground'
<i>Bistritsa</i>	100 % 'Bare Ground'
<i>Boyana</i>	40 % 'Developed', 60 % 'Thick forest'
<i>Manastirski livadi</i>	70 % 'Developed', 30 % 'Bare ground'
<i>Lyulin</i>	70 % 'Tall buildings', 30 % 'Bare ground'

As we have already stated AWS *Sofia Airport* (dark grey) has the worst statistical result expressed in rising of trend line in summer months and bigger MAE, RMSE, and SD values. The pixel area consists of tall buildings and runways leading to a higher surface temperature. In fact the MODIS LST product measure 5.30°C higher absolute maximum temperature than the AWS *Sofia Airport* (Table 2). The gray group which consists mainly of tall buildings or densely built houses has a slightly better result that may be due to the presence of 25÷30 % bare

ground. The next, pale grey group consists of mix from developed, bare ground, and park areas and the white encoded group, which has the best results, consists of bare ground or prevailing thick forest, i.e. natural formations.

On the other hand, the land cover influences not only the surface temperature, but the air temperature measured by AWSs. Unfortunately, we do not know the precise location of all of the AWSs. Hence, we would not know if a station is on the roof top or on the ground. We only have information for the AWS *Sofia Airport* which is on the ground and AWS *Kazichene* which is on a tiled roof top.

5. Conclusion

A very strong correlation with a pronounced seasonality between MODIS LST Level-3 product and near surface *in-situ* temperature observation exists. The averaged R^2 value is 0.97 with average MAE, RMSE, and SD at 95 % confidence respectively 1.87/2.30/2.73. The results are pronouncedly influenced by the land cover. In fact, the stations with prevailing non-urbanized area have better predicted values (MODIS LST) than the stations with mainly impervious surfaces. The trend lines are almost identical in the winter months but take apart in the summer months. The figure 1 shows this trend holds only for day time MODIS LST observations. From the residual plots and table 3 we can state that the driving force for the seasonality is not the increase of temperatures itself but the sunlight in combination with the presence of impervious surfaces. Considering correlation between these two types of temperature measurements another possible factor could be the altitude. However, with the available data we could not find a strong relationship between MODIS and AWS measurements with respect to the elevation, which is to be studied further. Having stated, that we compare surface versus near-surface temperatures, it is possible to have seasonality in the results which may be influenced by many other climatic processes such as advection.

In conclusion, the strong correlation and the low level of MAE, RMSE, and SD prove the applicability of MODIS LST Level-3 product in UHI studies. It could be suggested that such investigations have to study and model first the local cityscapes LSTs and compare with the LST satellite products and only then to analyze their UHIs to allow for a better analysis of local conditions for decision making.

References

1. Zhang, J., Y. Wang, & Y. Li. A C++ program for retrieving land surface temperature from the data of Landsat TM/ETM+ band 6. *Comp. & Geosci.*, 2006, 32(10), 1796–1805. DOI: 10.1016/j.cageo.2006.05.001 (last accessed: 16 March 2017).

2. Falahatkar, S., S.M. Hosseini, & A. Reza. The relationship between land cover changes and spatial-temporal dynamics of land surface temperature. *Indian J. for Sci. and Tech.*, 2011, 4(2), 76–81. DOI: 10.17485/ijst 2011/v4i2/29937
3. Pongrácz, R., J. Bartholy, & Z. Dezso. Application of remotely sensed thermal information to urban climatology of Central European cities. *Physics and Chemistry of the Earth*, 2010, 35(1–2), 95–99. DOI: 10.1016/j.pce.2010.03.004
4. Atwater, M.A. Thermal changes induced by urbanization and pollutants. *J. of Applied Meteor.*, 1975, 14, 1061–71. DOI: 10.1175/1520-0450(1975)014%3C1061:TCIBUA%3E2.0.CO;2 (last date accessed: 21 December 2016).
5. Ojima, T. Changing Tokyo Metropolitan area and its heat island model. *Energy and Buildings*, 1990, 15(1–2), 191–203. DOI: 10.1016/0378-7788(90)90131-2
6. Voogt, J.A. & T.R. Oke. Thermal remote sensing of urban climates. *Rem. Sens. of Environ.*, 2003, 86(3), 370–384. DOI: 10.1016/S0034-4257(03)00079-8
7. Voogt, J.A. Urban heat islands: hotter cities. *Actionbioscience*. 2004, URL: <http://www.actionbioscience.org/environment/voogt.html>
8. Arnfield, A.J. Two decades of urban climate research: A review of turbulence, exchanges of energy and water, and the urban heat island. *Int. J. of Climatology*, 2003, 23(1), 1–26. DOI: 10.1002/joc.859 (last date accessed: 21 December 2016).
9. Moriyama, M. Estimation of land cover ratio using remote sensing data (LANDSAT MSS) for investigating thermal properties of urban areas. *Energy and Buildings*, 1990, 15(C), 177–181. DOI: 10.1016/0378-7788(90)90129-7
10. Wan, Z. Collection 5 MODIS Land Surface Temperature Products Users' Guide, 2006. http://www.ices.ucsb.edu/modis/LstUsrGuide/MODIS_LST_products_Users_guide_C5.pdf (last date accessed: 21 December 2016).
11. Huang, G., W. Zhou, & M.L. Cadenasso. Understanding the relationship between urban land surface temperature, landscape heterogeneity and social structure. In: 30th IEEE International Geoscience and Remote Sensing Symposium, IGARSS 2010. Center for Regional Change, University of California, Davis, USA, 2010, 3933–36. DOI: 10.1109/IGARSS.2010.5649806 (last date accessed: 21 December 2016).
12. Kottmeier, C., C. Biegert, & U. Corsmeier. Effects of urban land use on surface temperature in Berlin: case study. *J. of Urban Plan. and Develop.*, 2007, 133(2), 128–137. DOI: 10.1061/(ASCE)0733-9488(2007)133:2(128)
13. Rinner, C. & M. Hussain. Toronto's urban heat island-exploring the relationship between land use and surface temperature. *Remote Sensing*, 2011, 3(6), 1251–65.
14. Amiri, R., Q. Weng, A. Alimohammadi, & S.K. Alavipanah. Spatial-temporal dynamics of land surface temperature in relation to fractional vegetation cover and land use/cover in the Tabriz urban area, Iran. *Rem. Sens. of Environ.* 2009, 113(12), 2606–17. DOI: 10.1016/j.rse.2009.07.021
15. Wong, M.S., J.E. Nichol, P.H. To, & J. Wang, A simple method for designation of urban ventilation corridors and its application to urban heat island analysis. *Building and Environment*, 2010, 45(8), 1880–89. DOI: 10.1016/j.buildenv.2010.02.019 (last date accessed: 21 December 2016).
16. Loughner, C.P., J.A. Dale, Z. Da-Lin, K.E. Pickering, R.R. Dickerson, & L. Landry. Roles of Urban Tree Canopy and Buildings in Urban Heat Island Effects: Parameterization and Preliminary Results. *J. of Applied Meteorology and Climatology*, 2012, 51(10), 1775–93. DOI: 10.1175/JAMC-D-11-0228.1

17. Stanganelli, M. & M. Soravia. Connections between urban structure and urban heat island generation: An analysis through remote sensing and GIS. *Lecture Notes in Computer Science (including subseries Lecture Notes in Artificial Intelligence and Lecture Notes in Bioinformatics)*, 2012, 7334 LNCS(PART 2), 599–608. DOI: 10.1007/978-3-642-31075-1_45 (last date accessed: 21 December 2016).
18. Stathopoulou, M., A. Synnefa, C. Cartalis, M. Santamouris, T. Karlessi, & H. Akbari. A surface heat island study of Athens using high-resolution satellite imagery and measurements of the optical and thermal properties of commonly used building and paving materials. *International Journal of Sustainable Energy*, 2009, 28(1–3), 59–76. DOI: 10.1080/14786450802452753 (last accessed: 21 December 2016).
19. Du, M., W. Sun, & G. Cai. Calculation of corridor structure effect on urban heat island using highly spatial resolution satellite images in Beijing, China. In *International Geoscience and Remote Sensing Symposium (IGARSS). 2008 IEEE International Geoscience and Remote Sensing Symposium - Proceedings*. School of Geomatic and Urban Information, Beijing University of Civil Engineering and Architecture, No.1, Zhanlanguan Road, 100044, China, 2008, III1342–III1345. DOI: 10.1109/IGARSS.2008.4779608 (last date accessed: 21 December 2016).
20. Nakata, C.M. & L.C.L. de Souza. Verification of the influence of urban geometry on the nocturnal heat island intensity. *J. of Urban and Environ. Engineering*, 2013, 7(2), 286–292. DOI: 10.4090/juee.2013.v7n2 (last accessed: 21 December 2016).
21. Voogt, J.A. & T.R. Oke. Effects of urban surface geometry on remotely-sensed surface temperature. *International Journal of Remote Sensing*, 1998, 19(5), 895–920. DOI: 10.1080/014311698215784 (last date accessed: 21 December 2016).
22. Di Maria, V., M. Rahman, P. Collins, G. Dondi & C. Sangiorgi. Urban Heat Island effect: thermal response from different types of exposed paved surfaces. *Int. Journal of Pavement Research and Technology*, 2013, 6(4), 414–422. DOI: 10.6135/ijprt.org.tw/2013.6(4).414 (last date accessed: 21 December 2016).
23. Oke, T.R. *Boundary Layer Climates*, Methuen, 1987, 435 p.
24. Gluch, R., D.A. Quattrochi, & J.C. Luvall. A multi-scale approach to urban thermal analysis. *Remote Sensing of Environment*, 2006, 104(2), 123–132. DOI: 10.1016/j.rse.2006.01.025 (last date accessed: 21 December 2016).
25. Voogt, J.A. Assessment of an urban sensor view model for thermal anisotropy. *Rem. Sens. of Environ.*, 2008, 112(2), 482–495. DOI: 10.1016/j.rse.2007.05.013
26. Liu, L. & Y. Zhang. Urban Heat Island analysis using the Landsat TM Data and ASTER data: A case study in Hong Kong. *Rem. Sens.*, 2011, 3(12), 1535–52. DOI: 10.3390/rs3071535 (last date accessed: 21 December 2016).
27. Klok, L., S. Zwart, H. Verhagen & E. Mauri. The surface heat island of Rotterdam and its relationship with urban surface characteristics. *Resources, Conservation and Recycling*, 2012, 64, 23–29. DOI: 10.1016/j.resconrec.2012.01.009
28. Jiang, X., B. Xia, G. Lin & W. Lin. Daily changes of spatial patterns of meteorological elements over Pearl River Delta based on GIS and MM5. *Chin. Geog. Sci.*, 2009, 19(1), 69–76. DOI: 10.1007/s11769-009-0069-1
29. Van, T.T., H. Duong, & X. Bao. A study on urban development through land surface temperature by using remote sensing: in case of Ho Chi Minh City, Southern Vietnam. *Geog. Res.*, 2008, 24, 160–167. DOI: 10.1111/j.1745-5871.2009.00607.x

30. Yang, L. & Y. Li. City ventilation of Hong Kong at no-wind conditions. *Atmos. Environ.*, 2009, 43(19), 3111–21. DOI: 10.1016/j.atmosenv.2009.02.062 (last date accessed: 21 December 2016).
31. Liu, H. & Q. Weng. Seasonal variations in the relationship between landscape pattern and land surface temperature in Indianapolis, USA. *Environ. Monitor. & Assess.*, 2008, 144(1–3), 199–219. DOI: 10.1007/s10661-007-9979-5 (last date accessed: 21 December 2016).
32. Rizwan, A.M., L.Y.C. Dennis, & C. Liu. A review on the generation, determination and mitigation of Urban Heat Island. *J. of Environ. Sci.*, 2008, 20(1), 120–128. DOI: 10.1016/S1001-0742(08)60019-4 (last date accessed: 21 December 2016).
33. Mallick, J. & A. Rahman. Impact of population density on the surface temperature and micro-climate of Delhi. *Current Sci.*, 2012, 102(12), 1708–13. URL: <http://www.currentscience.ac.in/Volumes/102/12/1708.pdf>
34. Weng, Q. Thermal infrared remote sensing for urban climate and environmental studies: Methods, applications, and trends. *ISPRS J. of Photogram. and Rem. Sens.*, 2009, 64(4), 335–344. DOI: 10.1016/j.isprsjprs.2009.03.007
35. Steininger, M.K. Tropical secondary forest regrowth in the Amazon: age, area and change estimation with Thematic Mapper data. *Int. J. of Rem. Sens.*, 1996, 17(1), 9–27. DOI: 10.1080/01431169608948984 (last date accessed: 21 December 2016).
36. Soux, A., J.A. Voogt, & T.R. Oke. A model to calculate what a remote sensor “sees” of an urban surface. *Boundary-Layer Meteor.*, 2004, 111(1), 109–132. DOI: 10.1023/B:BOUN.0000027978.21230.b7 (last accessed: 21 December 2016).
37. Qin, Z. & A. Karnieli. Progress in the remote sensing of land surface temperature and ground emissivity using NOAA-AVHRR data. *Int. J. of Rem. Sens.*, 1999, 20(12), 2367–93. DOI: 10.1080/014311699212074 (last accessed: 21 December 2016).
38. Zhan, W., Y. Chen, J. Zhou, J. Wang, W. Liu, J. Voogt, X. Zhu, J. Quan, & J. Li. Disaggregation of remotely sensed land surface temperature: Literature survey, taxonomy, issues, and caveats. *Rem. Sens. of Environ.*, 2013, 131, 119–139. DOI: 10.1016/j.rse.2012.12.014 (last date accessed: 21 December 2016).
39. EUROSTAT – City Statistics Illustrated, 2015. URL: <http://ec.europa.eu/eurostat/cache/RSI/#?vis=city.statistics> (last date accessed: 21 December 2016).
40. Climate guide of People’s Republic of Bulgaria. Volume 3: Air temperature, soil temperature, frost. Sofia, Bulgaria, 1983. (in Bulgarian)
41. National Statistical Institute (NSI). Population by districts, municipalities, settlements and age to 01.02.2011. <http://goo.gl/UXt2pf> (last accessed: 22 December 2016).
42. MODIS (Moderate Resolution Imaging Spectroradiometer). <http://modis.gsfc.nasa.gov/about/design.php> (last date accessed: 15 December 2016).
43. Sohrabinia, M., W. Rack, & P. Zawar-Reza. Analysis of MODIS LST compared with WRF model and in situ data over the Waimakariri river basin, Canterbury, New Zealand. *Rem. Sens.*, 2012, 4(11), 3501–27. DOI: 10.3390/rs4113501
44. Wan, Z., Y. Zhang, Q. Zhang & Z.-L. Li. Quality assessment and validation of the MODIS global land surface temperature. *Int. J. of Rem. Sens.*, 2004, 25(1), 261–274. DOI: 10.1080/0143116031000116417 (last accessed: 21 December 2016).
45. Wan, Z., & J. Dozier. A generalized split-window algorithm for retrieving land-surface temperature from space. *IEEE Transactions on Geosci. and Rem. Sens.*, 1996, 34(4), 892–905. DOI: 10.1109/36.508406 (last date accessed: 22 December 2016).

46. Snyder, W.C., Z. Wan, Y. Zhang, & Y.Z. Feng. Classification-based emissivity for land surface temperature measurement from space. *Int. J. of Rem. Sens.*, 1998, 19(14), 2753–74. DOI: 10.1080/014311698214497 (last accessed: 22 December 2016).
47. MODIS land validation team. URL: <http://landval.gsfc.nasa.gov/ProductStatus.php?ProductID=MOD11> (last date accessed: 15 December 2016).
48. Weather Underground. URL: <http://www.wunderground.com/about/background.asp> (last date accessed: 15 December 2016).
49. Tomlinson, C.J., L. Chapman, J.E. Thornes & C. Baker. Remote sensing land surface temperature for meteorology and climatology: A review. *Meteorological Applications*, 2011, 18(3), 296–306. DOI: 10.1002/met.287
50. Rajasekar, U. & Q. Weng. Urban heat island monitoring and analysis using a non-parametric model: A case study of Indianapolis. *ISPRS J. of Photogram. and Rem. Sens.*, 2009, 64(1), 86–96. DOI: 10.1016/j.isprsjprs.2008.05.002 (last date accessed: 21 December 2016).

СРАВНИТЕЛЕН АНАЛИЗ МЕЖДУ MODIS LST НИВО-3 СПЪТНИКОВИ ПРОДУКТИ И НАЗЕМНИ ТЕМПЕРАТУРНИ ИЗМЕРВАНИЯ ЗА ОЦЕНКА НА ГРАДСКИЯ ТОПЛИНЕН ОСТРОВ НА ГР. СОФИЯ

И. Янев, Л. Филчев

Резюме

В настоящето изследване използваме осемдневни спътникови продукти ниво-3 за глобалната температура на земната повърхност и топлинното излъчване от спътниковия сензор MODIS (MOD11A2 и MYD11A2) и наземни данни от автоматични климатични станции (АКС) за анализиране на пригодността и надеждността на спътниковите данни за оценка на градския топлинен остров на гр. София, България. За целта са сравнени наземни температурни данни от осем АКС с извлечени пикселни стойности от MODIS LST Ниво-3 продукти за 2013 г. Така получената времева серия е осреднена за привеждане в съответствие с MODIS LST Ниво-3 продуктите. Липсващите данни във времевата серия са запълнени с помощта на корелационен анализ между спътниковите и наземни температурни данни. Установена е много силна положителна корелационна зависимост ($R^2 \sim 0.97$ при 95 % доверителен интервал) за осемте АКС, чиито денонощна и сезонна динамика беше анализирана. Изказано е предположението, че добре изразените денонощни и сезонни колебания в температурния тренд и корелацията между спътниковите MODIS LST Ниво-3 продукти и наземни данни, са преди всичко свързани със смесения пиксел от MODIS (с различни типове земеползване/земно-покритие).

QUATERNION-BASED AUTOPILOT FOR DODECACOPTERS - PART I

Svetoslav Zabunov

e-mail: SvetoslavZabunov@gmail.com

Abstract

The innovations in modern unmanned aerial vehicles do pose higher requirements against the autopilot aircraft control. Special demand is placed by the multirotor innovative helicopters for their unique control system and rotor positions.

The current article establishes the core of a quaternion based autopilot suitable for the innovative and award winning twelve rotor UAV helicopter Bulgarian Knight. Quaternions offer a number of benefits to autopilot systems, but their implementation to specialized autopilots used in innovative and unique drone models require exclusive attention and discussion. As a result, an efficient and flexible autopilot is attained, because quaternion computations are much faster and accurate than the other competing approaches. Nevertheless, a quaternion-based autopilot requires sophisticated software libraries with inherent significant complexity. The elevated accuracy and pliability of the quaternion method is a fertile means for developing a prototype, scientific and research autopilot that is suitable for customization in response to the novel UAVs specific needs.

Notation legend:

\vec{a}	Vectors are denoted with italic letters and an arrow above.
\mathbf{a}	Quaternions are denoted with bold letters.
$\mathbf{0}$	Zero quaternion.
$\mathbf{1}$	Identity quaternion.
\mathbb{A}	Matrices are denoted by blackboard bold letters.
$\mathbb{0}$	Zero matrix.
$\mathbb{1}$	Identity matrix.

Introduction

The modern era of unmanned aerial vehicles (UAVs) presumes highly robotized autonomous flying machines, controlled by an onboard powerful computer in their flight maneuvers and actions. The foremost control process of the aircraft is the flight control, which is carried out by the autopilot. Almost all autopilots nowadays are constructed using quaternion algebra and quaternion analysis, due to the unquestionable performance benefits of this mathematical apparatus [1, 2].

The more complex the drones become, the more sophisticated the autopilots have to be in order to respond to the higher demands of control manipulations the newer UAVs encounter [3]. In pursuit of higher stability, invulnerability, reliability, efficiency, lower noise, either mechanical or electromagnetic, and higher safety, a larger number of rotors is often advised. Among the consumer multirotor drones the highest rotor number often is eight and the airframe topology used is the classic “star” topology. Neither the number of eight for the rotors, nor the “star” topology is optimal in terms of the above sought benefits. Of course, as the number of rotors increases, gradually establishes a prohibitively elevated complexity of the machine thus overthrowing the benefits of the greater number of rotors. There is a ‘sweet spot’ and it begins at twelve rotors, because 12 is the lowest even number of rotors a multirotor helicopter must have in order to implement an airframe structure with optimal geometric covering (figure 1). Going from twelve rotors up the optimal geometric covering may be preserved, but the complexity of the flying machine will go higher and the airframe normalized weight will increase. The airframe normalized weight is the airframe total weight divided by the number of rotors.

This article focuses on the quaternion mathematical apparatus utilized in the innovative twelve-rotor drone helicopter – *The Bulgarian Knight* (Fig. 1).

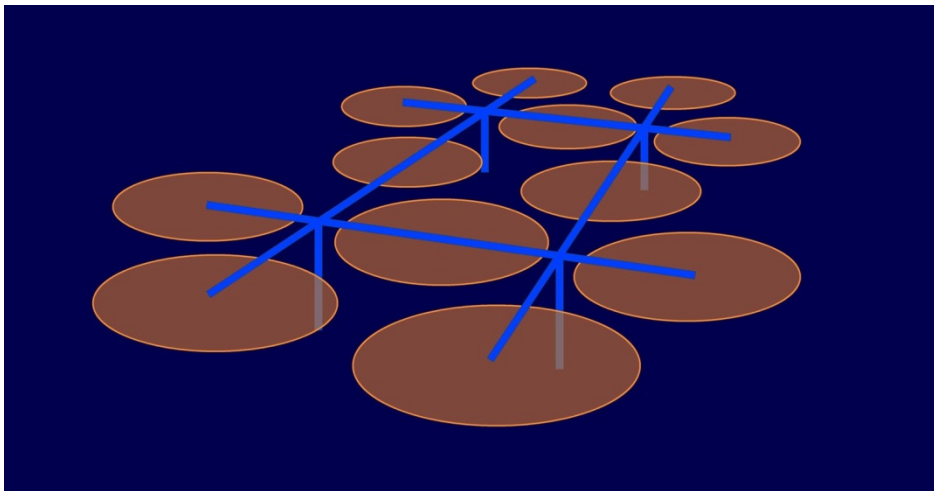


Fig. 1. Bulgarian Knight award winning dodeca-copter

Quaternion analysis suitability to autopilot systems

Quaternions are used mostly to present rotations, but may be applied to the whole mathematical apparatus for computations including all mechanical models

the autopilot implements such as the 3D geometric model, 3D kinematic model, 3D dynamic model, and so on [4].

Nevertheless, the rotation matrix is the most common mathematical object used to hold spatial rotations in the three dimensional Euclidean space as described in [5]. There are other means as well, such as Euler angles and quaternions [6]. The latter have certain well pronounced benefits over the other approaches such as:

1. A smaller number of scalars used to describe the rotation, compared to a matrix form: 4 instead of 9 scalars. Thus the rotation quaternion consumes less computer memory.
2. Smaller number of mathematical operations required to calculate a rotation compared to the matrix form [7].
3. Easier to normalize than a rotation matrix.
4. Gimbal lock is not present as is the case with Euler angles.
5. Rotation quaternion exhibits slower degradation due to accumulation of numerical errors than the rotation matrix [8]. The degradation raises distortion of the rotation matrix orthogonality.
6. The transformation from rotation quaternion to another representation is fast and comfortable. This is not the case with rotation matrix and Euler angles [9].
7. When a rotation matrix is irreplaceable, the transformations between rotation quaternion and rotation matrix are convenient and reasonably fast [10].

All the above advantages gain the predilection for quaternions as the method of choice used to realize spatial rotations in autopilot systems, especially in autopilots with high level of safety, efficiency and computing accuracy. Hence, in most modern autopilot systems, from small drones to large airplanes the preferred mathematical method is quaternions.

Quaternion prerequisites

Quaternions were introduced by W. Hamilton in the year of 1843 [11]. Later, vector analysis followed as a result of quaternion analysis simplification [12]. The next paragraphs will briefly summarize the quaternion mathematical basic principles to aid the reader in comprehending all formulations about autopilot algorithms presented in the following sections of the current paper [13]. For deduction of some of the formulas and thorough examination of quaternion properties the reader may consult the following books on quaternions [5, 14–16].

A quaternion is defined through three objects called fundamental quaternion units: \mathbf{i} , \mathbf{j} , and \mathbf{k} . There is a strong resemblance to complex numbers, but a quaternion has four elements instead of two. Hamilton defined quaternions as follows [11]:

$$(1) \quad \mathbf{a} = w + x\mathbf{i} + y\mathbf{j} + z\mathbf{k}$$

In (1) \mathbf{a} is a quaternion with elements w , x , y , and z . Other notations are: $(w, x, y, z) \Leftrightarrow [w, \vec{v}] \Leftrightarrow w + x\mathbf{i} + y\mathbf{j} + z\mathbf{k}$, where \vec{v} is a three-dimensional vector (x, y, z) .

Note that lowercase bold is used to denote quaternions in this article. The basis elements themselves are quaternions. The basis element scalar 1 is the identity element and is represented by the identity quaternion:

$$(2) \quad \mathbf{1} = (1, 0, 0, 0) = [1, 0] = 1$$

The zero quaternion is a quaternion with all elements zeros:

$$(3) \quad \mathbf{0} = (0, 0, 0, 0) = [0, 0] = 0$$

A quaternion is invariant under multiplication by 1. Quaternion multiplication is defined through the products of the basis elements:

$$(4) \quad \mathbf{ii} = \mathbf{jj} = \mathbf{kk} = \mathbf{ijk} = -1$$

This equation was carved by Hamilton on a stone on Brougham Bridge over the Royal Canal in Dublin on October 16th, 1843. It holds all the essence of quaternions. From (2) it is easy to derive all combinations of basis products:

$$(5) \quad \mathbf{ij} = \mathbf{k}, \mathbf{jk} = \mathbf{i}, \mathbf{ki} = \mathbf{j}$$

$$(6) \quad \mathbf{ji} = -\mathbf{k}, \mathbf{kj} = -\mathbf{i}, \mathbf{ik} = -\mathbf{j}$$

From (4), (5), and (6) the general multiplication of two quaternions is derived:

$$(7) \quad \mathbf{qq}' = (w + x\mathbf{i} + y\mathbf{j} + z\mathbf{k})(w' + x'\mathbf{i} + y'\mathbf{j} + z'\mathbf{k}) = [ww' - \vec{v}\vec{v}', w\vec{v}' + w'\vec{v} + \vec{v} \times \vec{v}']$$

Quaternions addition and multiplication operations obey the associative law:

$$(8) \quad (\mathbf{q} + \mathbf{q}') + \mathbf{q}'' = \mathbf{q} + (\mathbf{q}' + \mathbf{q}'')$$

$$(9) \quad (\mathbf{qq}')\mathbf{q}'' = \mathbf{q}(\mathbf{q}'\mathbf{q}'')$$

These two operations obey also the distributive law:

$$(10) \quad \mathbf{q}(\mathbf{q}' + \mathbf{q}'') = \mathbf{q}\mathbf{q}' + \mathbf{q}\mathbf{q}''$$

Further, the addition law is commutative:

$$(11) \quad \mathbf{q} + \mathbf{q}' = \mathbf{q}' + \mathbf{q}$$

For the product of a quaternion with itself one obtains:

$$(12) \quad \mathbf{q}^2 = [w^2 - \vec{v}^2, 2w\vec{v}]$$

One should notice that the quaternion product is non-commutative:

$$(13) \quad \mathbf{q}\mathbf{q}' \neq \mathbf{q}'\mathbf{q}$$

The quaternion conjugate is defined as:

$$(14) \quad \tilde{\mathbf{q}} = w - \mathbf{x}\mathbf{i} - \mathbf{y}\mathbf{j} - \mathbf{z}\mathbf{k} = [w, -\vec{v}]$$

The product of a quaternion with its conjugate has similar properties to complex numbers:

$$(15) \quad \mathbf{q}\tilde{\mathbf{q}} = \tilde{\mathbf{q}}\mathbf{q} = [ww + \vec{v}\vec{v}, -w\vec{v} + w\vec{v}] = [w^2 + \vec{v}^2, \mathbf{0}] = w^2 + x^2 + y^2 + z^2$$

And also the following rule holds:

$$(16) \quad (\mathbf{qp})^\sim = \tilde{\mathbf{p}}\tilde{\mathbf{q}}$$

Quaternion norm is used to keep a unit rotation quaternion stable:

$$(17) \quad |\mathbf{q}| = \sqrt{\mathbf{q}\tilde{\mathbf{q}}} = \sqrt{\tilde{\mathbf{q}}\mathbf{q}} = \sqrt{w^2 + x^2 + y^2 + z^2} = |\tilde{\mathbf{q}}|$$

A multiplicative law is applicable to the norm:

$$(18) \quad |\mathbf{pq}| = |\mathbf{p}||\mathbf{q}| = |\mathbf{q}||\mathbf{p}| = |\mathbf{qp}|$$

The unit quaternion is defined as the quaternion divided by its norm. It is also called a versor:

$$(19) \quad \mathbf{n}_q = \frac{\mathbf{q}}{|\mathbf{q}|}$$

The unit quaternion has a unit norm:

$$(20) \quad |\mathbf{n}_q| = 1$$

With finite rotations (they shall be called just rotations from now on), the order they are applied to a vector matters. Rotations are naturally expressed by algebraic systems with non-commutative products. At first glance, the non-commutability would affect the quaternion reciprocal:

$$\mathbf{q}\mathbf{q}_r^{-1} = \mathbf{q}_l^{-1}\mathbf{q} = \mathbf{1} \text{ and it is expected that } \mathbf{q}_r^{-1} \neq \mathbf{q}_l^{-1}$$

But taking into view (15) it is observed that:

$$(21) \quad \frac{\mathbf{q}\tilde{\mathbf{q}}}{|\mathbf{q}|^2} = \frac{\tilde{\mathbf{q}}\mathbf{q}}{|\mathbf{q}|^2} = \mathbf{1} \Rightarrow \mathbf{q}^{-1} = \mathbf{q}_l^{-1} = \mathbf{q}_r^{-1} = \frac{\tilde{\mathbf{q}}}{|\mathbf{q}|^2}$$

An important property of the versor is that its reciprocal is equal to its conjugate. This formula follows from (17) and (21):

$$(22) \quad \mathbf{n}_q^{-1} = \left(\frac{\mathbf{q}}{|\mathbf{q}|} \right)^{-1} = |\mathbf{q}|\mathbf{q}^{-1} = |\mathbf{q}|\frac{\tilde{\mathbf{q}}}{|\mathbf{q}|^2} = \frac{\tilde{\mathbf{q}}}{|\mathbf{q}|} = \frac{\tilde{\mathbf{q}}}{|\tilde{\mathbf{q}}|} = \tilde{\mathbf{n}}_q$$

According to the above properties of quaternions and taking into account that for any nonzero quaternion \mathbf{q} , there is a quaternion $-\mathbf{q}$ such that $\mathbf{q} + (-\mathbf{q}) = \mathbf{0}$ and the non-commutative law it follows that quaternions are a non-commutative division ring. If quaternions had a commutative product they would have been a field.

As mentioned above, the three dimensional rotation is an important procedure in autopilot systems. The rotation is defined as follows:

$$(23) \quad \mathbf{q}_R = \left[\cos \frac{\theta}{2}, \vec{n} \sin \frac{\theta}{2} \right]$$

In (23) \vec{n} is a unit vector specifying the axis of rotation and θ is the angle of rotation. It should be noted that the rotation quaternion is a versor [17]:

$$(24) \quad \begin{aligned} |\mathbf{q}_R| &= \sqrt{\mathbf{q}_R \tilde{\mathbf{q}}_R} = \sqrt{\cos^2 \frac{\theta}{2} + \sin^2 \frac{\theta}{2} (x^2 + y^2 + z^2)} = \\ &= \sqrt{\cos^2 \frac{\theta}{2} + \sin^2 \frac{\theta}{2}} = \sqrt{1} = 1 \end{aligned}$$

Immediately follows that the reciprocal of the rotation quaternion is its conjugate:

$$(25) \quad \mathbf{q}_R^{-1} = \tilde{\mathbf{q}}_R$$

The rotation operator on a vector using a rotation quaternion is as follows:

$$(26) \quad \mathbf{q}_R \mathbf{v} \tilde{\mathbf{q}}_R = \mathbf{q}_R \mathbf{v} \mathbf{q}_R^{-1}$$

Here quaternion $\mathbf{v} = [0, \vec{v}]$ represents the vector that is to be rotated. Changing the sign of the rotation quaternion gives the same rotation:

$$(27) \quad \begin{aligned} -\mathbf{q}_R &= \left[-\cos \frac{\theta}{2}, -\vec{n} \sin \frac{\theta}{2} \right] = \left[\cos \left(\pi + \frac{\theta}{2} \right), \vec{n} \sin \left(\pi + \frac{\theta}{2} \right) \right] = \\ &= \left[\cos \left(\frac{2\pi + \theta}{2} \right), \vec{n} \sin \left(\frac{2\pi + \theta}{2} \right) \right] \end{aligned}$$

Obviously, quaternion $-\mathbf{q}_R$ rotates by an angle of $2\pi + \theta$, but this is the same rotation as rotating by θ , because $2\pi = 360^\circ$ adds full turn to the rotation and does not act as a transformation. To perform an inverse rotation to an angle of $-\theta$ one should use the conjugate of the rotation quaternion:

$$(28) \quad \tilde{\mathbf{q}}_R \mathbf{v} \mathbf{q}_R = \mathbf{q}_R^{-1} \mathbf{v} \mathbf{q}_R$$

Applying two consecutive rotations \mathbf{p}_R and \mathbf{q}_R yields:

$$(29) \quad \mathbf{p}_R \mathbf{q}_R \mathbf{v} \tilde{\mathbf{q}}_R \tilde{\mathbf{p}}_R = \mathbf{p}_R \mathbf{q}_R \mathbf{v} (\mathbf{p}_R \mathbf{q}_R)^\sim = \mathbf{t}_R \mathbf{v} \tilde{\mathbf{t}}_R$$

The new composite rotation is $\mathbf{t}_R = \mathbf{p}_R \mathbf{q}_R$. The rotation of a product of two vectors, represented as quaternions, is equal to the product of the rotations of these two vectors, represented as quaternions:

$$(30) \quad \mathbf{q}_R \mathbf{a} \mathbf{b} \tilde{\mathbf{q}}_R = \mathbf{q}_R \mathbf{a} \tilde{\mathbf{q}}_R \mathbf{q}_R \mathbf{b} \tilde{\mathbf{q}}_R$$

Autopilots perform numerical integration according to their kinematic and dynamic models [18]. For this purpose differentiation of the rotation quaternion is required. The derivative of a rotation quaternion, in respect to time, is as follows [19]:

$$(31) \quad \frac{d\mathbf{q}_R}{dt} = \dot{\mathbf{q}}_R = \frac{1}{2} \boldsymbol{\omega} \mathbf{q}_R$$

Quaternion $\boldsymbol{\omega} = [0, \vec{\omega}]$. Vector $\vec{\omega}$ is the vector of the angular velocity. By differentiating (31), the second derivative may be obtained as follows:

$$(32) \quad \ddot{\mathbf{q}}_R = \frac{1}{2} \dot{\boldsymbol{\omega}} \mathbf{q}_R + \frac{1}{2} \boldsymbol{\omega} \dot{\mathbf{q}}_R = \frac{1}{2} \boldsymbol{\varepsilon} \mathbf{q}_R + \frac{1}{4} \boldsymbol{\omega}^2 \mathbf{q}_R$$

Quaternion $\boldsymbol{\varepsilon} = [0, \vec{\varepsilon}]$ represents the vector of the angular acceleration $\vec{\varepsilon}$. The derivative product rule in regard to time holds for quaternions. One should notice that in the general case of product of two quaternion functions with quaternion arguments the derivative product rule in regard to a quaternion variable does not hold [20].

Finally, the autopilot control calculations may require at certain places transformation from rotation matrix to rotation quaternion and vice versa. The transformation from rotation quaternion to rotation matrix is performed according to the next formula [21]:

$$(33) \quad \mathbb{R} = \begin{bmatrix} w^2 + x^2 - y^2 - z^2 & 2xy - 2wz & 2xz + 2wy \\ 2xy + 2wz & w^2 - x^2 + y^2 - z^2 & 2yz - 2wx \\ 2xz - 2wy & 2yz + 2wx & w^2 - x^2 - y^2 + z^2 \end{bmatrix} = \begin{bmatrix} R_{00} & R_{01} & R_{02} \\ R_{10} & R_{11} & R_{12} \\ R_{20} & R_{21} & R_{22} \end{bmatrix}$$

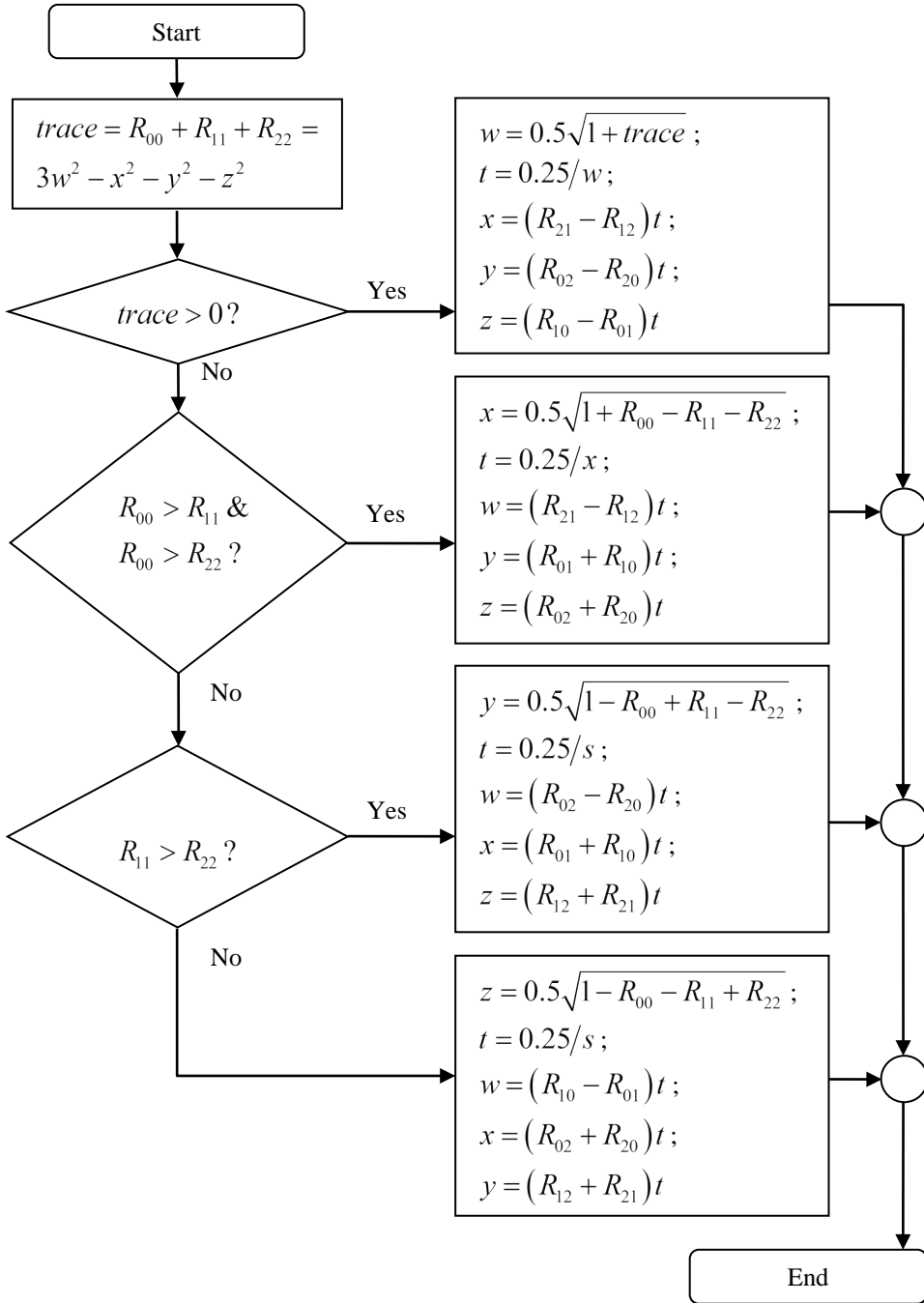


Fig. 2. Rotation matrix to rotation quaternion transformation algorithm

This rotation matrix may be used to rotate a row-matrix presented vector \mathbf{k} using the operator $\mathbf{k}\mathbb{R}$. The transformation from rotation matrix to rotation quaternion is more complex, due to a concern about the numerical stability. Division by small numbers needs to be avoided [21]. The idea is illustrated with the algorithm presented on figure 2. The algorithm first checks if the trace of the matrix is positive. In this case $|w| > 0.5$. If this condition is not met, the largest diagonal element is chosen, because it corresponds to the largest of the other three quaternion components absolute values $|x|$, $|y|$, or $|z|$. One of the latter three must be larger than $|w| > 0.5$.

3D geometric parallel between quaternions, vectors and matrices

There are many 3D geometric operations that are required to be implemented in an autopilot. Most of these operations are well known from vectors and matrices, but not so evident when utilizing quaternions. A discussion of such operations follows.

A vector may be presented in matrix form as a one-column or one-row matrix. This paper uses the one-row notation. As shown in (26) a quaternion may represent a vector:

$$(34) \quad \vec{k} \Leftrightarrow \mathbf{k} = [x \quad y \quad z] \Leftrightarrow \mathbf{k} = [0, \vec{k}]$$

Using (7) the dot and cross products of two vectors represented as quaternions may be easily calculated:

$$(35) \quad \mathbf{k}\mathbf{k}' = (0 + x\mathbf{i} + y\mathbf{j} + z\mathbf{k})(0 + x'\mathbf{i} + y'\mathbf{j} + z'\mathbf{k}) = [-\vec{k}\vec{k}', \vec{k} \times \vec{k}']$$

From (35) it follows that the dot product of two vectors represented as quaternions is:

$$(36) \quad \vec{k}\vec{k}' \Leftrightarrow -\text{Re}(\mathbf{k}\mathbf{k}')$$

In (36) function $\text{Re}(\)$ returns the real part of a quaternion w . The cross product of two vectors is computed in a similar way:

$$(37) \quad \vec{k} \times \vec{k}' \Leftrightarrow \text{Im}(\mathbf{k}\mathbf{k}')$$

Again, in (37) function $\text{Im}(\)$ returns the pure imaginary part $x\mathbf{i} + y\mathbf{j} + z\mathbf{k}$.

A general kinematic model based on quaternions used in autopilots

In this section the equations describing particle kinematics in a non-inertial reference frame are examined using quaternion formalism instead of vector formalism or matrix formalism. Let $Oxyz$ be the inertial and not moving reference frame and $O'x'y'z'$ be a non-inertial, moving and rotating reference frame (Fig. 3). All variables in regard to the inertial reference frame are non-primed and all variables in regard to the non-inertial reference frame are primed.

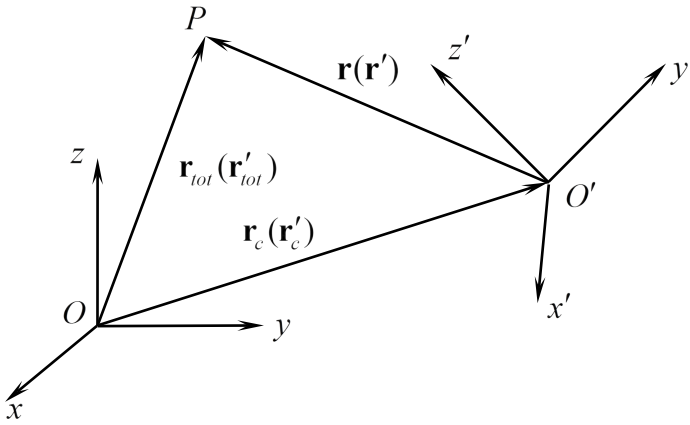


Fig. 3. Kinematics of a point particle P in regard to an inertial reference frame $Oxyz$ and non-inertial reference frame $O'x'y'z'$ described by quaternions

The non-inertial reference frame $O'x'y'z'$ has position \mathbf{r}_c and orientation \mathbf{q} in regard to the inertial reference frame $Oxyz$. The latter two quantities are quaternions. Quaternion \mathbf{r}_c represents a vector and has zero real part. Quaternion \mathbf{q} is a rotational quaternion. The position of the particle P in reference frame $Oxyz$ is \mathbf{r}_{tot} and in reference frame $O'x'y'z'$ is \mathbf{r}' . Quaternion \mathbf{r}' in regard to reference frame $Oxyz$ is $\mathbf{r} = \mathbf{q}\mathbf{r}'\tilde{\mathbf{q}}$:

$$(38) \quad \mathbf{r}_{tot} = \mathbf{r}_c + \mathbf{r} = \mathbf{r}_c + \mathbf{q}\mathbf{r}'\tilde{\mathbf{q}}$$

To proceed further with the derivatives of (38) the reader must consider the following equations that follow from (31):

$$(39) \quad \dot{\mathbf{q}} = \frac{1}{2} \boldsymbol{\omega} \mathbf{q} = \frac{1}{2} \mathbf{q} \tilde{\mathbf{q}} \boldsymbol{\omega} \mathbf{q} = \frac{1}{2} \mathbf{q} \boldsymbol{\omega}'$$

$$(40) \quad \boldsymbol{\omega} = 2\dot{\mathbf{q}}\tilde{\mathbf{q}}$$

$$(41) \quad \boldsymbol{\omega}' = 2\tilde{\mathbf{q}}\dot{\mathbf{q}}$$

The derivative of the rotation quaternion conjugate will also be utilized. Hence it is deduced in the following equation:

$$(42) \quad \mathbf{q}\tilde{\mathbf{q}} = 1 \Rightarrow \frac{d}{dt}(\mathbf{q}\tilde{\mathbf{q}}) = 0 \Rightarrow \dot{\mathbf{q}}\tilde{\mathbf{q}} + \mathbf{q}\dot{\tilde{\mathbf{q}}} = 0 \Rightarrow \dot{\mathbf{q}}\tilde{\mathbf{q}} = -\mathbf{q}\dot{\tilde{\mathbf{q}}} \Rightarrow \dot{\tilde{\mathbf{q}}} = -\tilde{\mathbf{q}}\dot{\mathbf{q}}$$

By elaborating further on (42) one obtains:

$$(43) \quad \dot{\tilde{\mathbf{q}}} = -\tilde{\mathbf{q}}\dot{\mathbf{q}}\tilde{\mathbf{q}} = -\frac{1}{2}\tilde{\mathbf{q}}\boldsymbol{\omega}\mathbf{q}\tilde{\mathbf{q}} = -\frac{1}{2}\tilde{\mathbf{q}}\boldsymbol{\omega}$$

And also:

$$(44) \quad \dot{\mathbf{q}} = -\tilde{\mathbf{q}}\dot{\tilde{\mathbf{q}}}\tilde{\mathbf{q}} = -\frac{1}{2}\tilde{\mathbf{q}}\boldsymbol{\omega}\mathbf{q}\tilde{\mathbf{q}} = -\frac{1}{2}\boldsymbol{\omega}'\tilde{\mathbf{q}}$$

Deriving $\boldsymbol{\omega}$ from (43) results in:

$$(45) \quad \boldsymbol{\omega} = -2\mathbf{q}\dot{\tilde{\mathbf{q}}}$$

When applying the rotation operator with quaternions we should mark off that its derivative has the form.

$$(46) \quad \begin{aligned} \frac{d}{dt}(\mathbf{q}\mathbf{a}'\tilde{\mathbf{q}}) &= \dot{\mathbf{q}}\mathbf{a}'\tilde{\mathbf{q}} + \mathbf{q}\dot{\mathbf{a}}'\tilde{\mathbf{q}} + \mathbf{q}\mathbf{a}'\dot{\tilde{\mathbf{q}}} = \\ &= \frac{1}{2}\mathbf{q}\boldsymbol{\omega}'\mathbf{a}'\tilde{\mathbf{q}} + \mathbf{q}\dot{\mathbf{a}}'\tilde{\mathbf{q}} - \frac{1}{2}\mathbf{q}\mathbf{a}'\boldsymbol{\omega}'\tilde{\mathbf{q}} = \mathbf{q}\boldsymbol{\omega}'\mathbf{a}'\tilde{\mathbf{q}} + \mathbf{q}\dot{\mathbf{a}}'\tilde{\mathbf{q}} \end{aligned}$$

The above equation relies on the property of the quaternion product to be anti-commutative when the two quaternions have zero real part (represent vectors).

Now (38) may be differentiated to obtain the equation of speed:

$$(47) \quad \mathbf{v}_{tot} = \dot{\mathbf{r}}_{tot} = \dot{\mathbf{r}}_C + \dot{\mathbf{r}} = \dot{\mathbf{r}}_C + \mathbf{q}\omega'\mathbf{r}'\tilde{\mathbf{q}} + \mathbf{q}\dot{\mathbf{r}}'\tilde{\mathbf{q}} = \mathbf{v}_C + \mathbf{q}\mathbf{v}'\tilde{\mathbf{q}} + \mathbf{q}\omega'\mathbf{r}'\tilde{\mathbf{q}}$$

And differentiating again the equation of acceleration is deduced:

$$(48) \quad \mathbf{a}_{tot} = \ddot{\mathbf{r}}_{tot} = \ddot{\mathbf{r}}_C + \ddot{\mathbf{r}} = \mathbf{a}_C + \mathbf{q}\mathbf{a}'\tilde{\mathbf{q}} + 2\mathbf{q}\omega'\mathbf{v}'\tilde{\mathbf{q}} + \mathbf{q}\omega'\text{Im}(\omega'\mathbf{r}')\tilde{\mathbf{q}} + \mathbf{q}\varepsilon'\mathbf{r}'\tilde{\mathbf{q}}$$

Equation (48) may be written entirely in the inertial reference frame:

$$(49) \quad \mathbf{a}_{tot} = \mathbf{a}_C + \mathbf{a} + 2\omega\mathbf{v} + \omega\text{Im}(\omega\mathbf{r})\mathbf{r} + \varepsilon\mathbf{r}$$

or in the non-inertial reference frame:

$$(50) \quad \mathbf{a}' = \mathbf{a}'_{tot} - \mathbf{a}'_C - 2\omega'\mathbf{v}' - \omega'\text{Im}(\omega'\mathbf{r}') - \varepsilon'\mathbf{r}'$$

The terms in (50) are the different accelerations that appear when a particle is moving in a non-inertial reference frame:

$$(51) \quad \mathbf{a}'_{net} = \mathbf{a}'_{tot} - \mathbf{a}'_C \quad - \text{net inertial acceleration in quaternion form}$$

$$(52) \quad \mathbf{a}'_{cor} = -2\omega'\mathbf{v}' \quad - \text{Coriolis acceleration in quaternion form}$$

$$(53) \quad \mathbf{a}'_{cen} = -\omega'\text{Im}(\omega'\mathbf{r}') \quad - \text{centrifugal acceleration in quaternion form}$$

$$(54) \quad \mathbf{a}'_{ang} = -\varepsilon'\mathbf{r}' \quad - \text{Euler acceleration in quaternion form}$$

In the above four equations only the imaginary part of the result is of significance, as it holds a vector. The real part should be ignored.

A general dynamic model based on quaternions used in autopilots

The most common dynamic model with variances used in autopilots is the rigid body motion model of the aircraft. Further in this section the rigid body motion dynamic model shall be discussed in terms of quaternion implementation. On Fig. 4 a numerical 3D simulation is used to visualize the examined

phenomenon. The body reference frame $O'x'y'z'$ (non-inertial) is drawn with cyan colored vector arrows. The space reference frame $Oxyz$ (inertial) is visualized using white arrows. Angular momentum vector \vec{L} is shown in magenta color. The external force arm coincides with $\vec{O'z'}$ vector. The external force vector \vec{F} is in red color and the moment of external force vector \vec{M} is drawn in green color. The orange vector is the angular velocity vector $\vec{\omega}$.

The equations of rigid body motion also known as Euler equations in matrix form are as follows:

$$(55) \quad \mathbf{L}' = \boldsymbol{\omega}' \mathbf{I}' \Rightarrow \mathbf{L}' \mathbf{R} = \boldsymbol{\omega}' \mathbf{R} \mathbf{R}' \mathbf{I}' \mathbf{R} \Rightarrow \mathbf{L} = \boldsymbol{\omega} \mathbf{I}$$

$$(56) \quad \mathbf{M}_{ext} = \frac{d}{dt} (\mathbf{L}) = \frac{d}{dt} (\mathbf{L}' \mathbf{R}) =$$

$$\frac{d}{dt} (\mathbf{L}') \mathbf{R} + \mathbf{L}' \frac{d}{dt} (\mathbf{R}) = \frac{d}{dt} (\boldsymbol{\omega}') \mathbf{I}' \mathbf{R} + \boldsymbol{\omega}' \mathbf{I}' \frac{d}{dt} (\mathbf{R})$$

The (55) inference uses the well-known similarity transformation that rotates an arbitrary 3×3 matrix (in this case \mathbf{I}') using a rotation matrix \mathbf{R} and thus transforms the 3×3 matrix from body reference frame $O'x'y'z'$ to space reference frame $Oxyz$:

$$(57) \quad \mathbf{R}' \mathbf{I}' \mathbf{R} = \mathbf{I}$$

The matrix \mathbf{R}' is the transposed of \mathbf{R} . In (55) and (56) \mathbf{L} is the angular momentum vector in matrix form, $\boldsymbol{\omega}$ is the angular velocity vector in matrix form and \mathbf{M}_{ext} is the moment of external force vector in matrix form (one-row matrices). The 3×3 matrix \mathbf{I} is the moment of inertia tensor, which is invariant in the body reference frame for a given non-changing rigid body. \mathbf{I}' is defined as:

$$(58) \quad \mathbf{I}' = \begin{bmatrix} I'_{xx} & I'_{xy} & I'_{xz} \\ I'_{xy} & I'_{yy} & I'_{yz} \\ I'_{xz} & I'_{yz} & I'_{zz} \end{bmatrix} =$$

$$\iiint_{V'} \begin{bmatrix} r_z'^2 + r_y'^2 & -r_x' r_y' & -r_x' r_z' \\ -r_x' r_y' & r_x'^2 + r_z'^2 & -r_y' r_z' \\ -r_x' r_z' & -r_y' r_z' & r_x'^2 + r_y'^2 \end{bmatrix} \rho(x', y', z') dx' dy' dz'$$

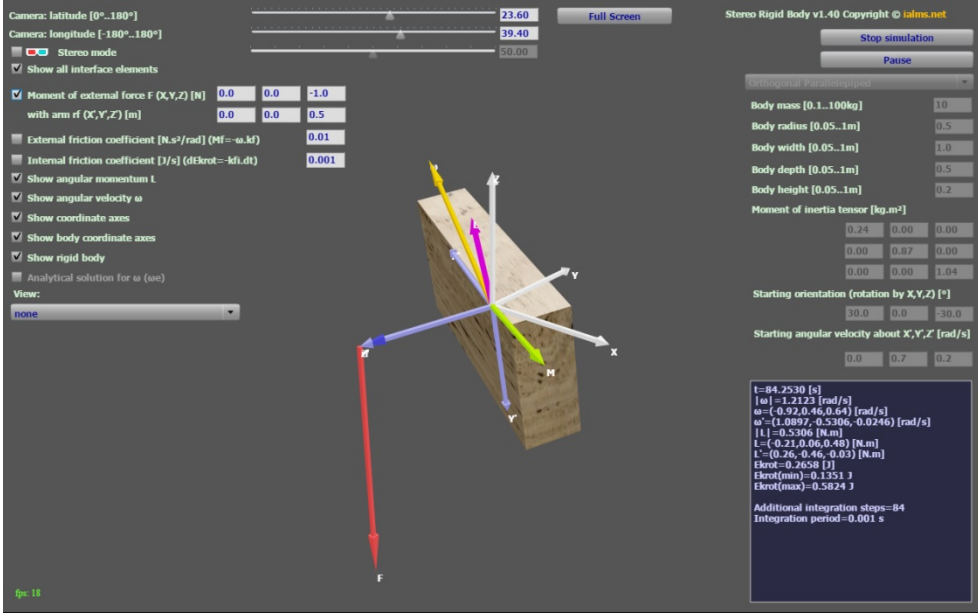


Fig. 4. Rigid body motion in a numerical 3D simulation

In (58) we observe that tensor \mathbb{I}' is a symmetric matrix. Vector $\begin{bmatrix} r_x' & r_y' & r_z' \end{bmatrix}$ is the radius-vector of the current infinitesimal point in the rigid body that is being integrated. Scalar function $\rho(x', y', z')$ gives the density of the rigid body at the current point of integration. The integration is performed over the volume V' of the rigid body. For an elaborate derivation of (58) please consult [22]. Further, \mathbb{I}' is a diagonal matrix if the body reference frame is chosen along the principal axis of inertia:

$$(59) \quad \mathbb{I}' = \begin{bmatrix} I'_{xx} & 0 & 0 \\ 0 & I'_{yy} & 0 \\ 0 & 0 & I'_{zz} \end{bmatrix} = const$$

Its inverse is also a diagonal matrix and has the simple form of

$$(60) \quad \mathbf{I}'^{-1} = \begin{bmatrix} I'_{xx}{}^{-1} & 0 & 0 \\ 0 & I'_{yy}{}^{-1} & 0 \\ 0 & 0 & I'_{zz}{}^{-1} \end{bmatrix} = \begin{bmatrix} 1/I'_{xx} & 0 & 0 \\ 0 & 1/I'_{yy} & 0 \\ 0 & 0 & 1/I'_{zz} \end{bmatrix} = const$$

Converting the rigid body motion equations into quaternion form requires the introduction of the Hadamard product of two quaternions:

$$(61) \quad \mathbf{a} \circ \mathbf{b} = (w_a w_b, x_a x_b, y_a y_b, z_a z_b)$$

The diagonal tensor \mathbf{I}' will be presented as a quaternion $\mathbf{I}' = (0, I'_{xx}, I'_{yy}, I'_{zz})$. Analogously, \mathbf{I}'^{-1} will be presented as $\mathbf{I}'^{-1} = (0, I'_{xx}{}^{-1}, I'_{yy}{}^{-1}, I'_{zz}{}^{-1})$. Now by transforming (55) and (56) to quaternion form we get:

$$(62) \quad \mathbf{L}' = \boldsymbol{\omega}' \mathbf{I}' \Rightarrow \mathbf{L}' = \boldsymbol{\omega}' \circ \mathbf{I}' \Rightarrow \boldsymbol{\omega}' = \mathbf{L}' \circ \mathbf{I}'^{-1}$$

$$(63) \quad \mathbf{M}_{ext} = \frac{d}{dt}(\mathbf{L}) \Rightarrow \\ \mathbf{M}_{ext} = \dot{\mathbf{L}} = \mathbf{q} \boldsymbol{\omega}' \mathbf{L}' \tilde{\mathbf{q}} + \mathbf{q} \dot{\mathbf{L}}' \tilde{\mathbf{q}} = \mathbf{q} \boldsymbol{\omega}' (\boldsymbol{\omega}' \circ \mathbf{I}') \tilde{\mathbf{q}} + \mathbf{q} (\dot{\boldsymbol{\omega}}' \circ \mathbf{I}') \tilde{\mathbf{q}}$$

$$(64) \quad \mathbf{M}'_{ext} = \tilde{\mathbf{q}} \mathbf{M}_{ext} \mathbf{q} = \boldsymbol{\omega}' (\boldsymbol{\omega}' \circ \mathbf{I}') + \dot{\boldsymbol{\omega}}' \circ \mathbf{I}'$$

A special case of rigid body motion is the free rigid body motion when the moment of external force is zero:

$$(65) \quad \mathbf{M}_{ext} = \dot{\mathbf{L}} = 0 \Rightarrow \mathbf{L} = \mathbf{q} \mathbf{L}' \tilde{\mathbf{q}} = \mathbf{q} (\boldsymbol{\omega}' \circ \mathbf{I}') \tilde{\mathbf{q}} = const$$

The second constant of free rigid body motion is the kinetic energy of rotation E_{Krot} :

$$(66) \quad E_{Krot} = -\frac{\text{Re}(\mathbf{L}\boldsymbol{\omega})}{2} = -\frac{\text{Re}(\mathbf{L}'\boldsymbol{\omega}')}{2} = -\frac{\text{Re}((\boldsymbol{\omega}' \circ \mathbf{I}')\boldsymbol{\omega}')}{2} = const$$

Quaternion numerical integration used in autopilots

The current orientation of the body reference frame (i.e. the aircraft airframe) in respect to the space reference frame is obtained by integrating the angular velocity vector. The latter is derived from the onboard gyroscope. The onboard gyroscope measures the angular velocity $\boldsymbol{\omega}'$ in regard to the body reference frame. Equation (39) comes in hand and it should be now numerically integrated:

$$(67) \quad \mathbf{q} = \mathbf{q}_0 + \int_0^{\Delta t} \dot{\mathbf{q}} dt$$

Different integration schemes may be implemented such as Euler, Runge-Kutta, etc. A symplectic method of integration is preferred as it preserves the rotational energy under conservative torque. Below an example is given with the symplectic semi-implicit Euler–Cromer integration method:

$$(68a) \quad \boldsymbol{\omega}'_{n+1} = \boldsymbol{\omega}'_n + \left(\tilde{\mathbf{q}}_n \mathbf{M}_{(ext)n} \mathbf{q}_n - \boldsymbol{\omega}'_n (\boldsymbol{\omega}'_n \circ \mathbf{I}') \right) \circ \mathbf{I}'^{-1} \Delta t$$

$$(68b) \quad \boldsymbol{\omega}'_{n+1} = \text{gyroscope_omega}(t_{n+1})$$

$$(68c) \quad \mathbf{q}_{n+1} = \mathbf{q}_n + \frac{1}{2} \mathbf{q}_n \boldsymbol{\omega}'_{n+1} \Delta t = \mathbf{q}_n \left(\mathbf{1} + \frac{\boldsymbol{\omega}'_{n+1} \Delta t}{2} \right)$$

Equation (68a) demonstrates the predicted angular velocity. The gyroscope read angular velocity is presented in (68b). Finally, the new orientation is calculated in (68c). The autopilot utilized algorithm selects between the predicted angular velocity according to the dynamic model and the gyroscope read angular velocity. Further corrections on the current position are carried out according to other autopilot sensors and procedures, which are not disclosed in (68).

In the above example the so called naive quaternion integration was implemented. A better approach is to integrate the quaternion over the hypersphere surface in the four dimensional quaternion space [23]. This four dimensional sphere has radius of 1 (see figure 5). The rotation quaternions \mathbf{q}_n and \mathbf{q}_{n+1} are unit quaternions and lie on the unit hypersphere. The natural method of integrating the rotation quaternion is to interpolate it over the hypersphere surface. The time change for one integration step of the rotation quaternion \mathbf{q}_n is $\dot{\mathbf{q}} \Delta t$. The latter quaternion is perpendicular to \mathbf{q}_n , but having non-infinitesimal length goes out of the hypersphere.

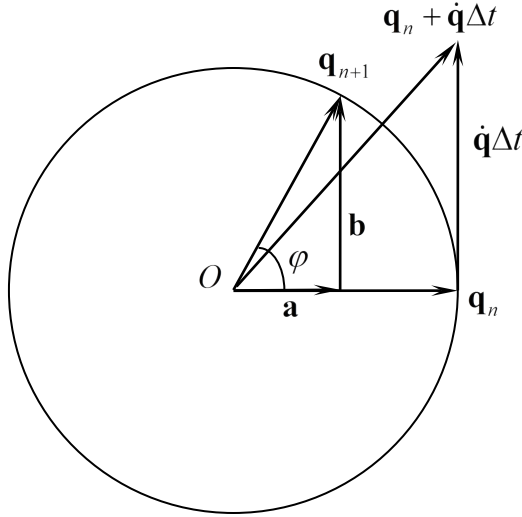


Fig. 5. Integrating the quaternion over the hypersphere surface

The new rotation quaternion $\mathbf{q}_{n+1} = \mathbf{q}_n + \dot{\mathbf{q}}\Delta t$ has magnitude > 1 . On the other hand the correct value for \mathbf{q}_{n+1} is a quaternion positioned on the hypersphere. It also lies on the two dimensional unit circle defined by \mathbf{q}_n and $\dot{\mathbf{q}}\Delta t$ (Fig. 5). The arc of the hypersphere between \mathbf{q}_n and \mathbf{q}_{n+1} has length $\varphi = |\dot{\mathbf{q}}|\Delta t$. It follows that

quaternion $\mathbf{b} = \frac{\dot{\mathbf{q}}}{|\dot{\mathbf{q}}|} \sin \varphi$ and quaternion $\mathbf{a} = \mathbf{q}_n \cos \varphi$. For \mathbf{q}_{n+1} we obtain:

$$(69) \quad \mathbf{q}_{n+1} = \mathbf{a} + \mathbf{b} = \mathbf{q}_n \cos \varphi + \frac{\dot{\mathbf{q}}}{|\dot{\mathbf{q}}|} \sin \varphi$$

Conclusion

The utilization of quaternions in autopilots has been a privilege to large and expensive aircraft till recently. The quaternion arithmetic computations are much faster and more accurate than other approaches, but require well written software libraries of significant complexity. The increased accuracy and flexibility of the quaternion method is a fruitful avenue for developing prototype, scientific and research autopilot systems. Furthermore, the modern unmanned helicopters do require custom made autopilots that can respond to their high specific needs. Such machine is the award winning *The Bulgarian Knight Dodecacopter*

that has an unique rotor arrangement and benefits from a custom and specialized accurate and fast autopilot, realized using the quaternion approach.

References

1. Pervin, E., J.A. Webb. Quaternions in Computer Vision and Robotics. Carnegie-Mellon University, 1992.
2. Foreman, D., C. Tournes, and Y. Shtessel. Integrated missile flight control using quaternions and Third-order sliding mode control. *IEEE 11th International Workshop on Variable Structure Systems (VSS)*, 2010, 370–375.
3. Mahony, R., V. Kumar, and P. Corke. Multirotor aerial vehicles: Modeling, estimation and control of quadrotor. *IEEE Robotics and Automation Magazine*, 2012, 19(3), 20–32.
4. Dam, E.B., M. Koch, and M. Lillholm. Quaternions, interpolation, and animation. Technical Report DIKU-TR-98/5, Department of Computer Science, University of Copenhagen, Denmark, 1998.
5. Goldman, R. Rethinking Quaternions: Theory and Computation. Morgan & Claypool Publishers, 2010. ISBN 978-1-60845-420-4.
6. Faugeras, O.D. and M. Hebert. The representation, recognition, and locating of 3-D objects. *International Journal of Robotics Research*, 1986, 5(3), 27–52.
7. Shoemake, K. Animating rotation with quaternion curves. *Computer Graphics*, 1985, 19(3), 245–254.
8. Zhao, F. and B.G.M. van Wachem. A novel quaternion integration approach for describing the behaviour of non-spherical particles. *Acta Mechanica*, 2013, 224, 3091–3109.
9. Horn, B.K.P. Closed-form solution of absolute orientation using unit quaternions. *Journal of Optical Society of America A*, 1987, 4(4), 629–642.
10. Shoemake, K. Quaternion calculus and fast animation. *SIGGRAPH Course Notes*, 1987, 10, 101–121.
11. Hamilton, W.R. On quaternions, or on a new system of imaginaries in algebra. *Philosophical Magazine*. 1844, 25(3), 489–495.
12. Gutmann-Madsen, T. Course notes for Mathematics IMA (calculus). Matematisk Notetryk, Institute of Mathematics, University of Copenhagen, Denmark, Copenhagen, 1991.
13. Hamilton, W.R. Lectures on Quaternions. Hodges Smith & Co., Dublin, 1853.
14. Hamilton, W.R. Elements of Quaternions, Vol. 1–2. Longmans, Green and Co., 1899.
15. Kuipers, J.B. Quaternions and rotation Sequences: a Primer with Applications to Orbits, Aerospace, and Virtual Reality, Princeton University Press, 1999. ISBN 978-0-691-10298-6
16. Chris, D., A.N. Lasenby. Geometric Algebra for Physicists. Cambridge University Press, 2003. ISBN 978-0-521-48022-2.
17. Maillot, P.-G. Using quaternions for coding 3D transformations. In: Andrew Glassner, editor, *Graphics Gems 1*, chapter 10, 498–515. Academic Press, Inc., 1990.
18. Omelyan, I.P. Algorithm for numerical integration of the rigid-body equations of motion, *Phys. Rev. E.*, 1998, 58(1), 1169.

19. Kim, M.-J., M.-S., Kim, and S.Y. Shin. A compact differential formula for the first derivative of a unit quaternion curve. *Journal of Visualization and Computer Animation*, 1996, 7(1), 43–57.
20. Xu, D., C. Jahanchahi, C.C. Took, and D.P. Mandic. Quaternion Derivatives: The GHR Calculus. *Royal Society Open Science*, 2015, 2(8), 150255.
21. van Waveren, J.M.P. From Quaternion to Matrix and Back, 27 February 2005, Id Software, Inc.
22. Zabunov, S., P. Getsov, and M. Gaydarova. Stabilization of Free Rigid Body Motion Stereo 3D Simulation through Invariants, *International Journal of Advanced Research in Computer Science*, 2014, 5(6), 9–16.
23. Jia, Y.-B. Quaternion and Rotation. *Com S*, 2013, 477(577), 15.

АВТОПИЛОТ ЗА ДВАНАДЕСЕТОКОПТЕРИ, БАЗИРАН ВЪРХУ КВАТЕРНИОНИ – ЧАСТ I

С. Забунов

Резюме

Иновациите в областта на модерните безпилотни летателни апарати поставят по-високи изисквания към автопилотите. Иновативните мулти-роторни хеликоптери, поради своята уникална система за контрол и разположение на роторите, изискват от автопилотите специални условия.

Настоящата статия представя ядрото на автопилот, който е базиран върху кватерниони. Този автопилот е подходящ за иновативния и спечелил международни награди дванадесет роторен безпилотен хеликоптер “Българският Рицар”. Кватернионите предлагат на автопилотните системи редица предимства. Тяхното приложение в специализираните автопилоти изисква изключително внимание и обсъждане. Като резултат се получава ефективен и гъвкав автопилот, защото кватернионните изчисления са много по-бързи и по-точни от другите конкурентни подходи, но такъв автопилот изисква сложни софтуерни библиотеки. Повишената точност и адаптивност на кватернионния метод го правят обещаващо средство за разработка на прототипни, научни и изследователски автопилотни системи, подходящи за специфичните нужди на иновативните дронове.

KU-BAND SMALL ANTENNA FOR SATELLITE EARTH STATIONS WITH IMPROVED RADIATION DIAGRAM

Peter Petkov¹, Elissaveta Alexandrova², Maxim Zayakov³

¹*Technical University, Sofia,*

²*Bulgarian Astronautical Society, Sofia*

³*“Bulgaria Sat” EAD, Sofia*

e-mail: e_alexandr@mail.bg

Abstract

The mechanical and electrical design characteristics of a small offset antenna with elliptical aperture for receiving earth stations intended for the 11.7÷12.5 GHz Broadcasting Satellite Service (BSS), with improved antenna radiation pattern in the plane of the geostationary satellite orbit (GSO), were presented in a previous article published in Aerospace Research in Bulgaria. The antenna was manufactured by “Bulgaria SAT” company and its parameters and antenna pattern were measured by the Technical University in Sofia. In this article are presented specific elements of the production process and measured antenna characteristics. The results from measurements show that the antenna characteristics make this antenna suitable for use not only for BSS emissions reception, but also as a VSAT transceiver antenna in a much wider frequency band. Measured antenna pattern in the two main planes and at both linear polarizations were used in support of the revision of the ITU-R Recommendation S.1717 and were submitted for inclusion in the databank associated to this recommendation.

1. Introduction

A design of a small offset antenna with an elliptical aperture 70×50 cm with improved radiation pattern was presented in [1] as an alternative of the reference radiation pattern for BSS receiving antennas in Recommendation ITU-R BO.1213 with 60 cm circular aperture and bandwidth of $\sim 3^\circ$ (2.86°) at a half power level. The last is an existing reference antenna radiation pattern intended for BSS receiving earth stations for Region 1 and 3 of the International Telecommunication Union, Sector ‘Radiocommunication’ (ITU-R) in the band 11.7÷12.5 GHz referred to Appendix 30 of the Radio Regulations (RR) of ITU-R [2]. It is the basis of the analyses for the identification of the need for coordination of the new submitted systems for additional use of the BSS band. The reference antenna pattern does not allow too close positions of satellites in the systems for additional use of the BSS band. However, given the numerous submissions, it becomes increasingly difficult to find a position at the geostationary orbit (GSO) for new BSS system, which can

be successfully coordinated under the provisions of Article 4 of Appendix 30 of the PP.

In 2012, "Bulgaria SAT" EAD was awarded by the national regulatory authority 'Commission for regulation in communications' (CRC) with permission to use GSO position 1.9°E for BSS system in case of a successful coordination. Both sides of this position the satellites of other countries' BSS systems in operation are positioned at $\sim 3^\circ$ away. This circumstance required to conduct research and develop a new construction antenna for BSS receiving stations with improved radiation pattern enabling achievement of greater side-lobe suppression in the off-axis angles $\sim 3^\circ$ from the axis of the antenna and better cross-polarization discrimination. Based on constructive and electrical design characteristics of BSS receiving antenna a new reference antenna pattern was proposed and adopted by the Study Group 4 as Recommendation ITU-R BO.2063 [3]. The "Bulgaria SAT" EAD set up manufacturing of the antenna based on the design parameters, as well as, measurements of the basic constructive and electrical parameters: gain cross-polarization discrimination, radiation patterns of the antenna in the two major planes - in azimuth plane with the geostationary orbit and in the vertical plain along the elevation of the antenna.

2. Constructive and electrical characteristics of the developed antenna

The proposed antenna design is based on paraboloid shape main reflector, cut out with an oval rim. The rim shape is selected in a way to introduce reduction in the main lobe of the antenna, with edge illumination kept in control for low sidelobes, while the antenna gain still see a minimal reduction. To achieve a proper edge illumination level for oval (not circularly symmetric rim) a special dual mode feed horn was developed. In general cases, a single mode horn combined with an elliptical aperture will be sufficient to provide edge illumination good enough for the low first side lobes. However the induced currents on the reflector will have a component, degrading the cross-polar pattern of the antenna. In order to suppress the cross-polar component and improve the cross-polar pattern and antenna performance over the frequency band of operation (10.7÷12.75 GHz), a second order circular mode (TM₁₁) is excited in the horn [4]. The phase relation between the modes is controlled with the proper selection of the horn length after the mode launcher and aperture flaring. The flaring causes excitation of additional high-order modes, however it was determined that their amplitudes are low enough to impair the horn pattern and particularly cross-polarization component level. Since the proposed antenna has an offset geometry it still has a rise of the cross-polar component levels in the Azimuth plane, but the proposed technique helps these levels to be kept within predefined maximum limits. For further reduction of the spillovers and improvement of the horn (primary) pattern a quarter-wave choke is introduced around the horn aperture. The prototype horn was precisely machined

out of aluminum block on a Computer Numerical Control machine. All these measures led to bore-sight cross-polar discrimination of around -45 dB across the whole band. Additional measurements were conducted on casted aluminum samples, and they show a slight degradation of the cross-polar performance to -35dB, which is still a satisfactory result for receive-only antenna as will completely exclude the probability of cross-polar interference on the received channel.

The prototype of the main reflector is milled out of large single piece aluminum block which lead to surface deviation of 0.05 mm RMS against the ideal parabolic shape. Such deviation will introduce 0.02 dB antenna gain reduction [5], [6], which is an insignificant value, comparable with the error of the measurement instrument. Additional antenna gain loss may occur due to imperfect surface roughness, however estimations are for 0.02÷0.05 dB (antenna surface was brushed). The prototype antenna will not count for the large surface deviations which occur in stamped regular production, due to material spring-back leading to undesired pattern deviations and side-lobe level increase.

3. Measurement of radiation patterns of the developed antenna

The measurements were performed on an open far-field antenna range. The distance between the source and the antenna under test was approximately 100 m. Measurements were carried out at frequencies 10.7 GHz, 11.725 and 12.75 GHz describing the entire Ku-band 10.7÷12.75 GHz used for broadcasting of DTH TV programs. The measurements are performed according to recommendations in IEEE Standard Test Procedures for Antennas (IEEE Std 149-1979), with spectrum analyzer externally locked to the source generator. All measurements are performed by azimuth rotation, but with the antenna rotated around the boresight direction in cardinal planes (0° and 90°). The measurements in each cut plane at a given frequency are conducted up to 100° from the antenna boresight and consist of 201 data points in accordance with Annex 2 of Recommendation ITU-R S.1717 [7] determining the format of electronic data for inclusion in the data bank of the ITU-R for the measured diagrams of antennas for earth stations. This format was proposed in [8] and adopted by WP4A [9]. The antenna gain measurement accuracy is assessed as better than 0.25 dB.

The four figures presented below show the measured radiation diagrams for vertical polarization in azimuth ($\varphi_k = 0^\circ$) co-polar (Fig. 1 and Fig. 2) and cross-polar (Fig. 3 and Fig. 4) planes at 10.7 GHz and 12.75 GHz of the antenna operating frequency band. For comparison are shown diagrams generated following the equations of the current reference pattern for BSS receiving antennas of Recommendation ITU-R BO.1213, included in Annex 5 of Appendix 30 of the RR [2] and equations of the developed as an alternative radiation pattern for BSS receiving antennas in Recommendation ITU-R BO.2063 [3] resulted from the

Bulgarian proposal [10]. It is clearly seen that the measured radiation diagrams of the developed antenna are better than the analytical:

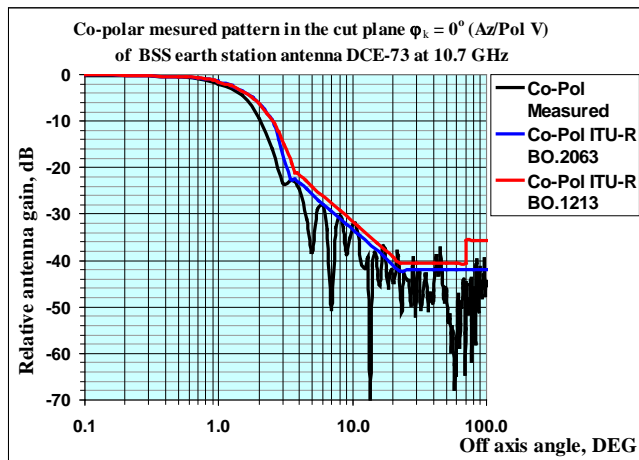


Fig. 1. Co-polar measured radiation diagrams for vertical polarization in azimuth ($\varphi_k = 0^\circ$) at 10.7 GHz

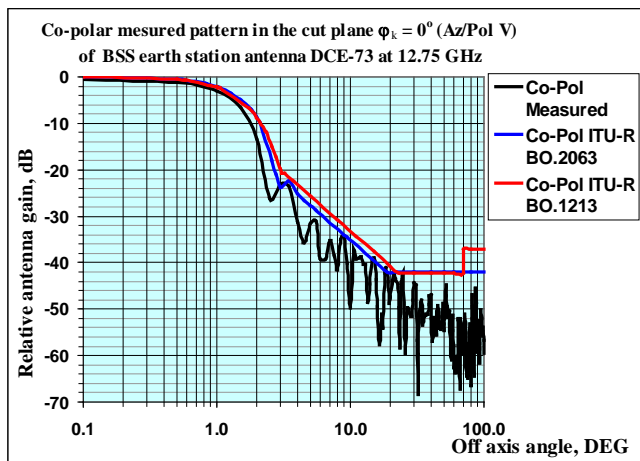


Fig. 2. Co-polar measured radiation diagrams for vertical polarization in azimuth ($\varphi_k = 0^\circ$) at 12.75 GHz

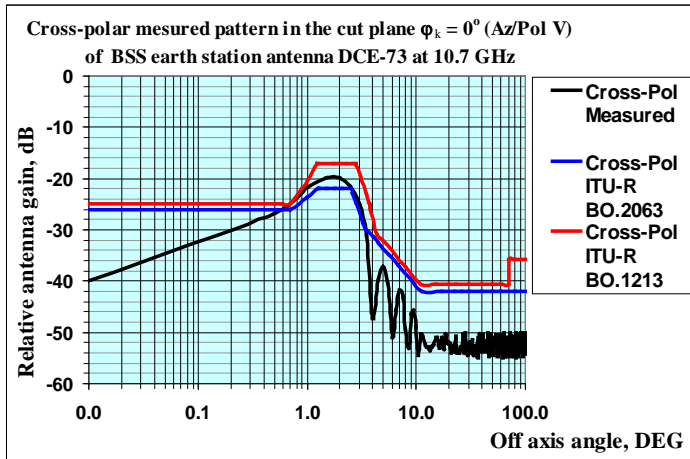


Fig. 3. Cross-polar measured radiation diagrams in $\varphi_k = 0^\circ$ (Az/Pol V) at 10.7 GHz

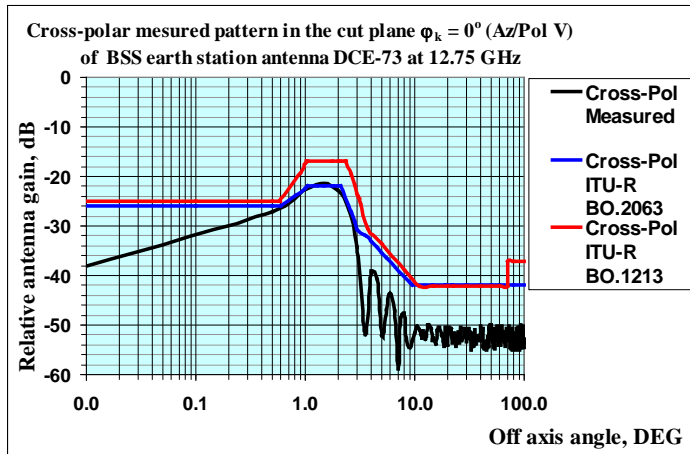


Fig. 4. Diagram of cross-polar measured radiation in $\varphi_k = 0^\circ$ (Az/Pol V) at 12.75 GHz

- co-polarization pattern (Fig. 1 and Fig. 2), especially in the off-axis antenna angles $1.5^\circ \div 3^\circ$, which are essential for the operation of satellite systems at close positions of the satellites on GSO;
- cross-polarization pattern (Fig. 3 and Fig. 4) providing better cross-polarization discrimination, which allows reception of co-frequency channels at both polarizations, i.e. developed antenna contributes to a more efficient use of the frequency-orbital resources in the frequency bands for broadcasting-satellite service.

In Fig. 5 is presented a comparison between the co-polar gain of the developed antenna DCE-73 at the middle frequency 11.725 GHz, at which measurements are also made, and the gain for the corresponding off-axis angles calculated using equations for the radiation diagram in Recommendation ITU-R BO.2063 [3] for 0.6 m antenna size, as well as, a comparison between the antenna gain based of this recommendation and Recommendation ITU-R BO.1213, which was adopted as a reference diagram for the planned BSS band [2]. From the curves shape it is evident that the equations in Recommendation ITU-R BO.2063 provide greater side-lobe gain suppression within the scope of the most important off-axis angles for effective use of GSO and BSS spectrum than that according the equations in Recommendation ITU-R BO.1213. The radiation pattern of the real antenna provides significantly greater side-lobe gain suppression than the analytical ones in both recommendations, especially in the off-axis angle sector $2^{\circ} \div 3^{\circ}$.

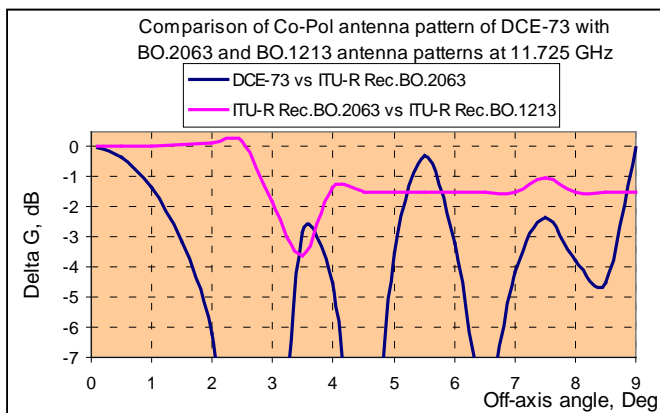


Fig. 5

3. Evaluation of the results from using the developed antenna

In order to establish the effect of using more effective radiation pattern of Recommendation ITU-R BO.2063 developed based on the design parameters of the antenna of "Bulgaria SAT" EAD, the excess of the criterion „Max. EPM Degradation ≤ 0.45 dB” is analyzed. The results of this analysis are used by the ITU-R Radiocommunication Bureau to establish the need for coordination of newly submitted BSS satellite system with submitted before it systems in the planned BSS band. The software MSPACEg of the ITU-R Radiocommunication Bureau, designed for this purpose, is used. The analyzes are made for the reference diagram of Recommendation ITU-R BO.1213 for BSS receiving antennas of the test systems as applied to the ITU-R Radiocommunication Bureau and for the radiation pattern of Recommendation ITU-R BO.2063. A sample of the results from analyzes, in a form of outputs from MSPACEg, are presented in

Attachment 1. In green are marked all systems, groups of emissions, and BSS channels dropped out as potentially affected by newly submitted BSS system as a result of application of the radiation pattern of Recommendation ITU-R BO.2063: 4 systems, 25 groups of emissions, and 21 BSS channels from the great groups of emissions. As a newly submitted system the Bulgarian submission from 2012 in the planning BSS band 11.7÷12.5 GHz at position 1.9° is used.

From the comparisons presented in Fig. 5, it is obvious that the use of the developed antenna DCE-73 as receiving BSS antenna will minimize interference in real conditions, since the distance between the positions of the affected systems and the Bulgarian system are exactly in the off-axis angle sector 2°÷3°. In this angular sector differences in the real antenna gain and the calculated ones according to Recommendation ITU-R BO.2063 is more than 5 dB in favor of the real antenna.

5. Conclusion

Through the development of the BSS receiving antenna (Fig. 6) from "Bulgaria SAT" EAD the following results were achieved:

1. Based on the design data of the developed BSS receiving antenna, presented in [1], [10] and other contributions, a new Recommendation ITU-R BO.2063 [3] were proposed and adopted following the ITU-R procedures as an alternative of the existing reference pattern for BSS receiving antennas [2] taken from Recommendation ITU-R BO.1213;

2. The measurement data of the radiation patterns of "Bulgaria SAT" EAD BSS receiving antenna for both polarizations in two orthogonal planes allowed to finalize the proposed revision of Recommendation ITU-R S.1717 by inclusion of actual data for all components in its new Annex 2 [7];

3. Measurement data of the developed by "Bulgaria SAT" BSS receiving antenna with improved radiation pattern presented in the format of Annex 2 to Recommendation ITU-R S.1717 were included in the data bank to this recommendation [8, 9].



Fig. 6 "Bulgaria SAT" BSS receiving antenna

The following conclusions can be made:

1. The measurement data of the radiation pattern of the developed from "Bulgaria CAT" BSS receiving antenna shows that it is possible to develop a BSS receiving antenna with the aperture, equivalent to 0.6 m antenna with a circular aperture, with an improved radiation pattern complying with Recommendation ITU-R BO.2063 [4], developed based on the design parameters of this antenna, which confirms that the Recommendation ITU-R BO.2063 is feasible and can be proposed to replace the existing in the RR reference radiation pattern for BSS receiving antennas [3]. This would result in the identification of less number of potentially affected systems and will facilitate the coordination process and consequently will lead to more effective use of frequency-orbital resources;

2. The use of the developed antenna (DCE-73) as a BSS receiving antenna will allow closer spacing of BSS satellite systems and thus will lead to extremely improve under real conditions the use of frequency-orbital resources in one of the most overloaded bands for distribution of satellite TV programs.

References

1. Petkov, P., E. Alexandrova. New Construction KU-Band Antenna with Improved Radiation Diagram for Satellite Broadcasting Receiving Earth Station. Aerospace Research in Bulgaria, 2013, 25, 228–238. ISSN 1313-0927.
2. Annex 5 to Appendix 30 of the Radio Regulations, 2012.
3. Recommendation ITU-R BO.2063 (09/2014), Alternative BSS earth station antenna radiation pattern for 12 GHz BSS bands with effective apertures in the range 55–75 cm, Geneva, 2014.
4. Potter, P. D. A New Horn Antenna with Suppressed Sidelobes and Equal Beamwidths, Microwave Journal, 1963, 71–78. (reprinted in A.W. Love, Electromagnetic Horn Antennas, IEEE, 1976, 195–202.)
5. Ruze, J. Antenna tolerance theory-a review, Proceedings of the IEEE, vol. 54, pp. 633–640, 1966.
6. Ruze, J. The effect of aperture errors on the antenna radiation pattern, Il Nuovo Cimento, 1952, 9(3), 364–380.
7. Recommendation ITU-R S.1717 (09/2015), Electronic data file format for earth station antenna patterns, Geneva, 2015.
8. Document 4A/624, 20 June 2015, Bulgaria (Republic of), Study of the applicability of the FSS earth station antenna reference patterns to small earth station antennas, (Geneva, 17-25 June 2015).
9. Document 4A/669, 14 July 2015, Chairman, Working Party 4A, Report on the meeting of Working Party 4A, (Geneva, 17-25 June 2015).
10. Document 4A/548, 26 June 2014, Bulgaria (Republic of), Measurements of new design BSS receiving antenna and conclusions on PDRR ITU-R D.1717 and DNR BO.[ALT_BSS_ANT_DIAG], (Geneva, 02-10.07.2014).

Input File Name: C:\BRIFICS\IFIC-2809_08.12.2015\S_IFIC2809\Databases\AP30_30A\SPS_ALL_IFIC2809.mdb
 Output Database Name: C:\BRIFICS\IFIC-2809_08.12.2015\S_IFIC2809\Databases\AP30_30A\SPS_ALL_IFIC2809.OUT.MDB
 Date/Time of Creation: 12/31/2015 5:16:47 AM
 Version of Analysis: 16
 MSPACe software version: 7.5.0.0
 EPM degradation limit = 0.45 dB
 Co-polar orbital separation limit = 9.00 Cross-polar orbital separation limit = 9.00 (degrees)
 All Networks/Assignments from Input File or SNS/SPS Database Were Considered in Analysis

Adm. Symbol	Orbital Position (Deg, E)	Sat.Network Id.	Sat.Network Beam Name	Program Beam Name	Affected Channels	Max. EPM Degradation with BO.1213 (dB)	Max. EPM Degradation with BO.2063 (dB)
BUL	-1.20	BUL02000	BUL02000	BUL02000	22,24,26,28,30,32,34,36,38,40	4.397	2.091
GRC	-1.20	GRC10500	GRC10500	GRC10500	2,6,8,10,12,14,16,18	2.416	0.7
NOR	-0.80	NOR12100	NOR12100	NOR12100	28	7.578	6.087
S	5.00	S_13800	S_13800	S_13800	27,29,31,33,35,37,39	4.885	1.975
S	5.00	S_13900	S_13900	S_13900	30	3.072	<0.45
S	5.00	SIRIUS-2-BSS	NOR2	SI2ADN2A	20	1.986	<0.45
S	5.00	SIRIUS-2-BSS	NOR2	SI2ADN2D	20	1.958	<0.45
S	5.00	SIRIUS-2-BSS	NOR2	SI2DN2A	24,30,32,38,40	6.046	3.233
S	5.00	SIRIUS-2-BSS	NOR2	SI2DN2D	24,30,32,38,40	5.951	3.149
S	5.00	SIRIUS-2-BSS	NOR3	SI2DN3A	28,34,36	5.995	3.200
S	5.00	SIRIUS-2-BSS	NOR3	SI2DN3D	28,34,36	5.898	3.114
S	5.00	SIRIUS-2-BSS	STR2	SI2ADS2A	19	2.129	<0.45
S	5.00	SIRIUS-2-BSS	STR2	SI2ADS2D	19	2.108	<0.45
S	5.00	SIRIUS-2-BSS	STR3	SI2ADS3A	3,21	2.487	<0.45
S	5.00	SIRIUS-2-BSS	STR3	SI2ADS3D	3,21	2.415	<0.45
S	5.00	SIRIUS-2-BSS	STR1	SI2DS1A	27,35	7.962	4.920
S	5.00	SIRIUS-2-BSS	STR1	SI2DS1D	27,35	7.962	4.920
S	5.00	SIRIUS-2-BSS	STR2	SI2DS2A	29,31,33,37,39	7.962	4.920
S	5.00	SIRIUS-2-BSS	STR2	SI2DS2D	29,31,33,37,39	7.962	4.920
S	5.00	SIRIUS-2-BSS	STR3	SI2DS3A	1,23,25	2.795	<0.45

Page / pagina 1/6

МАЛКА АНТЕНА ЗА ЗЕМНИ СТАНЦИИ ЗА ВРЪЗКА СЪС СПЪТНИЦИ В КУ-ОБХВАТА С ПОДОБРЕНА ДИАГРАМА НА ИЗЛЪЧВАНЕ

П. Петков, Е. Александрова, М. Заяков

Резюме

В [1] са представени проектираните механични и електрически характеристики на малка антена с изместена фокална ос с елиптична апертура, предназначена за приемни земни станции за спътниково-радиоразпръскване (BSS) в обхвата 11.7÷12.5 GHz, с подобрена диаграма на излъчване в равнината на геостационарната орбита (GSO). Антената е разработена от „България САТ“ ЕАД и параметрите ѝ и диаграмата ѝ са измерени от Техническия университет в гр. София. В настоящата статия са представени специфични елементи на производствения процес и измерените характеристики на антената. Резултатите от измерванията показват, че антенните характеристики позволяват тя да бъде използвана не само за приемане на BSS излъчвания, но също и като предавателна VSAT антена в доста по-широк честотен обхват. Измерената диаграма на антената в двете главни равнини и на двете линейни поляризации са използвани за целите на ревизиране на Препоръка ITU-R S.1717 и са подадени за включване в банката данни, свързана с тази препоръка [10].

A RECTANGULAR UNIPOLAR PULSE WIDTH MEASUREMENT BY MEANS OF PIC18F2550 MCU

Konstantin Metodiev

*Space Research and Technology Institute – Bulgarian Academy of Sciences
e-mail: komet@space.bas.bg*

Abstract

The article examines an approach towards pulse width measurement by means of PIC18F2550 microcontroller unit (MCU). The proposed solution may come into use in process automation where the MCU decides in virtue of the measured quantity, for instance in case of a pulse with modulation. By way of illustration, it is possible to install the MCU on-board an unmanned aerial vehicle (UAV). In this case, the MCU reads a PWM input signal fed by the radio receiver and actuate a terminal mechanism afterwards depending upon the measured duty cycle value.

Special attention is given to the MCU software peculiarities. Additional computer simulation has also been made. The used software was MikroC Pro for PIC and Proteus VMS. The proposed solution has been shown to operate with sufficient precision. The source code is also included in the present article.

1. Introduction

Microcontrollers units (MCU) are vastly useful nowadays. Among many features supported, the ability of MCU to capture edges of a rectangular signal is applicable to many solutions. Should an edge happen to be registered, the MCU generates external interrupt and an interrupt service routine (ISR) is triggered afterwards. Because of this, the MCU no longer has to wait and check whether new impulse has arrived which is the major drawback of the so-called ‘polling approach’ [1]. Having that said, the possibility of counting time between consecutive rising and falling edges seems feasible.

The main purpose of the present article is to demonstrate the ability of such a simple solution to measure the pulse width automatically, see fig. 1, and then set in motion either a terminal mechanism or a circuit. Consider the emergency parachute on-board the LHK-3M unmanned aerial vehicle (UAV) as an example. By default, the chute is locked by a servo motor. The MCU might be connected parallel to the PWM wire as a sniffer. If a duty cycle value set in advance occurs, this means that the chute has been released. Then the MCU shuts the engine off by triggering a common emitter amplifier (bipolar transistor) and a relay.

2. Materials and methods

The electronic circuit consists of minimum required parts that make the MCU running according to Fig. 2, i.e. a high speed crystal of 20 MHz and two capacitors of 15 pF each. These are said to provide the MCU with stable instruction clock of 5 MHz [2].

The program algorithm is easy to understand. The MCU is initially set to expect a rising edge of the signal. Should this edge occurs, an external interrupt is triggered and the interrupt flag is switched on by the hardware. It is developer's responsibility to clear this flag each time when it is necessary otherwise it would be impossible for the MCU to trigger another interrupt. Having had the rising edge detected, the program code sets the interrupt flag off, starts an internal timer, and then adjusts the corresponding register so as to expect falling edge of the signal. In case of falling edge arrival, the interrupt flag is cleared again, the timer is stopped, and the program is set to expect the next rising edge. The timer value is converted into milliseconds and then it is cleared.

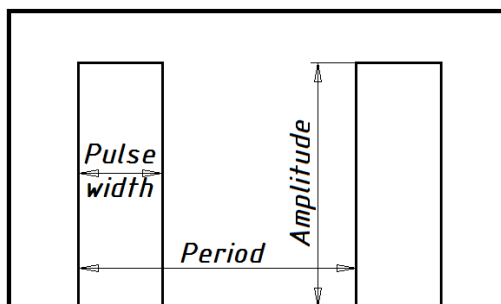


Fig. 1. Basic rectangular pulse definitions used in the article

On the other hand, the source code is a bit more complicated. It is published in the appendix section in the present paper. The code starts with setting port B as digital output and disabling the analog comparator. The former action is solely necessary if the application is to display results on a liquid crystal display (LCD). What follows is a function setting the capture ability of the MCU (see 'configureCapture' function in Appendix). For the present study, one out of two available Capture-Compare-PWM modules has been chosen, i.e. the CCP1. The external impulse is fed to RC2 pin which is why this pin is set as input.

The capture mode is initialized by setting the CCP1CON register. The most significant four bits remain unused in capture mode. The least significant four bits CCP1M<3:0> are set to 0b0101 so that the MCU expects the rising edge. Then, the Timer3 module is picked as a counter. It consists of two eight-bit registers TMR3H and TMR3L. Their values are eventually concatenated to obtain the pulse

width. As a matter of fact, in capture mode, two timers are available: Timer1 and Timer3. Neither of them should be chosen in preference to the other because both offer same input clock prescale values. These are set in corresponding control registers. In the present case study, the chosen prescale value for Timer3 is 1:8 which value is selected by setting the T3CON register accordingly [2]. What follows next is enabling the capture (CCP1IE_bit), peripheral (PEIE_bit), and global (GIE_bit) interrupts. Setting these bits is obligatory so that the ISR may happen. At the end of initialization function, Timer3 and CCP1 storage registers are cleared understandably. In addition, the Timer3 enabling bit (TMR3ON_bit) is set at zero for security reasons.

The ISR (see ‘checkExternalInterrupt’ function in Appendix) is triggered by the impulse rising edge first in accordance with what is written in the initialization function. If interrupt occurs, hardware sets the CCP1IF bit to 1. As it was mentioned earlier, it is mandatory for this bit to be cleared in the ISR. The next part of the function relies on the developer’s resourcefulness. An integer counter variable lets the MCU tell the upcoming edge apart, i.e. whether the edge is rising or falling. The counter solely gets two values, i.e. either 1 or 2. Each time the interrupt has been triggered, the counter is augmented by 1, yet it is cleared after the falling edge. If the counter equals to 1, it is the rising edge coming. This is the right moment to switch the Timer3 module on and set the CCP1M<3:0> bits to 0b0100 so that the MCU no longer looks for the rising edge but the falling. If the counter equals to 2, the falling edge is said to arrive, the CCP1M<3:0> bits are reverted to rising edge, and Timer3 is stopped. Also, a flag is set in order to indicate that Timer3 store registers contain the pulse width. When the capture mode is changed, a false capture interrupt may be generated [2]. The developer has to clear the CCP1IF bit once again. This is a special feature solely observable in the discussed MCU. The reader is referred to ‘if condition’ in ‘checkExternalInterrupt’ function, Appendix section.

The pulse width is further converted to seconds in ‘get_timer3_capture’ function. The function is indispensable because Timer3 module solely stores integers between 0 and 65535. Thus, the pulse width duration is obtained in accordance with following formula:

$$T_{pulse} = (CCPR1H \ll 8 + CCPR1L) * \frac{1}{\frac{F_{osc}}{4} Prescaler}, [s]$$

where Prescaler = 1/8, Fosc/4 = 5E+06 is instruction clock and CCPR1 register stores a copy of TMR3 register value. In the end of the function both TMR3 and CCPR1 registers has to be cleared so that a new count may begin. The obtained result unit is seconds. It is wise to remind that both counter and flag variables must be cleared after each falling pulse edge.

3. Results

The proposed circuit has been put to the test as follows. A sequence of rectangular pulses with frequency 50 Hz and pulse duration 1.75 ms enters the CCP1 pin. The obtained results after simulation by means of Proteus VMS are visible in Fig. 2. On the upper left side of the figure is shown a dialog panel for adjustment the input signal parameters. On the bottom side, the result is written down onto a LCD. Both values (1.75 ms) coincide in practice.

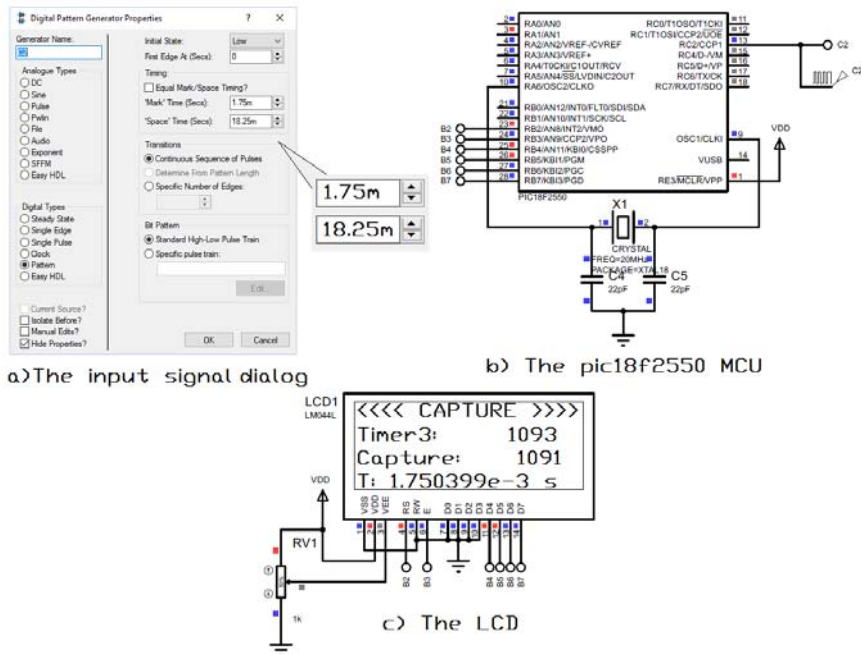


Fig. 2. Project simulation in Proteus VMS

4. Discussion

The proposed test case resembles a PWM signal which is widely used in remotely controlled vehicles for hobbyists. The MCU successfully measures the pulse width. The result is visible on the LCD in Fig. 2 and shows that the error is less than 1 %. This error may grow bigger however if the timer resolution get low. It is highly up to the program developer to decide. Nevertheless, the proposed solution might be used onboard an UAV as an actuator apart from standard articles sold off-the-shelf in hobby RC stores.

In addition, this article might be found useful by developers who are less experienced in the interrupt technique.

References

1. <http://www.electronics-base.com/useful-info/software-related/90-polling-vs-interrupt>
2. PIC18F2455/2550/4455/4550 Data Sheet, Microchip Technology Inc., 2006.

Appendix: Source code, MikroC Pro for PIC v.6.6.3

```
unsigned int timer3_register; // stores timer3 register value
unsigned int capture_register; // stores capture register value
float period; // stores the periodic
time
unsigned short counter = 0; // edge counter (rising and
falling)
bit flag = 0; // if two edges are detected, frequency & period might
be calculated

void cofigureCapture(void) {
    TRISC.F2 = 1; // input pin
    // Capture mode, every rising edge; 1 - rising edge; 0 -
falling edge
    CCP1M3_bit = 0; CCP1M2_bit = 1; CCP1M1_bit = 0; CCP1M0_bit =
1;
    // Pick up Timer3 as a resource
    T3CCP2_bit = 1; T3CCP1_bit = 1;
    // prescaler 1:8
    T3CKPS1_bit = 1;
    T3CKPS0_bit = 1;
    CCP1IE_bit = 1; // enable capture interrupt
    // enable all interrupts
    PEIE_bit = 1;
    GIE_bit = 1;
    // reset high & low bytes of timer3 & capture registers
    TMR3H = 0; TMR3L = 0;
    CCP1H = 0; CCP1L = 0;
    TMR3ON_bit = 0;
    flag = 0; // might be omitted
    return;
}

void get_timer3_capture(void) {
    //get high & low bytes of timer3 & capture registers
    timer3_register = (TMR3H<<8) + TMR3L;
    capture_register = (CCP1H<<8) + CCP1L;
    //calculate period
    period = (float)(capture_register + 1);
    period = (float)period * (4);
    period = (float)period * 1/20000000;
    period = (float)period * 8;
    //reset timer3 & capture & period
    TMR3H = 0; TMR3L = 0;
    CCP1H = 0; CCP1L = 0;
}
```

```

        return;
    }
void checkExternalInterrupt(void) {
    if (CCP1IF_bit == 1) { // if capture interrupt occurred
        (rising edge detected)
        CCP1IF_bit = 0; // reset capture interrupt flag
        TMR3ON_bit = 0; // stop timer1
        counter++; // counter increment by 1
        if (counter == 1) { // if cnt = 1 then rising edge
            has been detected
                TMR3ON_bit = 1; // timer3 start counting
                // look for falling edge
// CCP1M3_bit = 0; CCP1M2_bit = 1; CCP1M1_bit = 0;
                CCP1M0_bit = 0;
                CCP1IF_bit = 0; // obligatory for pic18f2550
only
                } // if
                if (counter == 2) { // if cnt = 2 then falling edge
                    has been detected
                        TMR3ON_bit = 0; // stop timer3
                        flag = 1; // set this flag to indicate that
                        pulse duration has been counted
                        // look for rising edge
// CCP1M3_bit = 0; CCP1M2_bit = 1; CCP1M1_bit = 0;
                        CCP1M0_bit = 1;
                        CCP1IF_bit = 0; // obligatory for pic18f2550 only
                } // if
            } // if
        return;
    }
}

void interrupt(void) { checkExternalInterrupt(); }

void capturePulseWidth(void) {
    if (flag == 1) { // if pulse duration has been
        counted
            get_timer3_capture(); // go and get results
            counter = 0; // then reset rising edge
        counter
            flag = 0; // also reset this flag
        } // if
    return;
}

void main(void) {
    TRISB = 0; // all output
    CMCON = 0x07; // disable comparators
    ADCON1 = 0b00001111; ADCON0 = 0b00101100; // all digital
    cofigureCapture();
    while(1) { capturePulseWidth(); }
    return; }

```


ИЗМЕРВАНЕ НА ШИРОЧИНАТА НА ПРАВОЪГЪЛЕН ЕДНОПОЛЯРЕН ИМПУЛС С ПОМОЩТА НА МИКРОКОНТРОЛЕР PIC18F2550

К. Методиев

Резюме

В настоящия доклад се разглежда подход за измерване на широчината на правоъгълен импулс чрез микроконтролер PIC18F2550. Предложеното решение може да се използва в автоматизиран процес, където микроконтролерът взема решение въз основа на измерената величина, например при широчинноимпулсна модулация. Възможно е устройството да се инсталира на борда на безпилотен летателен апарат. В случая контролерът чете широчинноимпулсно модулиран сигнал, подаван на входа от радиоприемника и въз основа на измерения коефициент на запълване задейства изпълнителен механизъм.

Специално внимание е отделено на особеностите на програмата за микроконтролера. Допълнително е направена компютърна симулация. Използваният софтуер е MikroC Pro for PIC и Proteus VMS. Показано е, че предложеното решение функционира със задоволителна точност. Кодът на програмата също е публикуван в настоящия доклад.

DOSIMETRY SCIENCE PAYLOADS FOR EXOMARS TGO & SURFACE PLATFORM. UNIFIED WEB-BASED DATABASE WITH LIULIN TYPE INSTRUMENTS' COSMIC RADIATION DATA (“DOSIMETRY”)*

DOSIMETRY is a complex project (URL: <http://esa-pro.space.bas.bg/>), combining investigations of space radiation environment, development of new instrumentation for space radiation measurements, and creating a database with Bulgarian cosmic radiation data obtained in different space missions from 1988 till nowadays.

The impact of the project objectives is in the area of Space Science, Human Spaceflight and Exploration, Robotic Space Exploration. The project is under realization in the Space Research and Technology Institute at the Bulgarian Academy of Science (SRTI-BAS).

ExoMars is a joint ESA-Roscosmos programme for investigating Mars (URL: <http://exploration.esa.int/mars/46048-programme-overview>). Two missions are foreseen within this programme: one consisting of the Trace Gas Orbiter (TGO), plus an Entry, Descent and landing demonstrator Module (EDM), launched on 14 March 2016; and the other, featuring a rover and a surface platform, with a launch date of 2020. The SRTI-BAS participates in both missions with experiments for investigation of the space radiation environment, conducted by dosimeters of *Liulin*-type instruments. The experiment *Liulin-MO* for measuring the radiation environment onboard the ExoMars 2016 TGO is a part of the Russian Fine Resolution Epithermal Neutron Detector (FREND) onboard TGO. The second envisaged experiment is *Liulin-ML* experiment for investigation of the radiation environment on Mars surface. The experiment will be conducted with the *Liulin-ML* dosimeter as a module of the Russian active detector of neutrons and gamma rays (ADRON-EM) on the surface platform of ExoMars 2020 mission. The objectives of DOSIMETRY are:

1. Development, manufacture, and testing in relevant environments of the dosimeter *Liulin-ML* of ADRON-EM instrument of ExoMars 2020 surface platform science payload;
2. Flight operations and handling the data of the dosimeter *Liulin-MO* of FREND instrument on ExoMars 2016 TGO. The dosimeter *Liulin-MO* of FREND instrument for ExoMars TGO has been developed and manufactured in SRTI-BAS under contracts with Space Research Institute (SRI-Moscow); FREND including its dosimeter *Liulin-MO* has been launched aboard ExoMars TGO on 14 March 2016. Presently TGO is in orbit around Mars.

3. Development of unified, web-based database with *Liulin* data

The objective is to develop a web-based database with the *Liulin* type instruments data sets from *Mir* space station, International Space Station, BION, Photon, and Chandrayan-1 satellites and to add *Liulin-MO* ExoMars TGO data to the database.

The geometrical mass and thermal equivalent models of *Liulin-ML* have been already developed and tested at SRTI-BAS. The external view of *Liulin-ML* is shown in Fig. 1.

During main part of TGO cruise to Mars the *Liulin-MO* was turned on. The average dose rate in Si in the interplanetary space is 372 ± 30 mGy d⁻¹ and 390 ± 31 mGy d⁻¹; the average flux is 3.12 cm⁻² s⁻¹ and 3.29 cm⁻² s⁻¹ in two perpendicular directions.

The average measured dose rate from 01.11.2016 till 18.01.2017 in high elliptic Mars' orbit is respectively 405.6 ± 41 μGy d⁻¹ and 422.4 ± 42 μGy d⁻¹, the particle flux is 3.3 and 3.4 cm⁻² s⁻¹. The particle fluxes in high elliptic Mars orbit from 01.11.2016 to 04.01.2017 and comparison with SIS instrument on ACE satellite (URL: <https://helios.gsfc.nasa.gov/ace/sis.html>) are shown in Fig. 2.



Fig. 1. External view of *Liulin-ML* dosimeter

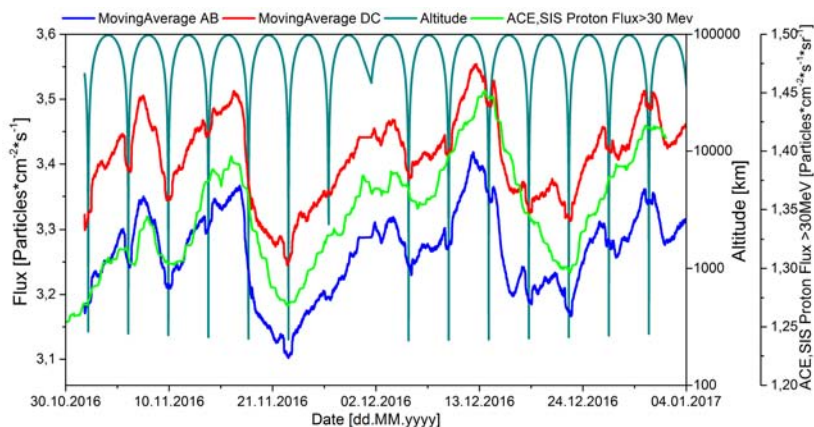



Fig. 2. Particle flux in the perpendicular detectors of *Liulin-MO*. Comparison with the proton flux of SIS instrument on ACE satellite. SIS data is shifted back by 4 days.

*  The Project is funded by the Government of Bulgaria through an ESA Contract 4000117692/16/NL/NDe under the PECS (Plan for European Cooperating States). The view expressed herein can in no way be taken to reflect the official opinion of the European Space Agency

TESTING SENTINEL-2 VEGETATION INDICES FOR THE ASSESSMENT OF THE STATE OF WINTER CROPS IN BULGARIA (TS2AGROBG)*



The *TS2AgroBG* project is motivated by the idea that the Bulgarian agriculture sector can benefit significantly from the wider application of remote sensing technology. While aerial photographs have been used in this sector for a decade for agricultural parcels identification, the full potential of satellite applications for crop growth assessment and crop mapping is to be further explored.

The innovative Sentinel-2 satellite mission, of the European Commission's *Copernicus* programme, will expand the possibilities by providing free imagery with high spectral and spatial resolution suitable for crop state monitoring at field level. In addition to that, the PROBA-V acquires 100 m spatial resolution satellite data at high temporal frequency enabling crop mapping based on image time series. In this context, it is an opportunity to raise awareness of Bulgarian policy makers and other agricultural stakeholders for the capability of these advanced contemporary technologies. This project could also promote the development of applications and services for this emerging market in Bulgaria.

For effective crop management it is important to have timely information about the distribution and areas of different crops and about their growth status and potential yield. To acquire this information, satellite imagery from Sentinel-2 and PROBA-V seems to be of great benefit. In this project, data from these two satellites will be used to generate agriculture-relevant products, including: raster layers with crop biophysical variables, crop state assessment maps, crop masks, and national crop map. Because this is a pilot study, the project will focus on the most important winter crop in Bulgaria – winter wheat. In addition to the common bio-physical variables like Leaf Area Index (LAI), fraction of Absorbed Photosynthetically Active Radiation (fAPAR) and Canopy Chlorophyll Content (CCC), the project will investigate the possibility to retrieve total nitrogen (N) content, fresh and dry above ground biomass (AGBf and AGBd), and fraction vegetation cover (fCover) from Sentinel-2 data. Vegetation indices calculated from Sentinel-2 data will be used to develop empirical regression models for computation of biophysical variables. Dedicated field campaigns will be conducted to obtain consistent ground-truth dataset for the regression models' calibration and validation. The Institute of Soil Science, Agrotechnologies and Plant Protection "Nikola Poushkarov" will provide valuable support during the field campaigns and laboratory analyses of plant samples. Based on these bio-physical variables a crop

state assessment map will be generated. Other type of product will be the crop mask, which will be developed by the Belgian project partner – VITO. To facilitate the generation of crop masks in operational context an extension of the software SPIRITS is proposed to handle and process Sentinel-2 data. In addition, a sub-pixel crop map at national level will be produced through classification of PROBA-V 100 m time series data. Classifications of Sentinel-2 imagery over two training/test areas will be used to calibrate the national level PROBA-V classification. Finally, the possibility to improve the winter wheat yield prediction based on crop-growth model and Sentinel-2 derived biophysical variables will be examined.

The main objectives for the project are to:

1. Accomplish series of field campaigns in a selected test site and to provide geo-database containing ground measured biophysical variables and semi-synchronous remote sensing imagery;
2. Calibrate and validate regression models for retrieval of different biophysical variables using Sentinel-2 vegetation indices applicable to winter wheat grown in Bulgaria; making use of this information to generate crop state assessment map;
3. Extend the capability of the software SPIRITS to assess the crop state using Sentinel-2 data. In absence of long Sentinel-2 time series, the capability of the software will be demonstrated by creating crop masks in the studied region;
4. Produce a crop map at national level using sub-pixel classification of PROBA-V 100 m time series;
5. Assess the possibility for improving WOFOST crop-growth modelled yield by using Sentinel-2 derived biophysical variables.

Project web site: <http://www.rse-sri.com/index.php?l=352>

Partners:




Space Research and Technology Institute – Bulgarian Academy of Sciences (SRTI-BAS) – leading partner



Institute of Soil Science, Agrotechnologies and Plant Protection "Nikola Poushkarov" (ISSAPP "N. Poushkarov")



Vlaamse Instelling voor Technologisch Onderzoek NV (VITO)

*  The Project is funded by the Government of Bulgaria through an ESA Contract (4000117474/16/NL/NDe) under the PECS (Plan for European Cooperating States). The view expressed herein can in no way be taken to reflect the official opinion of the European Space Agency

Coordinating and integrating state-of-the-art Earth Observation Activities in the regions of North Africa, Middle East, and Balkans and Developing Links with GEO related initiatives towards GEOSS¹ - GEO-CRADLE



In a Nutshell

The continuous provision of accurate and timely information through coordinated and sustained Earth Observation (EO) activities is considered a key enabler for informed decision making in response to challenges such as adaptation to climate change, improved food security & water extremes management, better access to raw materials and energy and many more. In this context, large international initiatives such as GEO

(URL: <https://www.earthobservations.org/index.php>) and Copernicus program (URL: <http://copernicus.eu/>) are promoting the integration and coordination of EO capacities at regional, national and international levels.

Despite the important progress made over the past years in the Balkans and in North Africa, in both regions, but even more so in the Middle East, there are still critical gaps in the uptake of EO activities. This includes a disparate level of development with regards to cooperation between the various EO stakeholders, ineffective exploitation of available resources and expertise, limited public awareness on the benefits of EO services and low involvement of the industrial sector of the economy.

GEO-CRADLE has received funding from the European Union's Horizon 2020 Research and Innovation Programme, and will be running from 2016 to 2018 with the aim to tackle these challenges and "*promote the uptake and exploitation of Earth Observation activities in North Africa, Middle East and the Balkans*". To this end, the project has brought together **25 partners from 3 continents**, to work in a highly-complementary team that combines a strong background in EO coordination activities with proven scientific excellence in four key thematic areas – adaptation to climate change, improved food security & water extremes management, access to raw materials, and access to energy.

The project strives to:

- enhance the current knowledge of existing EO capacities in the region (through an ongoing survey),
- facilitate the cooperation between EO stakeholders (through a networking platform and several events),

¹ The GEO-CRADLE project has received funding from the European Union's Horizon 2020 research and innovation programme under grant agreement No 690133.

- identify the gaps and the maturity level (through analysis) and boost the maturity of the different countries in the region,
- enable the exchange of EO data (by setting up a Regional Data Hub),
- showcase concrete ways of tackling regional challenges related to adaptation of climate change, improved food security & water extremes management, better access to raw materials and energy (through feasibility studies),
- propose a roadmap for the implementation of GEO, GEOSS and Copernicus in the three regions.

Project Objectives

GEO-CRADLE brings together key players from three regions (Balkans, North Africa and Middle East) representing the entire Earth Observation (EO) value chain, with the overarching objective of establishing a multi-regional coordination network that:

1. promotes the uptake of EO services and data in response to regional needs;
2. supports the effective integration of existing Earth Observation Capacities in the region;
3. facilitates the engagement of the complete ecosystem of EO stakeholders in the region;
4. enhances the participation in and contribution to the implementation of GEOSS and Copernicus in North Africa, Middle East and the Balkans

The vision of GEO-CRADLE is to pave the way for the sustainable and continuous uptake and exploitation of Earth Observation services in North Africa, Middle East and the Balkans. The different activities undertaken by the GEO-CRADLE have been defined and are pursued in a way that ensures appropriate coordination mechanisms and necessary tools are put in place during the lifetime of the project but are also used beyond that. Therefore, through the establishment of the GEO-CRADLE network and the parallel support of networking activities by a dedicated portal, the project aspires to ensure one of the fundamental requirements for coordinated EO activities; that is an attractive and comprehensive platform, named the Regional Networking Platform, where regional stakeholders can be informed on existing capacities, complementary skills and collaboration opportunities. Another key output of GEO-CRADLE that can contribute to the long-term uptake of EO activities in the region is the operation of the Regional Data Hub. By providing access to region-related datasets and services, directly fed from the GEOSS-portal, and at the same time being the centralized gateway for regional data providers to contribute easily and timely their products to GEOSS, the Regional Data Hub is designed to become the focal node in the region in the context of GEOSS and Copernicus implementation.

Project web-site: <http://geocradle.eu/en/>

EEOBSS: EDUCATION IN EARTH OBSERVATION FOR BULGARIAN SECONDARY SCHOOLS*

The need for education and training of young generation for the utilization of space data and products, in view of their use for the needs of the economy and society, were highlighted at recent meetings of the EU Council on Competitiveness (26/27 May 2016) and during the European week for space solutions (European space solutions) held in the Hague, the Netherlands. Bulgaria, as 18th Space country, continuing its way in space exploration also has ambitions to develop its space economy. To this end April 8, 2015 the Council of Ministers of the Republic of Bulgaria made a historic step in our cooperation with the European Space Agency (ESA), joining the Plan for European Cooperating States (PECS).



As a result of submitted project proposal in the first PECS tender for Bulgaria (AO/1-8268/15/NL/NDe) announced on May 11, 2015, the EEOBSS: Education in Earth observation for Bulgarian secondary schools project was approved for implementation. The project will be implemented for two years (07.2016-07.2018). In the tasks of the project includes a number of educational, communication and media events aimed at reaching a wider audience of students and their teachers. At the mid of 2017 will hold a workshop on the project, at which will be presented and discussed current trends in training in Earth Observation in secondary education both in Europe and nationwide. Within the project will be developed, adapted to Bulgarian educational standards, and issued (online and in print) a modern textbook on Earth observation for Bulgarian secondary schools. The textbook will be available for download upon registration at the project site in the second half of 2017 for the six partner schools participating in the project and for all stakeholders and interested parties. In the Summer of 2017 will be held a summer school aimed at familiarizing students from Bulgarian secondary schools with the theoretical and practical aspects of Earth Observation. All participants will receive Certificates for Attendance. The concluding event of the EEOBSS project (an Exhibition and an Open Day) will celebrate the completion of the project with various activities. On this event will be awarded prizes and certificates to all project partners (students, teachers, school leadership, and media partners). More information on upcoming events can be found on:

- 1) **Project web-site:** <http://eeobss.space>
- 2) **Facebook:** <https://www.facebook.com/eeobss>

3) **Twitter:** <https://twitter.com/eeobss>


Partners:



Space Research and Technology Institute – Bulgarian Academy of Sciences (SRTI-BAS) – leading partner



Information Technologies Institute (ITI), Centre for Research and Technology Hellas (CERTH) – Thessaloniki, Greece (sub-contractor)

*  The Project is funded by the Government of Bulgaria through an ESA Contract (4000117592/16/NL/NDe) under the PECS (Plan for European Cooperating States). The view expressed herein can in no way be taken to reflect the official opinion of the European Space Agency.

**VALENTINA TERESHKOVA
CELEBRATES 80th ANNIVERSARY**



The Soviet cosmonaut Valentina Tereshkova was born on March 6, 1937 in *Bolshoye Maslennikovo*, a village in West Russia. During World War II, when she was only two years old, her father was killed while fighting in the Red Army. Her mother raised Valentina, her sister Lyudmila, and her brother Vladimir, supporting the family by working in a textile plant. Valentina began attending school in 1945, but in 1953 she left school and became a textile-factory assembly worker. She continued her education by correspondence courses and parachuted as a hobby. Later on her parachuting hobby led her being chosen for training as a cosmonaut in the Soviet space program. She continued her education after

her space flight and graduated with distinction from the *Zhukovsky* Military Air Academy in 1969.

During the late 1950s and 1960s, the Space Race between the United States and the Soviet Union escalated for space travel supremacy. The competitiveness between the two nations for "one upping" achievements was fierce and the Soviets were determined to be the first to send a woman into space. After the flight of Yuri Gagarin in 1961, Sergey Korolyov, the chief Soviet rocket engineer, came up with the idea of putting a woman into space. Qualifications included that they should be parachutists less than 30 years of age, less than 170 cm tall, and less than 70 kg in weight. Only five were selected to become cosmonauts out of more than 400 applicants but Tereshkova actually went into space.

Valentina Tereshkova was chosen to be trained as a cosmonaut in the USSR's space program on March 12, 1962. On June 16, 1963, she became the first woman to travel into space aboard *Vostok 6*. Her call sign in this flight was *Chaika*. While the rocket was taking off Tereshkova called out, "Hey sky, take off your hat. I'm on my way!" In just less than three days, she orbited the Earth 48 times. The *Vostok 6* was the final *Vostok* flight. It was launched two days after *Vostok 5*, which carried Valery Bykovsky, into a similar orbit. The *Vostok 5* was in orbit for five days, landing three hours after *Vostok 6*. After she returned from her voyage,

parachuting from her spacecraft to earth from 8000 m, Tereshkova was given the title Hero of the Soviet Union.

On November 3, 1963, Tereshkova married cosmonaut Andrian Nikolayev. On June 8, 1964, was born their daughter, Elena Adrianovna Nikolayeva. Elena was a subject of medical interest because she was the first child born from parents who had both been into space. Elena later on became a medical doctor. Tereshkova and Nikolayev divorced in 1980.

She became a prominent member of the Communist Party, and represented the USSR at numerous international events, including the United Nations conference for the International Women's Year in 1975. She headed the Soviet Committee for Women from 1968 to 1987, was pictured on postage stamps, and had a crater on the Moon named after her.

Despite the success of Tereshkova's flight, there was a 19 year gap before another woman, the Soviet cosmonaut Svetlana Savitskaya, travelled to space in 1982. Many authors suggest that women cosmonauts did not receive the same treatment as their male counterparts. For instance, the first American woman to go into space was Sally Ride in 1983.

Assoc. Prof. Dr. Tanya Ivanova